

Nonlinear Alfvén Wave Model for Solar/Stellar  
Chromosphere, Corona and Wind  
from the Sun to M Dwarfs

Sakaue Takahito (Kyoto University)

December 24, 2020

# Abstract

The stellar atmospheres and winds from the Sun to M dwarfs are highly magnetized. Alfvén waves are responsible for the transfer of magnetic energy in such magnetized plasma. They are involved in heating stellar atmosphere and driving stellar wind through various nonlinear processes. Along this Alfvén wave scenario, we carried out the one-dimensional compressive magnetohydrodynamic (MHD) simulations for the solar atmosphere and wind, and subsequently, M-dwarfs' atmospheres and winds. To investigate the physical mechanisms for heating the stellar atmosphere and driving the stellar wind, the nonlinear propagation of Alfvén wave is calculated from the stellar photosphere, chromosphere to the corona and interplanetary space. In Chapter 2 of this thesis, we present the simulation results of solar atmosphere and wind, and discuss the energy transfer by nonlinear Alfvén waves in the solar chromosphere. It is found that when the nonlinearity of Alfvén waves in the chromosphere exceeds a critical value, the dynamics of the solar chromosphere (e.g., spicule) and the mass-loss rate of solar wind tend to be independent of the energy input from the photosphere. In Chapter 3, we extend our study to the M-dwarfs' atmospheres and winds, and discuss the similarities and differences among the simulated solar and M-dwarfs' atmospheres and winds. In particular, we found that M-dwarfs' coronae tend to be cooler than solar corona, and that M-dwarfs' stellar winds would be characterized with faster velocity and much smaller mass-loss rate compared to those of the solar wind. By developing the semi-empirical method describing the solar and M-dwarf's coronal temperature, stellar wind velocity, and wind's mass-loss rate, the physical mechanisms for these results are discussed.



# Acknowledgments

I would like to express my great appreciation to Kazunari Shibata, Kiyoshi Ichimoto, Ayumi Asai, and all the staff members of the Astronomical Observatory of Kyoto University. I appreciate Nobuyuki Araki and Keiichi Kodaira for inviting me to the field of astronomy and astrophysics. I also appreciate Takayuki Muranushi. I would like to thank Kousuke Namekata, Daikichi Seki, Akiko Tei, Hisashi Hayakawa, Denis P. Cabezas, K. A. P. Singh. I am proud to be a co-author on his/her papers. Finally, I would like to express my deep gratitude to my family.

This study was supported by JSPS KAKENHI Grant Number JP18J12677. A part of this study was carried out by using the computational resources of the Center for Integrated Data Science, Institute for Space-Earth Environmental Research, Nagoya University through the joint research program, XC40 at YITP in Kyoto University, and Cray XC50 at Center for Computational Astrophysics, National Astronomical Observatory of Japan. Numerical analyses were partly carried out on analysis servers at the Center for Computational Astrophysics, National Astronomical Observatory of Japan.



# Contents

<b>1</b>	<b>General Introduction</b>	<b>1</b>
1.1	Overview of Solar/M-dwarf's Atmospheres and Winds	1
1.1.1	Solar Chromosphere, Corona, and Wind	1
1.1.2	M-dwarf's Chromosphere, Corona, and Wind	2
1.2	Alfvén Wave Scenario	13
1.2.1	Alfvén Wave for Heating Atmosphere	13
1.2.2	Alfvén Wave for Driving Stellar Wind	13
<b>2</b>	<b>Energy Transfer by Nonlinear Alfvén Waves in the Solar Chromosphere, and Its Effect on Spicule Dynamics, Coronal Heating, and Solar Wind Acceleration</b>	<b>33</b>
2.1	Introduction	33
2.2	Numerical Setting	34
2.2.1	Basic Equations	34
2.2.2	Magnetic Flux Tube Model	35
2.2.3	Heat Conduction and Radiative Cooling	37
2.2.4	Initial and Boundary Condition	38
2.3	Results	41
2.3.1	Solar Wind Profiles	41
2.3.2	Spicule Dynamics	41
2.4	Analyses	43
2.4.1	Poynting Flux by Alfvén Waves	43
2.4.2	Alfvén Waves in the Chromosphere	46
2.4.3	Slow / Fast Shocks in the Chromosphere	46
2.5	Discussion	50
2.5.1	Intermediate Shock in the Chromosphere	50
2.5.2	Wave Nonlinearity in the Chromosphere	53
2.5.3	Evanescence of Slow Shock in the Chromosphere	56
2.5.4	Comparison with Observation and Other Theoretical Studies	56
2.5.5	Limitations to Our Model and Future Perspectives	59
Appendix 2.A	Mearsurement of Mach number of Fast / Slow Shocks	59
Appendix 2.B	Density Scale Height of the Atmosphere	59
Appendix 2.C	Axisymmetric and Local spherically Symmetric Coordinate Systems	62

<b>3</b>	<b>Nonlinear Alfvén Wave Model of Stellar Coronae and Winds from the Sun to M dwarfs</b>	<b>71</b>
3.1	Introduction . . . . .	71
3.2	Numerical Setting . . . . .	72
3.3	Typical Simulation Results . . . . .	73
3.4	Stellar Coronae and Winds from the Sun to M Dwarfs . . . . .	74
3.5	Semi-empirical method to predict the characteristics of stellar atmosphere and wind . . . . .	74
3.6	Discussion . . . . .	75
Appendix 3.A	Basic Equations . . . . .	79
Appendix 3.B	Semi-empirical Method for Stellar Coronae and Winds . . . . .	80
<b>4</b>	<b>Concluding Remarks</b>	<b>87</b>

# Chapter 1

## General Introduction

### 1.1 Overview of Solar/M-dwarf's Atmospheres and Winds

#### 1.1.1 Solar Chromosphere, Corona, and Wind

The outer atmosphere of the Sun is clearly visible at the total eclipse. In Figure 1.1, the **corona** refers to the pearly-white halo around the Sun, and the **chromosphere** corresponds to the thin, crimson-colored ring seen as the solar limb. Because the overall shape of the corona reflects the magnetic field configuration, it varies with the solar cycle (11 year quasi-periodicity in the sunspot number). The corona at the maximum phase of the solar cycle is close to spherical symmetry and bright features called streamers radially extend (Figure 1.1), while, during the minimum phase, the fine rays called polar plumes are apparent near the poles (Figure 1.2). These observations evidently indicate that the solar atmosphere is highly magnetized. That means the magnetic energy in the solar corona is much abundant compared to the thermal and kinetic energy of the atmosphere so that the large-scale structure of corona is governed by the magnetic field configuration, as seen in Figures 1.1 and 1.2.

The spectroscopic observations further revealed the diverse nature of the physical quantities of coronal and chromospheric plasma (Figure 1.3). The solar corona is filled with the tenuous ( $\lesssim 10^9 \text{ cm}^{-3}$ ), hot ( $\approx 10^6 \text{ K}$ ), fully-ionized plasma (Edlén, 1943; Woolley and Allen, 1948; Miyamoto, 1949), which can be observed especially in the soft X-ray band. In particular, the open and closed magnetic field structures in the solar corona are well distinguished in the soft X-ray image (Figure 1.4(a)). The soft X-ray flux ( $F_{\text{SXR}}$ ) from the closed field region in the vicinity of the sunspot (*active region*) reaches  $6 \times 10^5 \text{ erg cm}^{-2} \text{ s}^{-1}$ , while  $F_{\text{SXR}}$  from the open field region (*coronal hole*) is about  $3 \times 10^3 \text{ erg cm}^{-2} \text{ s}^{-1}$  (Vaiana et al., 1976; Schrijver et al., 1985; Schrijver and Zwaan, 2000). The coronal hole is identified as the origin of the fast solar wind, which is characterized with the flow speed of  $450 - 800 \text{ km s}^{-1}$  and relatively lower density of  $2 - 4 \text{ cm}^{-3}$  at 1 AU (Cranmer et al., 2017). The slow solar wind, on the other hand, shows the flow velocity of  $250 - 450 \text{ km s}^{-1}$  and higher density of  $5 - 20 \text{ cm}^{-3}$  at 1 AU, and the origin of it is thought to be around the active region or coronal hole boundaries.

The chromospheric plasma is, on the other hand, dense ( $\gtrsim 10^{11} \text{ cm}^{-3}$ ), cool ( $\lesssim 10^4 \text{ K}$ ), and partially-ionized (Vernazza et al., 1981; Fontenla et al., 2011). The temperature gradually increases with height in the chromosphere, and drastically rises up to the coronal temperature at the transition region (Figure 1.3). Many strong emission lines in optical range, such as  $\text{H}\alpha$  ( $6563 \text{ \AA}$ ),  $\text{Ca II H \& K}$  ( $3968 \text{ \AA}$  and  $3934 \text{ \AA}$ ),  $\text{Mg II h \& k}$  ( $2803 \text{ \AA}$  and  $2796 \text{ \AA}$ ), are formed in this layer (Figure 1.4(b) and Figure 1.5), and contribute to the strong radiative cooling of the chromosphere which is estimated to be around a few  $\times 10^6 \text{ erg cm}^{-2} \text{ s}^{-1}$  (Bray

and Loughhead, 1974). These chromospheric lines have been analyzed to investigate the dynamics of the chromospheric plasma. In particular, there are numerous observational studies focusing on the small jets called *spicules* (cf., reviews by Beckers, 1972; Sterling, 2000; Tsiropoula et al., 2012). The spicule refers to the frequent eruptions of the chromospheric material toward the corona (Figure 1.6(a)), and ubiquitously distributed around the periphery of the large-scale convection cells, especially in the quiet region and coronal hole (Figure 1.6(b)). The ascending speed of spicules ranges from 15 to 40 km s<sup>-1</sup>, and the maximum height is around 4 – 10 Mm (Pereira et al., 2012; Zhang et al., 2012). It is well known that the spicule in coronal hole tends to be taller and faster than those in the quiet region (Lippincott, 1957; Shibata and Suematsu, 1982; Johannesson and Zirin, 1996).

The above-mentioned properties of the solar corona and chromosphere indicate that both radiative and hydrostatic equilibriums are violated in the solar chromosphere and corona (Jefferies and Morrison, 1973; Athay, 1976; Linsky, 1980). Instead, in order to understand the thermal and kinetic natures of the solar atmosphere, it is fundamentally important to clarify the nonradiative heating mechanisms of the atmosphere and the driving mechanisms of the spicule. One of the major observational constraints on this issue is the inhomogeneity of the radiation from the solar chromosphere and corona. As seen in Figure 1.4, although the coronal hole in soft X-ray image cannot be distinguished from the quiet region in H $\alpha$  (and most chromospheric lines) (Munro and Withbroe, 1972; Wiegelmann and Solanki, 2004), the brightest features in soft X-ray image coincide with those in H $\alpha$ . This suggests that the magnetic field configuration has a great influence on the radiative energy loss from the coronal and chromospheric plasma (Harvey and White, 1999; Pevtsov et al., 2003; Pevtsov et al., 2016), and that the magnetic energy is involved in the nonradiative heating mechanisms of the solar atmosphere. From this point of view, Withbroe and Noyes (1977) presented Table 1.1 as a summary of the chromospheric and coronal energy losses with respect to the different magnetic field configurations (quiet region, coronal hole, and active region). It should be noted that, as seen in Table 1.1, the coronal energy loss is dominated by the conduction flux down to the transition region, rather than by the radiative flux. In other words, the cooling time scale due to the Spitzer-Härm heat conductivity (Spitzer and Härm, 1953) ( $t_{\text{cond}}$ ) is relatively shorter than that due to the optically thin radiative cooling ( $t_{\text{rad}}$ ). The following equations are written in Tajima and Shibata (1997).

$$t_{\text{cond}} = 4 \times 10^2 \text{ s} \left( \frac{L}{10^9 \text{ cm}} \right)^2 \left( \frac{n}{10^9 \text{ cm}^{-3}} \right) \left( \frac{T}{10^6 \text{ K}} \right)^{-5/2}, \quad (1.1)$$

$$t_{\text{rad}} = 4 \times 10^3 \text{ s} \left( \frac{n}{10^9 \text{ cm}^{-3}} \right)^{-1} \left( \frac{T}{10^6 \text{ K}} \right)^2, \quad (1.2)$$

where  $L$  is the typical length scale of the coronal closed loop, and  $n$  and  $T$  is the typical number density and temperature of the coronal plasma. It should be also noted that these cooling time scales are much shorter than the magnetic diffusion time scale due to the Ohmic resistivity ( $t_d$ ), where

$$t_d = 10^{14} \text{ s} \left( \frac{L}{10^9 \text{ cm}} \right)^2 \left( \frac{T}{10^6 \text{ K}} \right)^{3/2}. \quad (1.3)$$

This means the Ohmic dissipation of the coronal magnetic field cannot account for the *coronal (and chromospheric) heating problems* unless the dissipation is extremely localized.

### 1.1.2 M-dwarf's Chromosphere, Corona, and Wind

The presence of stellar chromospheres and coronae is evidently shown by the spectroscopic observations. The chromospheres are characterized with the various optical lines, such as H I Balmer series and Ca II H & K,



Figure 1.1: The total solar eclipse around the maximum phase of solar cycle, observed from Gabon (3 November 2013). The composite was made from original images by Jay M. Pasachoff, Allen B. Davis, and Vojtech Rusin with computer analysis by Miloslav Druckmüller, according to Pasachoff (2017). ©2013 Constantinos Emmanoulidis, ©2014 Miloslav Druckmüller. Available from [http://www.zam.fme.vutbr.cz/~druck/eclipse/Ecl2013g/TSE\\_2013\\_ed/0-info.htm](http://www.zam.fme.vutbr.cz/~druck/eclipse/Ecl2013g/TSE_2013_ed/0-info.htm).



Figure 1.2: The total solar eclipse around the minimum phase of solar cycle, observed from Chile (2 July 2019). ©2019 Miloslav Druckmüller, Peter Aniol. Available from [http://www.zam.fme.vutbr.cz/~druck/eclipse/Ecl2019ch/Tres\\_Cruses/TC\\_347mm/00-info.htm](http://www.zam.fme.vutbr.cz/~druck/eclipse/Ecl2019ch/Tres_Cruses/TC_347mm/00-info.htm).

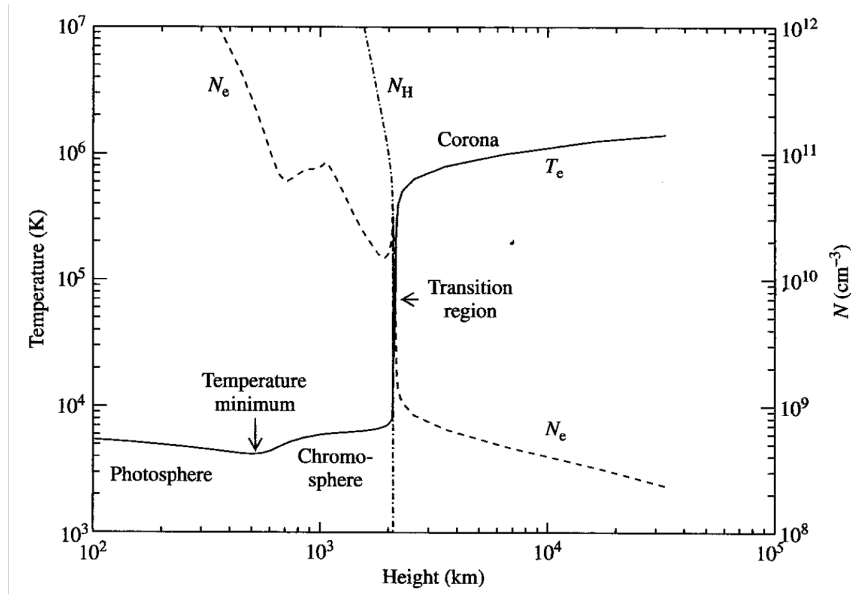


Figure 1.3: The vertical profiles of electron temperature ( $T_e$ ), number densities of electrons ( $N_e$ ) and neutral hydrogen atoms ( $N_H$ ) in the solar atmosphere. Adapted from Phillips et al. (2008) who referred to Vernazza et al. (1981), Fontenla et al. (1988) and Gabriel (1976).

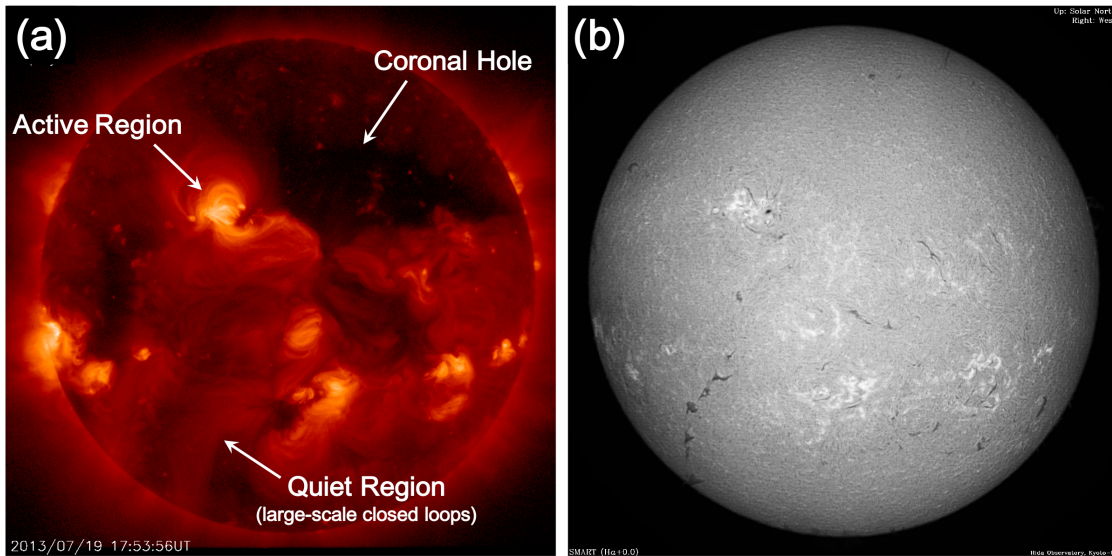


Figure 1.4: (a) The solar corona in the soft X-ray band observed by the X-Ray Telescope (XRT) (Ti-poly filter) on Hinode, on 19 July 2013. The examples of active region, quiet region and coronal hole are indicated by the white arrows. (b) The solar chromosphere in H $\alpha$  line (6563Å) observed by the Solar Magnetic Activity Research Telescope (SMART) of Hida Observatory (Kyoto University) on the same day.

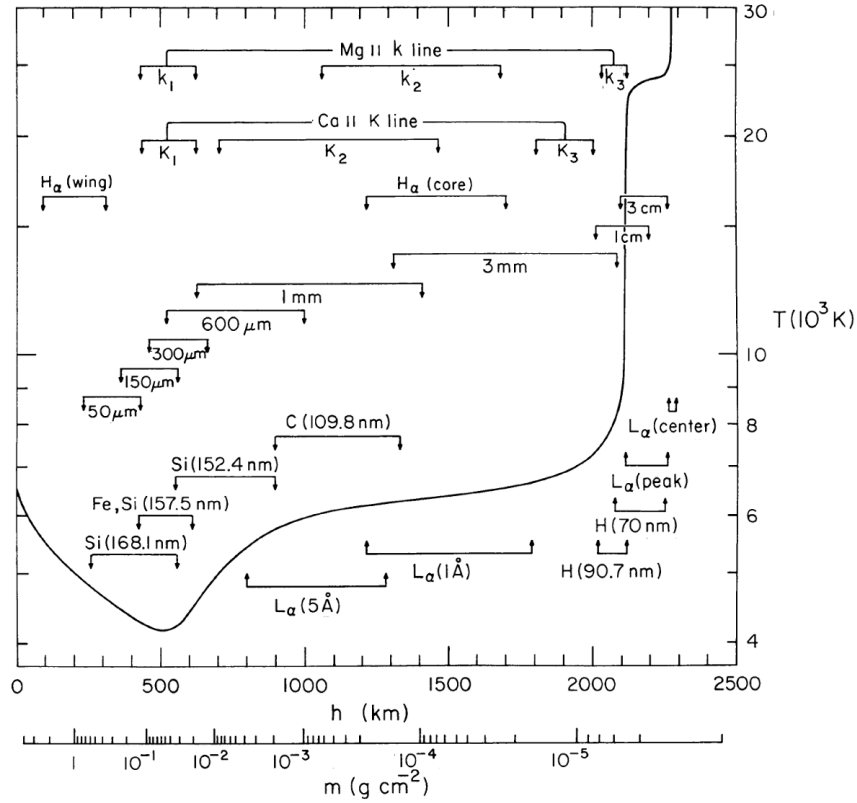


Figure 1.5: The approximate formation heights of the solar chromospheric lines and continua, with the vertical profile of temperature. Reproduced from Vernazza et al. (1981).

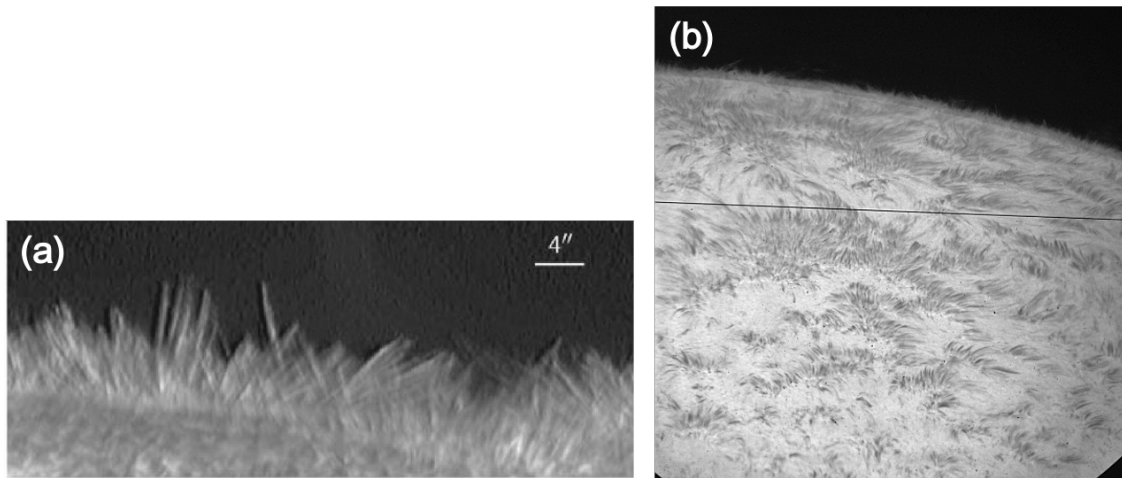


Figure 1.6: (a) Spicules as seen through the BFI Ca II H filter on board Hinode/SOT. The image was taken on 2006 November 21 near an active region on the east limb. Note that 4'' in this panel is equal to  $2.9 \times 10^3$  km. ©The Author(s) 2019. Published by Oxford University Press on behalf of the Astronomical Society of Japan. This is an Open Access article distributed under the terms of the Creative Commons Attribution License (<http://creativecommons.org/licenses/by/4.0/>), which permits unrestricted reuse, distribution, and reproduction in any medium, provided the original work is properly cited. (b) The distribution of spicules on the solar disk in the slitjaw image of  $H\alpha -0.65 \text{ \AA}$  taken by the Domeless Solar Telescope of Hida Observatory (Kyoto University) on 2018 July 20.

Table 1.1: Chromospheric and coronal energy losses (Adapted from [Withbroe and Noyes, 1977](#))

Parameter	Quiet region	Coronal hole	Active region
Transition layer pressure (dyn cm <sup>-2</sup> )	$2 \times 10^{-1}$	$7 \times 10^{-2}$	2
Coronal temperature (K, at $r \approx 1.1R_{\odot}$ )	$1.1 - 1.6 \times 10^6$	$10^6$	$2.5 \times 10^6$
Coronal energy losses (erg cm <sup>-2</sup> s <sup>-1</sup> )			
Conduction flux $F_c$	$2 \times 10^5$	$6 \times 10^4$	$10^5$ to $10^7$
Radiative flux $F_r$	$10^5$	$10^4$	$5 \times 10^6$
Solar wind flux $F_w$	$\lesssim 5 \times 10^4$	$7 \times 10^5$	( $< 10^5$ )
Total coronal loss $F_c + F_r + F_w$	$3 \times 10^5$	$8 \times 10^5$	$10^7$
Chromospheric radiative losses (erg cm <sup>-2</sup> s <sup>-1</sup> )			
Low chromosphere	$2 \times 10^6$	$2 \times 10^6$	$\lesssim 10^7$
Middle chromosphere	$2 \times 10^6$	$2 \times 10^6$	$10^7$
Upper chromosphere	$3 \times 10^5$	$3 \times 10^5$	$2 \times 10^6$
Total chromospheric loss	$4 \times 10^6$	$4 \times 10^6$	$2 \times 10^7$
Solar wind mass loss (g cm <sup>-2</sup> s <sup>-1</sup> )	$\lesssim 2 \times 10^{-11}$	$2 \times 10^{-10}$	( $< 4 \times 10^{-11}$ )

and the continua at the ultraviolet, infrared and radio wavelengths, while the coronae are observable in the (extreme-)ultraviolet and X-ray radiations. These emissions indicate that the atmospheric structure departs from the radiative equilibrium, and that some nonradiative heating mechanisms are required to meet the energy balance in the stellar atmosphere against the strong radiative cooling.

In order to infer the physical mechanisms leading to the formation of stellar chromospheres and coronae, the distribution of stars with these hot atmospheres in the Hertzsprung-Russell diagram (HR diagram) has been discussed. [Linsky \(1980\)](#) noted that Ca II H & K emission is occasionally seen in F stars, is usually seen in G stars, and is essentially ubiquitous in K and M stars, on the basis of the bibliography compiled by [Bidelman \(1954\)](#), while [Ulmschneider \(1979\)](#) concluded that all non degenerate type stars have chromospheres except possibly the A stars, according to his definition of stellar chromospheres. The chromospheric ultraviolet emission can be detected for spectral types F and later ([Böhm-Vitense and Dettmann, 1980](#); [Wolff et al., 1986](#)). As for the stellar coronae, the X-ray observations revealed that the coronal emission is common phenomena among nearly every type of star, except for the cooler giants and subgiants ([Linsky and Haisch, 1979](#); [Vaiana et al., 1981](#); [Helfand and Caillault, 1982](#); [Hünsch and Schroeder, 1996](#); [Hünsch et al., 1998](#)).

These statistical studies suggest that the chromospheres and coronae of main-sequence stars with spectral types later than F are causally related to their convective envelope and the dynamo processes in this layer ([Wilson, 1966a](#); [Wilson, 1966b](#); [Ayres et al., 1981](#); [Pallavicini et al., 1981](#)). Because the differential rotation in the convective envelope is the essential process for the generation of large-scale magnetic field by solar-like dynamo ([Parker, 1955](#); [Dikpati and Charbonneau, 1999](#)), the relation between large-scale magnetic field and enhancement of chromospheric or coronal radiations, which is confirmed by the solar observations (see Section 1.1.1), is generally expected to be applicable to the main-sequence stars with spectral types later than F. These stars also show the time-dependent chromospheric and coronal activities in wide time scale range, similarly to the Sun, e.g., stellar flares ([Kodaira et al., 1976](#); [Audard et al., 2000](#); [Maehara et al., 2012](#); [Shibayama et al., 2013](#)), surface inhomogeneity inferred from the rotational modulation ([Vaughan et al., 1981](#); [Baliunas et al., 1983](#); [Namekata et al., 2019](#)), and long-term activity cycle ([Wilson, 1978](#); [Duncan et al., 1991](#); [Baliunas et al., 1995](#)).

As implied above, the stellar chromospheric and coronal radiations are correlated with the stellar rotation through the dynamo action to generate the stellar magnetic field. [Schatzman \(1962\)](#) and [Weber and Davis \(1967\)](#) further pointed out that the stellar rotation could be decelerated as a result of angular momentum loss by the magnetized stellar wind (i.e. magnetic braking). These scenarios have been extensively examined by numerous observational studies, in terms of the *stellar activity-rotation relations*. [Kraft \(1967\)](#) investigated the Ca II emissions of F2 IV, V and G3 IV, V stars, and showed that the average rotational velocity of stars with active chromospheres is higher than that with inactive chromospheres. [Noyes et al. \(1984\)](#) confirmed the negative correlation between the rotation periods and the Ca II emissions among F, G, K stars. Similarly, there are many studies investigating the relationships between the rotation and various activity indicators, including the ultraviolet lines ([Simon et al., 1985](#); [Rutten, 1987](#); [Rutten and Schrijver, 1987](#); [Youngblood et al., 2017](#)), extreme ultraviolet ([Mathioudakis et al., 1995](#); [Kellett and Tsikoudi, 1997](#)), X-ray ([Pallavicini et al., 1981](#); [Maggio et al., 1987](#); [Pizzolato et al., 2003](#); [Wright et al., 2011](#)), and radio emissions ([Stewart et al., 1988](#); [Slee and Stewart, 1989](#)). Note that such a diversity of activity indicators is naturally expected because of the tight correlations among the chromospheric and coronal emissions ([Schrijver, 1987](#); [Martínez-Arnáiz et al., 2011](#)). [Skumanich \(1972\)](#) showed the power-law decay of both Ca II emission and rotational velocity with time, by comparing Pleiades, Ura Major, Hyades stars and the Sun. This activity-age relation for solar-type stars was further developed by [Ayres \(1997\)](#), [Ribas et al. \(2005\)](#), [Mamajek and Hillenbrand \(2008\)](#) (Figure 1.7). Finally, it should be noted that, as an indicator of the stellar rotation, Rossby number (Ro) is sometimes used in these studies. Rossby number is a nondimensional parameter defined as  $P_{\text{rot}}/\tau_c$ , where  $P_{\text{rot}}$  and  $\tau_c$  are the rotation period and convective turnover time ([Gilman, 1980](#); [Kim and Demarque, 1996](#)), respectively. [Wright et al. \(2011\)](#) presented an empirical formula:  $\log(\tau_c/\text{day}) = 1.16 - 1.49 \log(M/M_\odot) - 0.54[\log(M/M_\odot)]^2$  ( $0.09 < M/M_\odot < 1.36$ ), which is a monotonic increase function of stellar mass ( $M$ ). [Noyes et al. \(1984\)](#) proposed that the Ca II emissions could be better correlated with the Rossby number rather than the rotation period. On the other hand, the definition of convective turnover time and the applicability of Rossby number in activity-rotation relation are still under debate ([Stepien, 1994](#); [Reiners et al., 2014](#); [Suárez Mascareño et al., 2016](#)). Figures 1.8 and 1.9 show the activity-rotation relations in X-ray ([Wright et al., 2011](#)) and in Ca II emissions ([Suárez Mascareño et al., 2016](#)). The right panel of Figure 1.8 shows that, for the stars with the rotation period longer than  $\sim 0.1\tau_c$ , the X-ray to bolometric luminosity ratio ( $R_X$ ) declines with increasing Rossby number (Ro) while for the rapidly rotating stars ( $P_{\text{rot}} \lesssim 0.1\tau_c$ ),  $R_x$  appears to saturate.

Among the above-mentioned stars with chromospheres and coroneae, we particularly focus on the M-type main-sequence stars (M dwarfs) in this thesis.

M dwarfs are the tiniest and coolest stars on the main sequence in HR diagram. The schematic relation between their masses and radii is plotted in Figure 1.10. The fundamental parameters are listed in Table 1.2. The cooler  $T_{\text{eff}}$  and larger  $\log_{10} g$  in Table 1.2 immediately indicate the strongly stratified M-dwarf's atmosphere. It is expected that the magnetic flux concentration on such a high-pressure photosphere of M dwarf is characterized with much stronger field strength compared to the Sun ([Saar, 1990](#); [Reiners, 2012](#))<sup>1</sup>. Actually, the magnetic field observed on the M dwarfs' surfaces are quite strong especially in the case of rapidly rotating stars ([Reiners and Basri, 2007](#); [Reiners et al., 2009](#)). Figure 1.11 shows the activity-rotation relation in the observed magnetic field strength ([Shulyak et al., 2017, 2019](#)). [Kochukhov \(2021\)](#) noted that the 24 rapidly rotating M dwarfs with  $\text{Ro} \leq 10^{-2}$  have the magnetic field strength ranging from 2.0 to 7.3 kG ( $4.3 \pm 1.5$  kG on average), and that this group represents the most magnetized late-type stars currently

<sup>1</sup>It should be noted that, however, [Rajaguru et al. \(2002\)](#) and [Beeck et al. \(2015\)](#) suggested that convective collapse ([Parker, 1978](#)) on these cool dwarfs is inefficient to generate as strong field strengths as the equipartition field because of the lack of superadiabaticity in the upper convection zone layers.

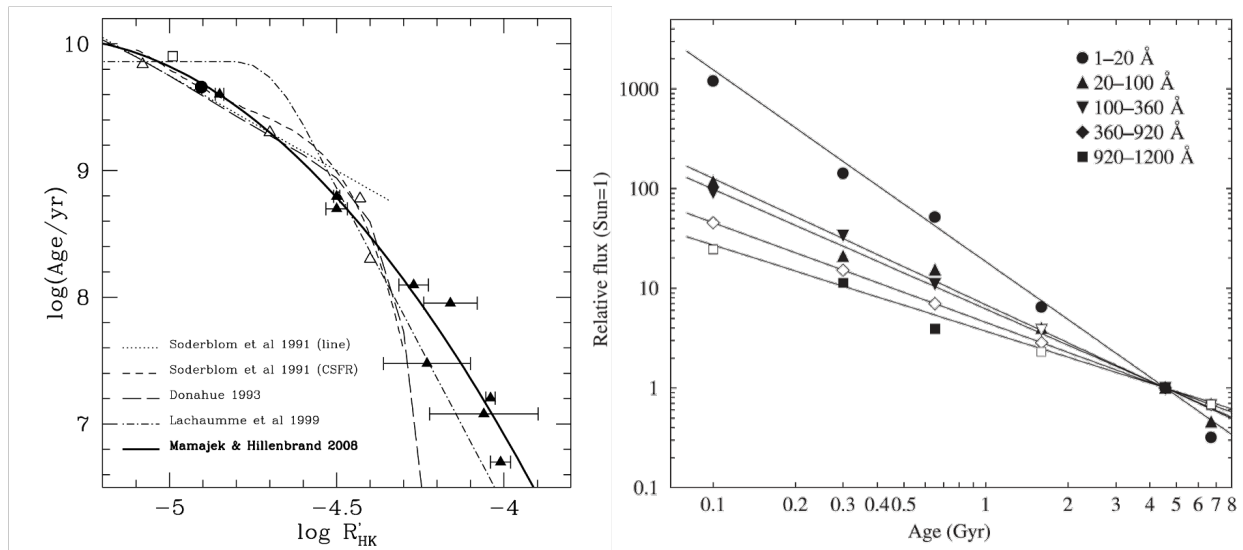


Figure 1.7: *left panel*: Mean  $\log R'_{\text{HK}}$  cluster values (interpolated to solar  $B - V$ ) vs cluster age, where  $R'_{\text{HK}}$  is defined as the ratio of the emission from the chromosphere in the cores of the Ca II H & K lines to the total bolometric emission of the star (Noyes et al., 1984). Adapted from Mamajek and Hillenbrand (2008). The filled triangles are cluster mean  $\log R'_{\text{HK}}$  values, including those of USco (5 Myr),  $\beta$  Pic (12 Myr), UCL+LCL (16 Myr), Tuc-Hor (30 Myr),  $\alpha$  Per (85 Myr), Pleiades (130 Myr), UMa (500 Myr), Hyades (625 Myr), and M67 (4 Gyr). The open triangles are ancillary cluster mean  $\log R'_{\text{HK}}$  values, including those of M34 (200 Myr), Coma Ber (600 Myr), NGC 752 (2 Gyr), M67 (4 Gyr), NGC 188 (6.9 Gyr). The open square is the mean datum for the 5–15 Gyr old solar-type dwarfs from Valenti and Fischer (2005). The filled circle is the Sun. Previously published activity-age relations are plotted as dotted and/or dashed lines. The thick fitted line represents  $\log \tau = -38.053 - 17.912 \log R'_{\text{HK}} - 1.6675(\log R'_{\text{HK}})^2$ , or  $\log R'_{\text{HK}} = 8.94 - 4.849 \log \tau + 0.624(\log \tau)^2 - 0.028(\log \tau)^3$ . In particular,  $R'_{\text{HK}} \propto \tau^{-0.63}$  around  $\tau = 4.56$  Gyr. *right panel*: Stellar age vs extreme ultraviolet fluxes for different stages of the evolution of solar-type stars: EK Dra (0.10 Gyr),  $\pi^1$  UMa+ $\chi^1$  Ori (0.30 Gyr),  $\kappa^1$  Cet (0.65 Gyr),  $\beta$  Com (1.6 Gyr), Sun (4.56 Gyr), and  $\beta$  Hyi (6.7 Gyr). Adapted from Ribas et al. (2005). The filled symbols are the observed fluxes of different wavelength bands. The open symbols are the estimated fluxes based on the assumptions of power-law decay.

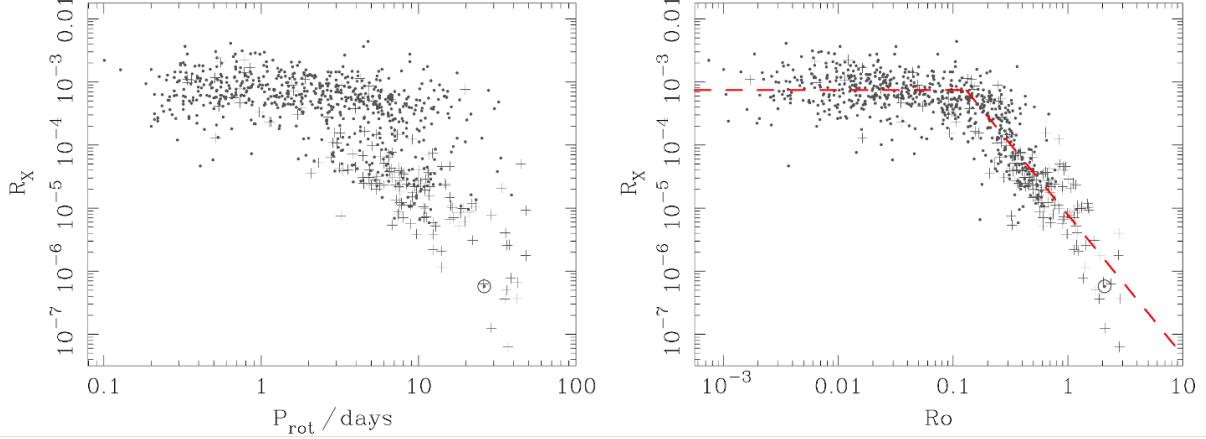


Figure 1.8: *left panel*: X-ray to bolometric luminosity ratio ( $R_X$ ) vs rotation period ( $P_{\text{rot}}$ ). *right panel*:  $R_X$  vs Rossby number ( $Ro$ ). The sample plotted here consists of 824 solar and late-type stars ( $0.1 \lesssim M/M_{\odot} \lesssim 5$ ). The plus symbols represent the stars known to be binaries. The dashed red line in the right panel represent  $R_X \propto Ro^{-2.18 \pm 0.16}$  for  $Ro \geq Ro_{\text{sat}} = 0.13 \pm 0.02$  and  $R_X = 10^{-3.13 \pm 0.08}$  for  $Ro \leq Ro_{\text{sat}}$ . Adapted from Wright et al. (2011).

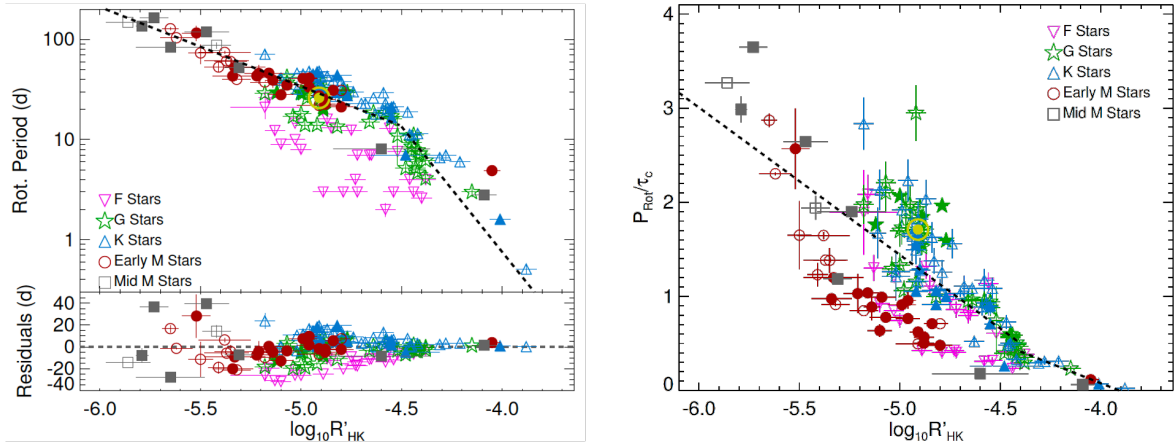


Figure 1.9: *left panel*: Chromospheric activity level  $\log R'_{\text{HK}}$  vs rotation period. *right panel*:  $\log R'_{\text{HK}}$  vs Rossby number. Adapted from Suárez Mascareño et al. (2016). Filled symbols show the stars analyzed in Suárez Mascareño et al. (2016), while others represent those in the other literatures (see Suárez Mascareño et al., 2016). The dashed line shows the best fit to the data, leaving out the F-type stars.

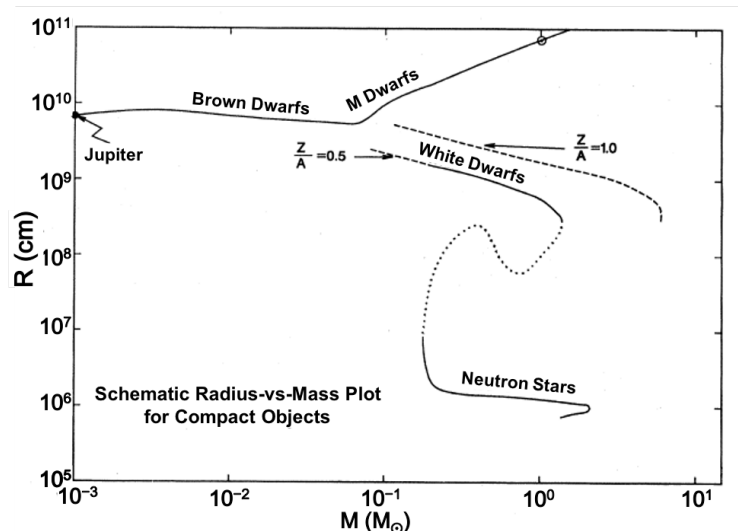


Figure 1.10: Radius versus mass for cold brown dwarfs, M dwarfs, white dwarfs, and neutron stars, demonstrates that the radii of low-mass brown dwarfs plateau over a broad range of masses. The cold brown dwarfs are at the hydrogen-rich (high  $Z/A$ ) low-mass end of the white dwarf family. The positions of the Sun and Jupiter are clearly marked. Reproduced from [Burrows and Liebert \(1993\)](#).

known. The large-scale structures of M dwarfs' magnetic field have been also investigated ([Donati et al., 2008](#); [Morin et al., 2008](#); [Morin et al., 2010](#)). These studies are believed to contribute to the understanding the difference in the dynamo processes between the partly- and fully-convective dwarfs.

The study on M-dwarf's magnetic activities is motivated by the following scientific interests.

The first interest is in whether physical mechanisms for the M-dwarf's and solar magnetic activities can be understood in a unified way.

The magnetic activities of M dwarfs and the earlier dwarfs have been compared especially by investigating their activity-rotation relations. In particular, the X-ray observations suggest that the coronal emissions from M dwarfs could be related to their rotation by the same activity-rotation relation as that observed in F, G, K dwarfs ([Pizzolato et al., 2003](#); [Wright et al., 2011](#); [Wright and Drake, 2016](#); [Wright et al., 2018](#)). [Wright et al. \(2018\)](#) suggested the two possibilities. (i) The activity-rotation relation does not change depending on any types of dynamo, or (ii) both fully-convective and partly-convective stars operate very similar dynamos that rely on the interaction of rotation and turbulent convection. The M-dwarf's activity-rotation relations have been also investigated for the chromospheric lines, including  $H\alpha$  ([Delfosse et al., 1998](#); [Mohanty and Basri, 2003](#); [Reiners et al., 2012](#); [West et al., 2015](#); [Newton et al., 2017](#)) and Ca II H & K ([Browning et al., 2010](#); [Suárez Mascareño et al., 2016](#); [Astudillo-Defru et al., 2017](#)). However, it is not true that any activity indicators of M dwarfs can be related to the rotation in the same manner as the earlier dwarfs. [Astudillo-Defru et al. \(2017\)](#) and [Suárez Mascareño et al. \(2018\)](#) concluded that the activity-rotation relation in Ca II H & K ( $\log R'_{\text{HK}}$ ) of M0-M6 dwarfs clearly shows the saturation regime for rapidly rotating stars ( $P_{\text{rot}} < 10\text{d}$ ) similarly to the activity-rotation relation in X-ray. On the other hand, this result implies that the activity-rotation relation in  $\log R'_{\text{HK}}$  of M0-M6 dwarfs does not match that of the earlier dwarfs. Actually, [Mamajek and Hillenbrand \(2008\)](#) showed that  $\log R'_{\text{HK}}$  of F7-K2 dwarfs is very strongly anticorrelated with Rossby number rather than saturated, and argued that the correlation between Ca II emissions and X-ray is much

Table 1.2: Fundamental properties of M dwarfs. (Adapted from Reid and Hawley, 2005)

Spectral Type	$T_{\text{eff}}$ [K]	$R/R_{\odot}$	$M/M_{\odot}$	$L/(10^{-2}L_{\odot})$	$\log_{10} g$	Prototype
M0	3,800	0.62	0.60	7.2	4.65	Gl 278C
M1	3,600	0.49	0.49	3.5	4.75	Gl 229A
M2	3,400	0.44	0.44	2.3	4.8	Gl 411
M3	3,250	0.39	0.36	1.5	4.8	Gl 725A
M4	3,100	0.36	0.20	0.55	4.9	Gl 699
M5	2,800	0.20	0.14	0.22	5.0	Gl 866AB
M6	2,600	0.15	0.10	0.09	5.1	Gl 406
M7	2,500	0.12	$\sim 0.09$	0.05	5.2	Gl 644C (VB 8)
M8	2,400	0.11	$\sim 0.08$	0.03	5.2	Gl 752B (VB 10)
M9	2,300	0.08	$\sim 0.075$	0.015	5.4	LHS 2924

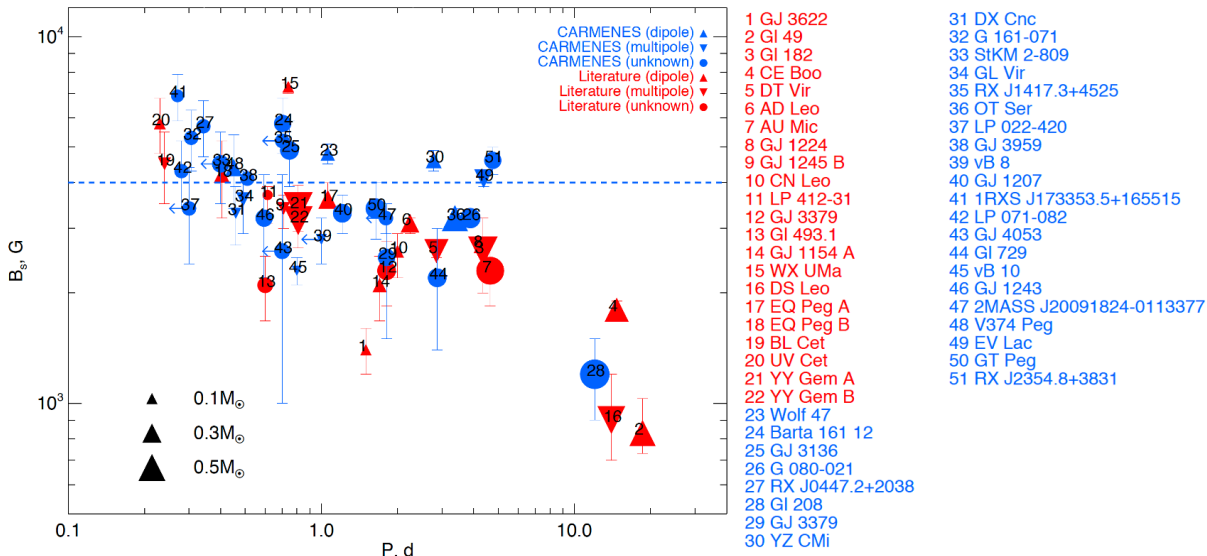


Figure 1.11: Average magnetic fields as a function of rotation period. Adapted from Shulyak et al. (2019). Measurements in stars with known dipole and multipole states are shown as solid upward- and downward-pointing triangles, respectively. Stars with unknown dynamo states are shown as solid blue circles. The measurements by Shulyak et al. (2019) are shown with blue color and the literature values are shown with the red one. The symbol size scales with stellar mass. The horizontal dashed line marks the 4 kG threshold of saturated magnetic field originally suggested by Reiners et al. (2009).

poor for the rapidly rotating stars. [Suárez Mascareño et al. \(2016\)](#) also pointed out that F and M stars do not follow the same exact relation as that of solar-type stars (see right panel of [Figure 1.9](#)).

The diverse nature of activity-rotation relations among M dwarfs and the earlier dwarfs is also expected from the deviations of flux-flux relations. [Oranje \(1986\)](#), [Schrijver and Rutten \(1987\)](#) and [Rutten et al. \(1989\)](#) reported that the flux-flux relations among the chromospheric and coronal emissions differ between M dwarfs and the earlier dwarfs. [Linsky et al. \(2020\)](#) pointed out that, at the same X-ray flux level (normalized to a distance of 1 AU), the more active M3–M7.5 stars show Ly $\alpha$  emission a factor of 4 smaller than corresponding F–K stars, and for the least active late-M stars, the Ly $\alpha$  emission is a factor of 10 lower.

The activity-rotation relation and flux-flux relation are more complicated in the dwarf stars later than M6. [McLean et al. \(2012\)](#) examined the activity-rotation relations in radio, X-ray and H $\alpha$  at spectral type later than M7, and reported none of them agree with those of the earlier dwarfs, respectively ([Figure 1.12](#)). In these ultracool dwarfs, it is well known that the activity observed in H $\alpha$  and X-ray rapidly decline ([Gizis et al., 2000](#); [Mohanty and Basri, 2003](#); [Fleming et al., 2003](#); [Williams et al., 2014](#); [Berger et al., 2010](#); [Cook et al., 2014](#)). [Figure 1.12](#) clearly shows that, unlike X-ray and H $\alpha$ , the radio luminosity remains unchanged as a function of rotation velocity and spectral type.

In order to understand the above observational results, the semi-empirical model atmosphere have been developed to reproduce the observed spectra of chromospheric lines or continua ([Cram and Mullan, 1979, 1985](#); [Houdebine and Doyle, 1994](#); [Mauas and Falchi, 1994](#); [Houdebine and Stempels, 1997](#); [Fontenla et al., 2016](#); [Peacock et al., 2019a, 2019b, 2020](#)). However, because of the lack of knowledge about the physical mechanisms for coronal and chromospheric heating, the origins of the diverse nature in the activity-rotation relation and flux-flux relation remain unsolved.

The second interest is in the influence of M-dwarf’s magnetic activities on the interplanetary space and exoplanets.

M dwarf’s magnetic activities have been particularly discussed with the focus on their impact on the planetary atmosphere. The planets orbiting M dwarfs are favorable targets for the extrasolar habitable worlds ([Kasting et al., 1993](#); [Kaltenegger and Traub, 2009](#); [Seager, 2013](#); [Kopparapu et al., 2017](#)). [Driscoll and Barnes \(2015\)](#) summarized the following reasons: (1) the habitable zone around M dwarfs is much closer to the star, making an Earth-mass planet in the habitable zone an easier target, (2) low-mass M dwarfs are more abundant in the nearby solar neighborhood, and (3) M dwarfs have longer main sequence times. On the other hand, the strong magnetic activity of M dwarfs, such as stellar flares, could strongly affect the planets in the habitable zone around M dwarfs ([Scalo et al., 2007](#); [Tarter et al., 2007](#); [Segura et al., 2010](#)). Their upper atmospheres are exposed to the high energy radiation in ultraviolet to X-ray range from the stellar atmosphere ([Tian, 2009](#); [Lammer et al., 2012](#); [Tian and Ida, 2015](#); [Owen and Mohanty, 2016](#)) and affected by the stellar wind ([Vidotto et al., 2011](#); [Vidotto et al., 2014](#); [Cohen et al., 2014](#); [Cohen et al., 2015](#); [Garraffo et al., 2016](#); [Garraffo et al., 2017](#); [Dong et al., 2017](#); [Dong et al., 2018](#)). The resultant mass loss from the planet’s atmosphere would determine its evolution especially for lower-mass planets.

In particular, there are a few observational reports of M-dwarf’s stellar winds, which could directly and continuously interact with the planetary atmosphere or magnetosphere. [Wood et al. \(2001, 2002, 2005a,b\)](#) estimated  $\dot{M}$  of several nearby stars, by detecting the absorption signatures in stellar Ly $\alpha$  spectra which originates in the “neutral hydrogen wall” around the astrospheres. Although their analysis included four M dwarfs (Proxima Centauri, AD Leo, EV Lac, AU Mic), the signature of astrosphere is detected only on EV Lac, leading to the estimation of  $\dot{M} \sim 2 \times 10^{-14} M_{\odot} \text{ yr}^{-1}$ . Note that they also suggested an upper limit of Proxima Centauri’s  $\dot{M} \sim 4 \times 10^{-15} M_{\odot} \text{ yr}^{-1}$ . [Bourrier et al. \(2016\)](#) and [Vidotto and Bourrier \(2017\)](#) deduced  $\dot{M}$  of GJ 436 (M2.5) around  $(0.45 - 2.5) \times 10^{-15} M_{\odot} \text{ yr}^{-1}$ , by analyzing the transmission spectra

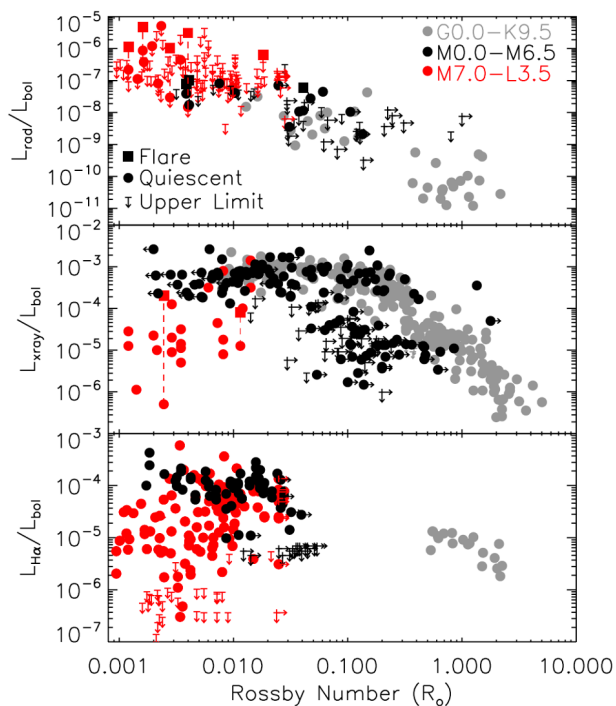


Figure 1.12: Activity-rotation relations in radio, X-ray, and  $H\alpha$ , as a function of Rossby number. Adapted from [McLean et al. \(2012\)](#). Right arrows indicate lower limits in  $Ro$ . Red symbols represent objects later than M7, black symbols represent objects with spectral types M0–M6.5, and gray symbols represent spectral types G–K.

of Ly $\alpha$  of GJ 436 b (a warm Neptune). On the other hand, the estimation of stellar wind's mass-loss rate by Wood et al. relies on the assumption that the velocities of any stellar winds are around 400 km s<sup>-1</sup> regardless of the stars.

## 1.2 Alfvén Wave Scenario

### 1.2.1 Alfvén Wave for Heating Atmosphere

For the coronal and chromospheric heating problems, Biermann (1946) and Schwarzschild (1948) proposed the acoustic wave heating mechanism, in which the upward-propagating acoustic wave is generated by the turbulent convection on the stellar surface, and transport the wave energy until it is dissipated through the steepening to shock in the stratified stellar atmosphere. Osterbrock (1961) generalized this idea by considering the magnetohydrodynamic shocks. He also pointed out the possibility that the slow shocks in the chromosphere could carry the chromospheric matter up into the corona when they reach the top of chromosphere, as the plausible idea of the spicule formation.

Based on these pioneering works, the acoustic wave propagation in the solar and stellar chromosphere has been widely investigated by the hydrodynamic simulations, in order to discuss the spicule formation (Steinolfson et al., 1979; Suematsu et al., 1982; Shibata et al., 1982; Shibata and Suematsu, 1982) and the stellar chromospheric heating (Mullan and Cheng, 1993, 1994; Cuntz et al., 1998, 1999; Buchholz et al., 1998; Ulmschneider et al., 2001a, 2001b; Fawzy and Stępień, 2018).

The above chromospheric heating models, however, can be applied only to the nonmagnetic chromospheric regions of the most magnetically inactive stars (Narain and Ulmschneider, 1990, 1996). That means the activity-rotation relation is not attributed to the acoustic heating mechanism (Schrijver, 1995). The difficulties of acoustic wave heating model strongly suggest that it is essential to consider the energy transfer by Alfvén wave, for the discussion about the magnetically active stellar chromosphere and corona. Alfvén wave can play a significant role in carrying the magnetic energy in the magnetized plasma owing to its incompressible nature. On the other hand, various physical mechanisms are suggested as the wave energy dissipation processes of Alfvén wave. In the non-uniform background media like the stratified atmosphere, small-scale structures that is favorable to the Ohmic or viscous dissipation are naturally induced by the propagation of (linear) Alfvén wave through the phase-mixing (Heyvaerts and Priest, 1983; Shoda and Yokoyama, 2018), turbulent cascade (Kraichnan, 1965; Hollweg, ; Velli et al., 1989; Sridhar and Goldreich, 1994; Goldreich and Sridhar, 1995), or resonant absorption (Ionson, 1978; Ofman et al., 1994; Ofman and Davila, 1995; Antolin et al., 2016). The propagating Alfvén wave energy is also reduced by the nonlinear mode coupling with the compressible waves through the direct steepening (Hollweg, 1982; Suzuki, 2004) or parametric decay instability (Goldstein, 1978; Derby, 1978; Terasawa et al., 1986; Shoda and Yokoyama, 2016). Despite of these various dissipation processes, it is widely believed that Alfvén wave can be responsible for supplying the magnetic energy steadily from the stellar surface to the chromosphere and corona, and depositing its wave energy to the background plasma so that the thermal structure of the stellar atmosphere is maintained.

Based on this Alfvén wave scenario, therefore, numerous studies have addressed the coronal and chromospheric heating problems especially by performing the magnetohydrodynamical (MHD) numerical simulations (Hollweg et al., 1982; Moriyasu et al., 2004; Matsumoto and Shibata, 2010; Antolin and Shibata, 2010; Washinoue and Suzuki, 2019; Wang and Yokoyama, 2020; Matsumoto, 2016; Matsumoto, 2018).

### 1.2.2 Alfvén Wave for Driving Stellar Wind

Since [Parker \(1958\)](#) pointed out that it is not possible for the atmosphere of any star to be in complete hydrostatic equilibrium out to large distances, the high-temperature solar and stellar coronae are believed to be always associated with *solar and stellar winds*. To describe the hydrodynamic expansion of solar corona, the following equations for mass and momentum conservations in the spherically symmetric coordinate system are helpful:

$$\frac{d}{dr}(\rho ur^2) = 0, \quad u \frac{du}{dr} = -\frac{1}{\rho} \frac{dp}{dr} - \frac{GM_\odot}{r^2}. \quad (1.4)$$

By defining the sound speed  $c_s = \sqrt{p/\rho}$  as a function of  $r$ , the equation of motion is expressed as below:

$$\frac{du^2}{dr} \left(1 - \frac{c_s^2}{u^2}\right) = -2r^2 \frac{d}{dr} \left(\frac{c_s^2}{r^2}\right) - \frac{2GM_\odot}{r^2}. \quad (1.5)$$

Assuming that  $c_s = \text{uniform}$ ,<sup>2</sup> [Parker \(1958\)](#) showed that, for a given temperature, there is a unique inner boundary condition about  $u = u_0 (< c_s)$  which eventually connects to the supersonic outflow in the distance, i.e., the solar wind. To obtain such a transonic flow solution from Equation (1.5), however, it is inevitable to specify the temperature distribution (or the profile of atmospheric heating rate) in the stellar corona and wind. The coronal heating problem and stellar wind acceleration problem are tightly related to each other in this sense.

[Lamers and Cassinelli \(1999\)](#) discussed more general expressions in the hydrodynamic regime, considering the heat and momentum deposition in the stellar wind.

$$\frac{d}{dr}(\rho ur^2) = 0, \quad u \frac{du}{dr} + \frac{1}{\rho} \frac{dp}{dr} + \frac{GM_\star}{r^2} = f, \quad (1.6)$$

where  $f$  is the outward directed force per unit mass.

$$\frac{de}{dr} = f + q, \quad \text{where } e = \frac{u^2}{2} + \frac{a_s^2}{\gamma - 1} - \frac{GM_\star}{r} = e_0 + \int_{r_0}^r f dr + \int_{r_0}^r q dr, \quad (1.7)$$

where  $a_s = \sqrt{\gamma p/\rho}$  is the adiabatic sound speed and  $q$  is the gradient of the heat addition per unit mass.  $r_0$  and  $e_0$  are the radius and total energy at the inner boundary. By substituting  $a_s^2$  in Equation (1.7) into Equation (1.6) and expressing the momentum equation in terms of the Mach number ( $M_s = u/a_s$ ), one can find that

$$\frac{M_s^2 - 1}{M_s^2} \frac{dM_s^2}{dr} = 2 \frac{(\gamma - 1)M_s^2 + 2}{e + GM_\star/r} \left[ \frac{2}{r} \left( e + \frac{GM_\star}{r} \right) + \frac{\gamma + 1}{2(\gamma - 1)} \left( f - \frac{GM_\star}{r^2} \right) - \frac{\gamma M_s^2 + 1}{2} q \right]. \quad (1.8)$$

Based on the above, [Lamers and Cassinelli \(1999\)](#) summarized the general behavior of the transonic solution as a response to the heat or momentum deposition. Namely, (a) adding  $f > 0$  in the subsonic region ( $M_s^2 - 1 < 0$ ) leads to the decrease in  $dM_s^2/dr$  of the subsonic part of the transonic solution, while the temperature structure does not change. This requires the higher initial velocity ( $u_0 = u(r_0)$ ), and results in the increase in the mass-loss rate ( $\dot{M} = \rho_0 u_0 r_0^2$ ). (b) Adding heat ( $q > 0$ ) in the subsonic region leads to the increase in the stellar wind temperature and decrease in the outward pressure gradient. These result in smaller radius of sonic point ( $r_c \sim GM_\star/(2a_s^2)$ ) and increase in the density at that point ( $\rho_c$ ). Consequently, the mass-loss rate  $\dot{M} \sim \rho_c a_s r_c^2$  increases. On the other hand, Equation (1.8) shows the increase in  $dM_s^2/dr$  by heat deposition in the subsonic region, which indicates higher velocities in the subsonic region. (c) Adding

<sup>2</sup>To be exact, [Parker \(1958\)](#) assumed the isothermal atmosphere from  $r = a$ , which is the inner boundary, to “some radius”  $r = b$ .

momentum or energy in the supersonic region does not affect the mass-loss rate, but it results in higher velocities in the supersonic region. These general discussions are consistent with the numerical experiments by Leer and Holzer (1980).

Since the fluctuation of interplanetary magnetic field was reported by Neugebauer and Snyder (1962) and Coleman et al. (1962), Parker (1965) suggested that Alfvén waves in the solar wind possibly do work on the wind because of the centrifugal force  $\frac{1}{2}\rho|\delta v^2|/r$  and the average additional pressure  $\frac{1}{2}|\delta B^2|/8\pi$ , where  $\delta v$  and  $\delta B$  represent the velocity and magnetic fluctuations, respectively. The propagation of Alfvén wave in the steady stellar wind is described by the transverse components of equation of motion and induction equation.

$$\frac{\partial(r\delta v)}{\partial t} + v_r \frac{\partial(r\delta v)}{\partial r} - \frac{B_r}{4\pi\rho} \frac{\partial(r\delta B)}{\partial r} = 0, \quad (1.9)$$

$$\frac{\partial(r\delta B)}{\partial t} + \frac{\partial}{\partial r}\{r(v_r\delta B - \delta v B_r)\} = 0. \quad (1.10)$$

Dewar (1970) and Jacques (1977) formulated this kind of acceleration as a reaction of waves on the background medium. When the interaction between Alfvén waves and stellar wind is taken into account, the outward directed force per unit mass ( $f$ ) in Equation (1.6) can be expressed as

$$f = -\frac{dP_A}{dr}, \quad (1.11)$$

where  $P_A$  is called *Alfvén wave pressure* and expressed with Elsässer variables  $z_{\pm}$  as follows:

$$P_A = \frac{1}{2}(w_+ + w_-), \quad w_{\pm} = \frac{\rho z_{\pm}^2}{4}, \quad z_{\pm} = \delta v \pm \frac{\delta B}{\sqrt{4\pi\rho}} \quad (1.12)$$

where  $w_+$  and  $w_-$  represent the wave energy density transported to the anti-parallel and parallel direction of the background magnetic field, respectively. The equations for wave energy transfer are written as follows:

$$\frac{\partial}{\partial t} \left( \frac{w_{\pm}}{\omega'} \right) + \frac{1}{r^2} \frac{\partial}{\partial r} \left( r^2 \frac{w_{\pm}}{\omega'} (u \mp V_A) \right) = 0, \quad (1.13)$$

where  $V_A$  is the Alfvén speed, and  $\omega' = \omega V_A / (u \mp V_A)$  is the Doppler shifted frequency of Alfvén wave. These equations originate in the transverse components of equation of motion and induction equation.

By extending this formulation, numerous theoretical studies have addressed the solar and stellar wind modelings (Alazraki and Couturier, 1971; Heinemann and Olbert, 1980; Holzer et al., 1983; Cranmer and van Ballegooijen, 2005; Cranmer et al., 2007). In these works, the right-hand side of Equation (1.13) is usually set to a non-zero value. That means the phenomenological terms describing the wave reflection and wave dissipation are introduced as the functions of the coupling terms ( $w_+ w_-$ ). More recently, the three-dimensional (3D) global MHD modeling has been developed by implementing this approach (van der Holst et al., 2014). Their Alfvén Wave Solar Model (AWSoM) is also used to investigate the solar and stellar wind (Alvarado-Gómez et al., 2016, 2018), including the M-dwarf’s wind (Cohen et al., 2014; Garraffo et al., 2016, 2017; Dong et al., 2018; Alvarado-Gómez et al., 2020). These 3D modelings enable them to investigate the global structure of stellar wind and magnetic field configuration because the difference between the closed field and open field is naturally reproduced. However, this approach has the following three serious drawbacks. First, because of their low spatial resolution, the velocity and magnetic field are inevitably divided into the background and wave components in these modelings. This assumption is associated with the non-self-consistent concepts about “wave pressure”, “wave dissipation rate”, “wave reflection rate” which need to be implemented in the equation of motion and energy equation so that the interaction between the background

and wave components is taken into consideration. Second, because only Alfvén wave is considered as the wave component in these modelings, the stellar wind acceleration and heating by compressible wave are totally neglected. Note that it has been revealed that the compressible wave excited by large-amplitude Alfvén wave plays a key role in accelerating the stellar wind (Chapter 3) and both reflection and dissipation of Alfvén wave (Shoda et al., 2019). Finally, their inner boundary is set to the so-called stellar “coronal base” or “upper chromosphere” although the physical quantities at this height can be neither theoretically nor observationally constrained. In particular, Alfvén wave energy flux on the inner boundary is not clearly related to that excited by the convective motion on the photosphere. That means the origin of Alfvén wave in these modelings is totally arbitrary.

From a different perspective, Suzuki and Inutsuka (2005, 2006) performed the time-dependent, compressible, one-dimensional magnetohydrodynamics simulations of the solar wind along a single open flux tube. In their simulation, the nonlinear propagation of Alfvén wave in the non-steady solar wind was fully resolved. The similar approach is applied to the various stellar winds (Suzuki, 2007; Suzuki et al., 2013; Tanaka et al., 2014, 2015; Yasuda et al., 2019; Suzuki, 2018; Shoda et al., 2020), and extended to the multi-dimensional simulations (Matsumoto and Suzuki, 2012; Matsumoto and Suzuki, 2014; Shoda et al., 2019; Matsumoto, 2021). It should be noted that, however, the driving force of stellar wind has not been clarified in these studies. Suzuki and Inutsuka (2006) concluded that the fast solar wind in their simulation is driven by the wave pressure rather than by the thermal pressure. On the other hand, they also explained that, by referring to Lamers and Cassinelli (1999), the energy and momentum inputs in the supersonic region gives higher wind speed, while those in the subsonic region raises the mass flux of the wind by an increase of the density. These arguments are inconsistent with each other. When the wind is accelerated by the wave pressure,  $f$  in the right-hand side of Equation (1.8) implicitly depends on the velocity gradient of the wind. The discussion based on Equation (1.8) is less helpful in such a case as noted by Lamers and Cassinelli (1999), because the definition of the critical point deviates from the sonic point. Therefore, it is crucially important to confirm whether the stellar winds in these simulations are magnetically accelerated or not, by investigating the acceleration force  $f$  directly.

In this thesis, we further extend the above single-flux-tube modeling of Alfvén-wave-driven solar and stellar wind. In Chapter 2, which is based on Sakaue and Shibata (2020), we present the simulation results of solar atmosphere and wind, and focus on the energy transfer by nonlinear Alfvén waves in the solar chromosphere. In Chapter 3, which is based on Sakaue and Shibata (2021), we extend our study to the M-dwarfs’ atmospheres and winds, and discuss the similarities and differences among the simulated solar and M-dwarfs’ atmospheres and winds.

## Bibliography

Alazraki, G. and P. Couturier

1971. Solar Wind Acceleration Caused by the Gradient of Alfvén Wave Pressure. *A&A*, 13:380.

Alvarado-Gómez, J. D., J. J. Drake, O. Cohen, S. P. Moschou, and C. Garraffo

2018. Suppression of Coronal Mass Ejections in Active Stars by an Overlying Large-scale Magnetic Field: A Numerical Study. *ApJ*, 862(2):93.

Alvarado-Gómez, J. D., J. J. Drake, F. Fraschetti, C. Garraffo, O. Cohen, C. Vocks, K. Poppenhäger, S. P. Moschou, R. K. Yadav, and I. Manchester, Ward B.

2020. Tuning the Exospace Weather Radio for Stellar Coronal Mass Ejections. *ApJ*, 895(1):47.

- Alvarado-Gómez, J. D., G. A. J. Hussain, O. Cohen, J. J. Drake, C. Garraffo, J. Grunhut, and T. I. Gombosi  
2016. Simulating the environment around planet-hosting stars. II. Stellar winds and inner astrospheres. *A&A*, 594:A95.
- Antolin, P., I. De Moortel, T. Van Doorselaere, and T. Yokoyama  
2016. Modeling Observed Decay-less Oscillations as Resonantly Enhanced Kelvin-Helmholtz Vortices from Transverse MHD Waves and Their Seismological Application. *ApJL*, 830(2):L22.
- Antolin, P. and K. Shibata  
2010. The Role Of Torsional Alfvén Waves in Coronal Heating. *ApJ*, 712(1):494–510.
- Astudillo-Defru, N., X. Delfosse, X. Bonfils, T. Forveille, C. Lovis, and J. Rameau  
2017. Magnetic activity in the HARPS M dwarf sample. The rotation-activity relationship for very low-mass stars through  $R'_{HK}$ . *A&A*, 600:A13.
- Athay, R. G.  
1976. *The solar chromosphere and corona: Quiet sun*, volume 53. Dordrecht: Reidel.
- Audard, M., M. Güdel, J. J. Drake, and V. L. Kashyap  
2000. Extreme-Ultraviolet Flare Activity in Late-Type Stars. *ApJ*, 541(1):396–409.
- Ayres, T. R.  
1997. Evolution of the solar ionizing flux. *JGR*, 102(E1):1641–1652.
- Ayres, T. R., J. L. Linsky, G. S. Vaiana, L. Golub, and R. Rosner  
1981. The cool Half of the H-R diagram in soft X-rays. *ApJ*, 250:293–299.
- Baliunas, S. L., R. A. Donahue, W. H. Soon, J. H. Horne, J. Frazer, L. Woodard-Eklund, M. Bradford, L. M. Rao, O. C. Wilson, Q. Zhang, W. Bennett, J. Briggs, S. M. Carroll, D. K. Duncan, D. Figueroa, H. H. Lanning, T. Misch, J. Mueller, R. W. Noyes, D. Poppe, A. C. Porter, C. R. Robinson, J. Russell, J. C. Shelton, T. Soyumer, A. H. Vaughan, and J. H. Whitney  
1995. Chromospheric Variations in Main-Sequence Stars. II. *ApJ*, 438:269.
- Baliunas, S. L., L. Hartmann, R. W. Noyes, H. Vaughan, G. W. Preston, J. Frazer, H. Lanning, F. Middelkoop, and D. Mihalas  
1983. Stellar rotation in lower main-sequence stars measured from time variations in H and K emission-line fluxes. II. Detailed analysis of the 1980 observing season data. *ApJ*, 275:752–772.
- Beckers, J. M.  
1972. Solar Spicules. *ARA&A*, 10:73.
- Beck, B., M. Schüssler, R. H. Cameron, and A. Reiners  
2015. Three-dimensional simulations of near-surface convection in main-sequence stars. III. The structure of small-scale magnetic flux concentrations. *A&A*, 581:A42.
- Berger, E., G. Basri, T. A. Fleming, M. S. Giampapa, J. E. Gizis, J. Liebert, E. Martín, N. Phan-Bao, and R. E. Rutledge  
2010. Simultaneous Multi-Wavelength Observations of Magnetic Activity in Ultracool Dwarfs. III. X-ray, Radio, and  $H\alpha$  Activity Trends in M and L dwarfs. *ApJ*, 709(1):332–341.
- Bidelman, W. P.  
1954. Catalogue and Bibliography of Emission-Line Stars of Types Later than B. *ApJS*, 1:175.

Biermann, L.

1946. Zur Deutung der chromosphärischen Turbulenz und des Exzesses der UV-Strahlung der Sonne. *Naturwissenschaften*, 33(4):118–119.

Böhm-Vitense, E. and T. Dettmann

1980. The boundary line in the H-R diagram for stellar chromospheres and the theory of convection. *ApJ*, 236:560–566.

Bourrier, V., A. Lecavelier des Etangs, D. Ehrenreich, Y. A. Tanaka, and A. A. Vidotto

2016. An evaporating planet in the wind: stellar wind interactions with the radiatively braked exosphere of GJ 436 b. *A&A*, 591:A121.

Bray, R. J. and R. E. Loughhead

1974. *The solar chromosphere*. London: Chapman and Hall.

Browning, M. K., G. Basri, G. W. Marcy, A. A. West, and J. Zhang

2010. Rotation and Magnetic Activity in a Sample of M-Dwarfs. *AJ*, 139(2):504–518.

Buchholz, B., P. Ulmschneider, and M. Cuntz

1998. Basal Heating in Main-Sequence Stars and Giants: Results from Monochromatic Acoustic Wave Models. *ApJ*, 494(2):700–714.

Burrows, A. and J. Liebert

1993. The science of brown dwarfs. *Reviews of Modern Physics*, 65(2):301–336.

Cohen, O., J. J. Drake, A. Gloer, C. Garraffo, K. Poppenhaeager, J. M. Bell, A. J. Ridley, and T. I. Gombosi

2014. Magnetospheric Structure and Atmospheric Joule Heating of Habitable Planets Orbiting M-dwarf Stars. *ApJ*, 790(1):57.

Cohen, O., Y. Ma, J. J. Drake, A. Gloer, C. Garraffo, J. M. Bell, and T. I. Gombosi

2015. The Interaction of Venus-like, M-dwarf Planets with the Stellar Wind of Their Host Star. *ApJ*, 806(1):41.

Coleman, P. J., J., J. Davis, Leverett, E. J. Smith, and C. P. Sonett

1962. Interplanetary Magnetic Fields. *Science*, 138(3545):1099–1100.

Cook, B. A., P. K. G. Williams, and E. Berger

2014. Trends in Ultracool Dwarf Magnetism. II. The Inverse Correlation Between X-Ray Activity and Rotation as Evidence for a Bimodal Dynamo. *ApJ*, 785(1):10.

Cram, L. E. and D. J. Mullan

1979. Model chromospheres of flare stars. I. Balmer-line profiles. *ApJ*, 234:579–587.

Cram, L. E. and D. J. Mullan

1985. Formation of the H-alpha absorption line in the chromospheres of cool stars. *ApJ*, 294:626–633.

Cranmer, S. R., S. E. Gibson, and P. Riley

2017. Origins of the Ambient Solar Wind: Implications for Space Weather. *SSRv*, 212(3-4):1345–1384.

Cranmer, S. R. and A. A. van Ballegoijen

2005. On the Generation, Propagation, and Reflection of Alfvén Waves from the Solar Photosphere to the Distant Heliosphere. *ApJS*, 156(2):265–293.

- Cranmer, S. R., A. A. van Ballegoijen, and R. J. Edgar  
2007. Self-consistent Coronal Heating and Solar Wind Acceleration from Anisotropic Magnetohydrodynamic Turbulence. *ApJS*, 171(2):520–551.
- Cuntz, M., W. Rammacher, P. Ulmschneider, Z. E. Musielak, and S. H. Saar  
1999. Two-Component Theoretical Chromosphere Models for K Dwarfs of Different Magnetic Activity: Exploring the Ca II Emission-Stellar Rotation Relationship. *ApJ*, 522(2):1053–1068.
- Cuntz, M., P. Ulmschneider, and Z. E. Musielak  
1998. Self-Consistent and Time-Dependent Magnetohydrodynamic Chromosphere Models for Magnetically Active Stars. *ApJL*, 493(2):L117–L120.
- Delfosse, X., T. Forveille, C. Perrier, and M. Mayor  
1998. Rotation and chromospheric activity in field M dwarfs. *A&A*, 331:581–595.
- Derby, N. F., J.  
1978. Modulational instability of finite-amplitude, circularly polarized Alfvén waves. *ApJ*, 224:1013–1016.
- Dewar, R. L.  
1970. Interaction between Hydromagnetic Waves and a Time-Dependent, Inhomogeneous Medium. *Physics of Fluids*, 13(11):2710–2720.
- Dikpati, M. and P. Charbonneau  
1999. A Babcock-Leighton Flux Transport Dynamo with Solar-like Differential Rotation. *ApJ*, 518(1):508–520.
- Donati, J. F., J. Morin, P. Petit, X. Delfosse, T. Forveille, M. Aurière, R. Cabanac, B. Dintrans, R. Fares, T. Gastine, M. M. Jardine, F. Lignières, F. Paletou, J. C. Ramirez Velez, and S. Théado  
2008. Large-scale magnetic topologies of early M dwarfs. *MNRAS*, 390(2):545–560.
- Dong, C., M. Jin, M. Lingam, V. S. Airapetian, Y. Ma, and B. van der Holst  
2018. Atmospheric escape from the TRAPPIST-1 planets and implications for habitability. *Proceedings of the National Academy of Science*, 115(2):260–265.
- Dong, C., M. Lingam, Y. Ma, and O. Cohen  
2017. Is Proxima Centauri b Habitable? A Study of Atmospheric Loss. *ApJL*, 837(2):L26.
- Driscoll, P. E. and R. Barnes  
2015. Tidal Heating of Earth-like Exoplanets around M Stars: Thermal, Magnetic, and Orbital Evolutions. *Astrobiology*, 15(9):739–760.
- Duncan, D. K., A. H. Vaughan, O. C. Wilson, G. W. Preston, J. Frazer, H. Lanning, A. Misch, J. Mueller, D. Soyumer, L. Woodard, S. L. Baliunas, R. W. Noyes, L. W. Hartmann, A. Porter, C. Zwaan, F. Middelkoop, R. G. M. Rutten, and D. Mihalas  
1991. CA II H and K Measurements Made at Mount Wilson Observatory, 1966–1983. *ApJS*, 76:383.
- Edlén, B.  
1943. Die Deutung der Emissionslinien im Spektrum der Sonnenkorona. Mit 6 Abbildungen. *Zeitschrift für Astrophysik*, 22:30.

- Fawzy, D. E. and K. Stepień  
 2018. Theoretical basal Ca II fluxes for late-type stars: results from magnetic wave models with time-dependent ionization and multi-level radiation treatments. *Ap&SS*, 363(3):57.
- Fleming, T. A., M. S. Giampapa, and D. Garza  
 2003. The Quiescent Corona of VB 10. *ApJ*, 594(2):982–986.
- Fontenla, J., E. J. Reichmann, and E. Tandberg-Hanssen  
 1988. The Lyman-Alpha Line in Various Solar Features. I. Observations. *ApJ*, 329:464.
- Fontenla, J. M., J. Harder, W. Livingston, M. Snow, and T. Woods  
 2011. High-resolution solar spectral irradiance from extreme ultraviolet to far infrared. *Journal of Geophysical Research (Atmospheres)*, 116(D20):D20108.
- Fontenla, J. M., J. L. Linsky, J. Witbrod, K. France, A. Buccino, P. Mauas, M. Vieytes, and L. M. Walkowicz  
 2016. Semi-empirical Modeling of the Photosphere, Chromosphere, Transition Region, and Corona of the M-dwarf Host Star GJ 832. *ApJ*, 830(2):154.
- Gabriel, A. H.  
 1976. A Magnetic Model of the Solar Transition Region. *Philosophical Transactions of the Royal Society of London Series A*, 281(1304):339–352.
- Garraffo, C., J. J. Drake, and O. Cohen  
 2016. The Space Weather of Proxima Centauri b. *ApJL*, 833(1):L4.
- Garraffo, C., J. J. Drake, O. Cohen, J. D. Alvarado-Gómez, and S. P. Moschou  
 2017. The Threatening Magnetic and Plasma Environment of the TRAPPIST-1 Planets. *ApJL*, 843(2):L33.
- Gilman, P. A.  
 1980. *Differential rotation in stars with convection zones*, volume 114, Pp. 19–37.
- Gizis, J. E., D. G. Monet, I. N. Reid, J. D. Kirkpatrick, J. Liebert, and R. J. Williams  
 2000. New Neighbors from 2MASS: Activity and Kinematics at the Bottom of the Main Sequence. *AJ*, 120(2):1085–1099.
- Goldreich, P. and S. Sridhar  
 1995. Toward a Theory of Interstellar Turbulence. II. Strong Alfvénic Turbulence. *ApJ*, 438:763.
- Goldstein, M. L.  
 1978. An instability of finite amplitude circularly polarized Alfvén waves. *ApJ*, 219:700–704.
- Harvey, K. L. and O. R. White  
 1999. Magnetic and Radiative Variability of Solar Surface Structures. I. Image Decomposition and Magnetic-Intensity Mapping. *ApJ*, 515(2):812–831.
- Heinemann, M. and S. Olbert  
 1980. Non-WKB Alfvén waves in the solar wind. *JGR*, 85(A3):1311–1327.
- Helfand, D. J. and J. P. Caillault  
 1982. An unbiased survey of field star X-ray emission. *ApJ*, 253:760–767.
- Heyvaerts, J. and E. R. Priest  
 1983. Coronal heating by phase-mixed shear Alfvén waves. *A&A*, 117:220–234.

Hollweg, J. V.

.

Hollweg, J. V.

1982. On the origin of solar spicules. *ApJ*, 257:345–353.

Hollweg, J. V., S. Jackson, and D. Galloway

1982. Alfvén Waves in the Solar Atmospheres - Part Three - Nonlinear Waves on Open Flux Tubes. *Sol. Phys.*, 75(1-2):35–61.

Holzer, T. E., T. Fla, and E. Leer

1983. Alfvén waves in stellar winds. *ApJ*, 275:808–835.

Houdebine, E. R. and J. G. Doyle

1994. Observation and modelling of main sequence star chromospheres I. Modelling of the hydrogen spectrum in dMe stars. *A&A*, 289:169–184.

Houdebine, E. R. and H. C. Stempels

1997. Observation and modelling of main sequence stellar chromospheres. VI.  $H_{\alpha}$ - and CaII line observations of M1 dwarfs and comparison with models. *A&A*, 326:1143–1166.

Hünsch, M., J. H. M. M. Schmitt, and W. Voges

1998. The ROSAT all-sky survey catalogue of optically bright late-type giants and supergiants. *A&AS*, 127:251–255.

Hünsch, M. and K. P. Schroeder

1996. The revised X-ray dividing line: new light on late stellar activity. *A&A*, 309:L51–L54.

Ionson, J. A.

1978. Resonant absorption of Alfvénic surface waves and the heating of solar coronal loops. *ApJ*, 226:650–673.

Jacques, S. A.

1977. Momentum and energy transport by waves in the solar atmosphere and solar wind. *ApJ*, 215:942–951.

Jefferies, J. T. and N. D. Morrison

1973. *Temperature Distribution in a Stellar Atmosphere, Diagnostic Basis*, volume 317, P. 3.

Johannesson, A. and H. Zirin

1996. The Pole-Equator Variation of Solar Chromospheric Height. *ApJ*, 471:510.

Kaltenegger, L. and W. A. Traub

2009. Transits of Earth-like Planets. *ApJ*, 698(1):519–527.

Kasting, J. F., D. P. Whitmire, and R. T. Reynolds

1993. Habitable Zones around Main Sequence Stars. *ICARUS*, 101(1):108–128.

Kellett, B. J. and V. Tsikoudi

1997. EUV activity in late-type stars during the ROSAT WFC All-Sky Survey - II. Comparisons with other observations. *MNRAS*, 288(2):411–420.

Kim, Y.-C. and P. Demarque

1996. The Theoretical Calculation of the Rossby Number and the “Nonlocal” Convective Overturn Time for Pre-Main-Sequence and Early Post-Main-Sequence Stars. *ApJ*, 457:340.

Kochukhov, O.

2021. Magnetic fields of M dwarfs. *A&ARv*, 29(1):1.

Kodaira, K., K. Ichimura, and S. Nishimura

1976. High-speed five-color photometry of the flare star EV Lacertae. *PASJ*, 28:665–674.

Kopparapu, R. k., E. T. Wolf, G. Arney, N. E. Batalha, J. Haqq-Misra, S. L. Grimm, and K. Heng

2017. Habitable Moist Atmospheres on Terrestrial Planets near the Inner Edge of the Habitable Zone around M Dwarfs. *ApJ*, 845(1):5.

Kraft, R. P.

1967. Studies of Stellar Rotation. V. The Dependence of Rotation on Age among Solar-Type Stars. *ApJ*, 150:551.

Kraichnan, R. H.

1965. Inertial-Range Spectrum of Hydromagnetic Turbulence. *Physics of Fluids*, 8(7):1385–1387.

Lamers, H. J. G. L. M. and J. P. Cassinelli

1999. *Introduction to Stellar Winds*. Cambridge, UK: Cambridge University Press.

Lammer, H., M. Güdel, Y. Kulikov, I. Ribas, T. V. Zaqarashvili, M. L. Khodachenko, K. G. Kislyakova,

H. Gröller, P. Odert, M. Leitzinger, B. Fichtinger, S. Krauss, W. Hausleitner, M. Holmström, J. Sanz-Forcada, H. I. M. Lichtenegger, A. Hansmeier, V. I. Shematovich, D. Bisikalo, H. Rauer, and M. Fridlund  
2012. Variability of solar/stellar activity and magnetic field and its influence on planetary atmosphere evolution. *Earth, Planets, and Space*, 64(2):179–199.

Leer, E. and T. E. Holzer

1980. Energy addition in the solar wind. *JGR*, 85:4681–4688.

Linsky, J. L.

1980. Stellar chromospheres. *ARA&A*, 18:439–488.

Linsky, J. L. and B. M. Haisch

1979. Outer atmospheres of cool stars. I. The sharp division into solar-type and non-solar-type stars. *ApJL*, 229:L27–L32.

Linsky, J. L., B. E. Wood, A. Youngblood, A. Brown, C. S. Froning, K. France, A. P. Buccino, S. R. Cranmer, P. Mauas, Y. Miguel, J. S. Pineda, S. Rugheimer, M. Veytes, P. J. Wheatley, and D. J. Wilson

2020. The Relative Emission from Chromospheres and Coronae: Dependence on Spectral Type and Age. *ApJ*, 902(1):3.

Lippincott, S. L.

1957. Chromospheric Spicules. *Smithsonian Contributions to Astrophysics*, 2:15.

Maehara, H., T. Shibayama, S. Notsu, Y. Notsu, T. Nagao, S. Kusaba, S. Honda, D. Nogami, and K. Shibata

2012. Superflares on solar-type stars. *Nature*, 485(7399):478–481.

- Maggio, A., S. Sciortino, G. S. Vaiana, P. Majer, J. Bookbinder, L. Golub, J. Harnden, F. R., and R. Rosner  
1987. Einstein Observatory Survey of X-Ray Emission from Solar-Type Stars: The Late F and G Dwarf Stars. *ApJ*, 315:687.
- Mamajek, E. E. and L. A. Hillenbrand  
2008. Improved Age Estimation for Solar-Type Dwarfs Using Activity-Rotation Diagnostics. *ApJ*, 687(2):1264–1293.
- Martínez-Arnáiz, R., J. López-Santiago, I. Crespo-Chacón, and D. Montes  
2011. Effect of magnetic activity saturation in chromospheric flux-flux relationships. *MNRAS*, 414(3):2629–2641.
- Mathioudakis, M., A. Fruscione, J. J. Drake, K. McDonald, S. Bowyer, and R. F. Malina  
1995. Activity versus rotation in the extreme ultraviolet. *A&A*, 300:775.
- Matsumoto, T.  
2016. Competition between shock and turbulent heating in coronal loop system. *MNRAS*, 463(1):502–511.
- Matsumoto, T.  
2018. Thermal responses in a coronal loop maintained by wave heating mechanisms. *MNRAS*, 476(3):3328–3335.
- Matsumoto, T.  
2021. Full compressible 3D MHD simulation of solar wind. *MNRAS*, 500(4):4779–4787.
- Matsumoto, T. and K. Shibata  
2010. Nonlinear Propagation of Alfvén Waves Driven by Observed Photospheric Motions: Application to the Coronal Heating and Spicule Formation. *ApJ*, 710(2):1857–1867.
- Matsumoto, T. and T. K. Suzuki  
2012. Connecting the Sun and the Solar Wind: The First 2.5-dimensional Self-consistent MHD Simulation under the Alfvén Wave Scenario. *ApJ*, 749(1):8.
- Matsumoto, T. and T. K. Suzuki  
2014. Connecting the Sun and the solar wind: the self-consistent transition of heating mechanisms. *MNRAS*, 440(2):971–986.
- Mauas, P. J. D. and A. Falchi  
1994. Atmospheric Models of Flare Stars: The Quiescent State of AD Leonis. *A&A*, 281:129–138.
- McLean, M., E. Berger, and A. Reiners  
2012. The Radio Activity-Rotation Relation of Ultracool Dwarfs. *ApJ*, 746(1):23.
- Miyamoto, S.  
1949. Ionization Theory of Solar Corona. *PASJ*, 1:10.
- Mohanty, S. and G. Basri  
2003. Rotation and Activity in Mid-M to L Field Dwarfs. *ApJ*, 583(1):451–472.
- Morin, J., J. F. Donati, P. Petit, X. Delfosse, T. Forveille, L. Albert, M. Aurière, R. Cabanac, B. Dintrans, R. Fares, T. Gastine, M. M. Jardine, F. Lignières, F. Paletou, J. C. Ramirez Velez, and S. Théado  
2008. Large-scale magnetic topologies of mid M dwarfs. *MNRAS*, 390(2):567–581.

- Morin, J., J. F. Donati, P. Petit, X. Delfosse, T. Forveille, and M. M. Jardine  
 2010. Large-scale magnetic topologies of late M dwarfs\*. *MNRAS*, 407(4):2269–2286.
- Moriyasu, S., T. Kudoh, T. Yokoyama, and K. Shibata  
 2004. The Nonlinear Alfvén Wave Model for Solar Coronal Heating and Nanoflares. *ApJL*, 601(1):L107–L110.
- Mullan, D. J. and Q. Q. Cheng  
 1993. MG II and LY alpha Fluxes in M Dwarfs: Evaluation of an Acoustic Model. *ApJ*, 412:312.
- Mullan, D. J. and Q. Q. Cheng  
 1994. Acoustic Waves in M Dwarfs: Maintaining a Corona. *ApJ*, 420:392.
- Munro, R. H. and G. L. Withbroe  
 1972. Properties of a Coronal “hole” Derived from Extreme-Ultraviolet Observations. *ApJ*, 176:511.
- Namekata, K., H. Maehara, Y. Notsu, S. Toriumi, H. Hayakawa, K. Ikuta, S. Notsu, S. Honda, D. Nogami, and K. Shibata  
 2019. Lifetimes and Emergence/Decay Rates of Star Spots on Solar-type Stars Estimated by Kepler Data in Comparison with Those of Sunspots. *ApJ*, 871(2):187.
- Narain, U. and P. Ulmschneider  
 1990. Chromospheric and Coronal Heating Mechanisms. *SSRv*, 54(3-4):377–445.
- Narain, U. and P. Ulmschneider  
 1996. Chromospheric and Coronal Heating Mechanisms II. *SSRv*, 75(3-4):453–509.
- Neugebauer, M. and C. W. Snyder  
 1962. Solar Plasma Experiment. *Science*, 138(3545):1095–1097.
- Newton, E. R., J. Irwin, D. Charbonneau, P. Berlind, M. L. Calkins, and J. Mink  
 2017. The H $\alpha$  Emission of Nearby M Dwarfs and its Relation to Stellar Rotation. *ApJ*, 834(1):85.
- Noyes, R. W., L. W. Hartmann, S. L. Baliunas, D. K. Duncan, and A. H. Vaughan  
 1984. Rotation, convection, and magnetic activity in lower main-sequence stars. *ApJ*, 279:763–777.
- Ofman, L. and J. M. Davila  
 1995. Nonlinear resonant absorption of Alfvén waves in three dimensions, scaling laws, and coronal heating. *JGR*, 100(A12):23427–23442.
- Ofman, L., J. M. Davila, and R. S. Steinolfson  
 1994. Nonlinear studies of coronal heating by the resonant absorption of Alfvén waves. *GeoRL*, 21(20):2259–2262.
- Oranje, B. J.  
 1986. Magnetic structure in cool stars. IX. Ultraviolet emission lines from chromospheres and transition regions. *A&A*, 154:185–196.
- Osterbrock, D. E.  
 1961. The Heating of the Solar Chromosphere, Plages, and Corona by Magnetohydrodynamic Waves. *ApJ*, 134:347.

- Owen, J. E. and S. Mohanty  
2016. Habitability of terrestrial-mass planets in the HZ of M Dwarfs - I. H/He-dominated atmospheres. *MNRAS*, 459(4):4088–4108.
- Pallavicini, R., L. Golub, R. Rosner, G. S. Vaiana, T. Ayres, and J. L. Linsky  
1981. Relations among stellar X-ray emission observed from Einstein, stellar rotation and bolometric luminosity. *ApJ*, 248:279–290.
- Parker, E. N.  
1955. Hydromagnetic Dynamo Models. *ApJ*, 122:293.
- Parker, E. N.  
1958. Dynamics of the Interplanetary Gas and Magnetic Fields. *ApJ*, 128:664.
- Parker, E. N.  
1965. Dynamical Theory of the Solar Wind. *SSRv*, 4(5-6):666–708.
- Parker, E. N.  
1978. Hydraulic concentration of magnetic fields in the solar photosphere. VI. Adiabatic cooling and concentration in downdrafts. *ApJ*, 221:368–377.
- Pasachoff, J. M.  
2017. Heliophysics at total solar eclipses. *Nature Astronomy*, 1:0190.
- Peacock, S., T. Barman, E. L. Shkolnik, P. H. Hauschildt, and E. Baron  
2019a. Predicting the Extreme Ultraviolet Radiation Environment of Exoplanets around Low-mass Stars: The TRAPPIST-1 System. *ApJ*, 871(2):235.
- Peacock, S., T. Barman, E. L. Shkolnik, P. H. Hauschildt, E. Baron, and B. Fuhrmeister  
2019b. Predicting the Extreme Ultraviolet Radiation Environment of Exoplanets around Low-mass Stars: GJ 832, GJ 176, and GJ 436. *ApJ*, 886(2):77.
- Peacock, S., T. Barman, E. L. Shkolnik, R. O. P. Loyd, A. C. Schneider, I. Pagano, and V. S. Meadows  
2020. HAZMAT VI: The Evolution of Extreme Ultraviolet Radiation Emitted from Early M Stars. *ApJ*, 895(1):5.
- Pereira, T. M. D., B. De Pontieu, and M. Carlsson  
2012. Quantifying Spicules. *ApJ*, 759(1):18.
- Pevtsov, A. A., G. H. Fisher, L. W. Acton, D. W. Longcope, C. M. Johns-Krull, C. C. Kankelborg, and T. R. Metcalf  
2003. The Relationship Between X-Ray Radiance and Magnetic Flux. *ApJ*, 598(2):1387–1391.
- Pevtsov, A. A., I. Virtanen, K. Mursula, A. Tlatov, and L. Bertello  
2016. Reconstructing solar magnetic fields from historical observations. I. Renormalized Ca K spectroheliograms and pseudo-magnetograms. *A&A*, 585:A40.
- Phillips, K. J. H., U. Feldman, and E. Landi  
2008. *Ultraviolet and X-ray Spectroscopy of the Solar Atmosphere*. Cambridge, UK: Cambridge University Press.

- Pizzolato, N., A. Maggio, G. Micela, S. Sciortino, and P. Ventura  
 2003. The stellar activity-rotation relationship revisited: Dependence of saturated and non-saturated X-ray emission regimes on stellar mass for late-type dwarfs. *A&A*, 397:147–157.
- Rajaguru, S. P., R. L. Kurucz, and S. S. Hasan  
 2002. Convective Intensification of Magnetic Flux Tubes in Stellar Photospheres. *ApJL*, 565(2):L101–L104.
- Reid, I. N. and S. L. Hawley  
 2005. *New light on dark stars : red dwarfs, low-mass stars, brown dwarfs*. Springer-Verlag Berlin Heidelberg.
- Reiners, A.  
 2012. Observations of Cool-Star Magnetic Fields. *Living Reviews in Solar Physics*, 9(1):1.
- Reiners, A. and G. Basri  
 2007. The First Direct Measurements of Surface Magnetic Fields on Very Low Mass Stars. *ApJ*, 656(2):1121–1135.
- Reiners, A., G. Basri, and M. Browning  
 2009. Evidence for Magnetic Flux Saturation in Rapidly Rotating M Stars. *ApJ*, 692(1):538–545.
- Reiners, A., N. Joshi, and B. Goldman  
 2012. A Catalog of Rotation and Activity in Early-M Stars. *AJ*, 143(4):93.
- Reiners, A., M. Schüssler, and V. M. Passegger  
 2014. Generalized Investigation of the Rotation-Activity Relation: Favoring Rotation Period instead of Rossby Number. *ApJ*, 794(2):144.
- Ribas, I., E. F. Guinan, M. Güdel, and M. Audard  
 2005. Evolution of the Solar Activity over Time and Effects on Planetary Atmospheres. I. High-Energy Irradiances (1-1700 Å). *ApJ*, 622(1):680–694.
- Rutten, R. G. M.  
 1987. Magnetic structure in cool stars. XII - Chromospheric activity and rotation of giants and dwarfs. *A&A*, 177(1-2):131–142.
- Rutten, R. G. M. and C. J. Schrijver  
 1987. Magnetic structure in cool stars. XIII - Appropriate units for the rotation-activity relation. *A&A*, 177(1-2):155–162.
- Rutten, R. G. M., C. J. Schrijver, C. Zwaan, D. K. Duncan, and R. Mewe  
 1989. Magnetic structure in cool stars. XVI. Emissions from the outer atmospheres of M-type dwarfs. *A&A*, 219:239–252.
- Saar, S. H.  
 1990. Magnetic Fields on Solar-like Stars: The First Decade. In *Solar Photosphere: Structure, Convection, and Magnetic Fields*, J. O. Stenflo, ed., volume 138, Pp. 427–441.
- Sakaue, T. and K. Shibata  
 2020. Energy Transfer by Nonlinear Alfvén Waves in the Solar Chromosphere and Its Effect on Spicule Dynamics, Coronal Heating, and Solar Wind Acceleration. *ApJ*, 900(2):120.

- Sakaue, T. and K. Shibata  
2021. Nonlinear Alfvén Wave Model of Stellar Coronae and Winds from the Sun to M Dwarfs. *ApJL*, 906(2):L13.
- Scalo, J., L. Kaltenegger, A. G. Segura, M. Fridlund, I. Ribas, Y. N. Kulikov, J. L. Grenfell, H. Rauer, P. Odert, M. Leitzinger, F. Selsis, M. L. Khodachenko, C. Eiroa, J. Kasting, and H. Lammer  
2007. M Stars as Targets for Terrestrial Exoplanet Searches And Biosignature Detection. *Astrobiology*, 7(1):85–166.
- Schatzman, E.  
1962. A theory of the role of magnetic activity during star formation. *Annales d’Astrophysique*, 25:18.
- Schrijver, C. J.  
1987. Magnetic structure in cool stars. XI. Relations between radiative fluxes measuring stellar activity, and evidence for two components in stellar chromospheres. *A&A*, 172:111–123.
- Schrijver, C. J.  
1995. Basal heating in the atmospheres of cool stars. *A&ARv*, 6(3):181–223.
- Schrijver, C. J. and R. G. M. Rutten  
1987. Magnetic structure in cool stars. XIV. Deficiency in chromospheric fluxes from M-type dwarfs. *A&A*, 177:143–149.
- Schrijver, C. J. and C. Zwaan  
2000. *Solar and Stellar Magnetic Activity*. New York: Cambridge University Press.
- Schrijver, C. J., C. Zwaan, C. W. Maxson, and R. W. Noyes  
1985. A study of ultraviolet and X-ray emissions of selected solar regions. *A&A*, 149(1):123–134.
- Schwarzschild, M.  
1948. On Noise Arising from the Solar Granulation. *ApJ*, 107:1.
- Seager, S.  
2013. Exoplanet Habitability. *Science*, 340(6132):577–581.
- Segura, A., L. M. Walkowicz, V. Meadows, J. Kasting, and S. Hawley  
2010. The Effect of a Strong Stellar Flare on the Atmospheric Chemistry of an Earth-like Planet Orbiting an M Dwarf. *Astrobiology*, 10(7):751–771.
- Shibata, K., T. Nishikawa, R. Kitai, and Y. Suematsu  
1982. Numerical Hydrodynamics of the Jet Phenomena in the Solar Atmosphere - Part Two - Surges. *Sol. Phys.*, 77(1-2):121–151.
- Shibata, K. and Y. Suematsu  
1982. Why are spicules absent over plages and long under coronal holes? *Sol. Phys.*, 78(2):333–345.
- Shibayama, T., H. Maehara, S. Notsu, Y. Notsu, T. Nagao, S. Honda, T. T. Ishii, D. Nogami, and K. Shibata  
2013. Superflares on Solar-type Stars Observed with Kepler. I. Statistical Properties of Superflares. *ApJS*, 209(1):5.
- Shoda, M., T. K. Suzuki, M. Asgari-Targhi, and T. Yokoyama  
2019. Three-dimensional Simulation of the Fast Solar Wind Driven by Compressible Magnetohydrodynamic Turbulence. *ApJL*, 880(1):L2.

- Shoda, M., T. K. Suzuki, S. P. Matt, S. R. Cranmer, A. A. Vidotto, A. Strugarek, V. See, V. Réville, A. J. Finley, and A. S. Brun  
 2020. Alfvén-wave-driven Magnetic Rotator Winds from Low-mass Stars. I. Rotation Dependences of Magnetic Braking and Mass-loss Rate. *ApJ*, 896(2):123.
- Shoda, M. and T. Yokoyama  
 2016. Nonlinear Reflection Process of Linearly Polarized, Broadband Alfvén Waves in the Fast Solar Wind. *ApJ*, 820(2):123.
- Shoda, M. and T. Yokoyama  
 2018. Anisotropic Magnetohydrodynamic Turbulence Driven by Parametric Decay Instability: The Onset of Phase Mixing and Alfvén Wave Turbulence. *ApJL*, 859(2):L17.
- Shulyak, D., A. Reiners, A. Engeln, L. Malo, R. Yadav, J. Morin, and O. Kochukhov  
 2017. Strong dipole magnetic fields in fast rotating fully convective stars. *Nature Astronomy*, 1:0184.
- Shulyak, D., A. Reiners, E. Nagel, L. Tal-Or, J. A. Caballero, M. Zechmeister, V. J. S. Béjar, M. Cortés-Contreras, E. L. Martin, A. Kaminski, I. Ribas, A. Quirrenbach, P. J. Amado, G. Anglada-Escudé, F. F. Bauer, S. Dreizler, E. W. Guenther, T. Henning, S. V. Jeffers, M. Kürster, M. Lafarga, D. Montes, J. C. Morales, and S. Pedraz  
 2019. Magnetic fields in M dwarfs from the CARMENES survey. *A&A*, 626:A86.
- Simon, T., G. Herbig, and A. M. Boesgaard  
 1985. The evolution of chromospheric activity and the spin-down of solar-type stars. *ApJ*, 293:551–574.
- Skumanich, A.  
 1972. Time Scales for Ca II Emission Decay, Rotational Braking, and Lithium Depletion. *ApJ*, 171:565.
- Slee, O. B. and R. T. Stewart  
 1989. Stellar radio luminosity and stellar rotation. *MNRAS*, 236:129–138.
- Spitzer, L. and R. Härm  
 1953. Transport Phenomena in a Completely Ionized Gas. *Physical Review*, 89(5):977–981.
- Sridhar, S. and P. Goldreich  
 1994. Toward a Theory of Interstellar Turbulence. I. Weak Alfvénic Turbulence. *ApJ*, 432:612.
- Steinolfson, R. S., E. J. Schmahl, and S. T. Wu  
 1979. Hydrodynamic simulations of flare/surge events. *Sol. Phys.*, 63(1):187–200.
- Stepien, K.  
 1994. Applicability of the Rossby number in activity-rotation relations for dwarfs and giants. *A&A*, 292:191–207.
- Sterling, A. C.  
 2000. Solar Spicules: A Review of Recent Models and Targets for Future Observations - (Invited Review). *Sol. Phys.*, 196(1):79–111.
- Stewart, R. T., J. L. Innis, O. B. Slee, G. J. Nelson, and A. E. Wright  
 1988. A Relation Between Radio Luminosity and Rotation for Late-Type Stars. *AJ*, 96:371.

- Suárez Mascareño, A., R. Rebolo, and J. I. González Hernández  
2016. Magnetic cycles and rotation periods of late-type stars from photometric time series. *A&A*, 595:A12.
- Suárez Mascareño, A., R. Rebolo, J. I. González Hernández, B. Toledo-Padrón, M. Perger, I. Ribas, L. Af-fer, G. Micela, M. Damasso, J. Maldonado, E. González-Alvarez, G. Leto, I. Pagano, G. Scandariato, A. Sozzetti, A. F. Lanza, L. Malavolta, R. Claudi, R. Cosentino, S. Desidera, P. Giacobbe, A. Maggio, M. Rainer, M. Esposito, S. Benatti, M. Pedani, J. C. Morales, E. Herrero, M. Lafarga, A. Rosich, and M. Pinamonti  
2018. HADES RV programme with HARPS-N at TNG. VII. Rotation and activity of M-dwarfs from time-series high-resolution spectroscopy of chromospheric indicators. *A&A*, 612:A89.
- Suematsu, Y., K. Shibata, T. Neshikawa, and R. Kitai  
1982. Numerical Hydrodynamics of the Jet Phenomena in the Solar Atmosphere - Part One - Spicules. *Sol. Phys.*, 75(1-2):99–118.
- Suzuki, T. K.  
2004. Coronal heating and acceleration of the high/low-speed solar wind by fast/slow MHD shock trains. *MNRAS*, 349(46):1227–1239.
- Suzuki, T. K.  
2007. Structured Red Giant Winds with Magnetized Hot Bubbles and the Corona/Cool Wind Dividing Line. *ApJ*, 659(2):1592–1610.
- Suzuki, T. K.  
2018. Stellar winds and coronae of low-mass Population II/III stars. *PASJ*, 70(3):34.
- Suzuki, T. K., S. Imada, R. Kataoka, Y. Kato, T. Matsumoto, H. Miyahara, and S. Tsuneta  
2013. Saturation of Stellar Winds from Young Suns. *PASJ*, 65:98.
- Suzuki, T. K. and S.-i. Inutsuka  
2005. Making the Corona and the Fast Solar Wind: A Self-consistent Simulation for the Low-Frequency Alfvén Waves from the Photosphere to 0.3 AU. *ApJL*, 632(1):L49–L52.
- Suzuki, T. K. and S.-I. Inutsuka  
2006. Solar winds driven by nonlinear low-frequency Alfvén waves from the photosphere: Parametric study for fast/slow winds and disappearance of solar winds. *Journal of Geophysical Research (Space Physics)*, 111(A6):A06101.
- Tajima, T. and K. Shibata  
1997. *Plasma astrophysics*. Reading, Massachusetts: Addison-Wesley.
- Tanaka, Y. A., T. K. Suzuki, and S.-i. Inutsuka  
2014. Atmospheric Escape by Magnetically Driven Wind from Gaseous Planets. *ApJ*, 792(1):18.
- Tanaka, Y. A., T. K. Suzuki, and S.-i. Inutsuka  
2015. Atmospheric Escape by Magnetically Driven Wind from Gaseous Planets. II. Effects of Magnetic Diffusion. *ApJ*, 809(2):125.
- Tarter, J. C., P. R. Backus, R. L. Mancinelli, J. M. Aurnou, D. E. Backman, G. S. Basri, A. P. Boss, A. Clarke, D. Deming, L. R. Doyle, E. D. Feigelson, F. Freund, D. H. Grinspoon, R. M. Haberle, I. Hauck, Steven A., M. J. Heath, T. J. Henry, J. L. Hollingsworth, M. M. Joshi, S. Kilston, M. C. Liu, E. Meikle, I. N. Reid,

- L. J. Rothschild, J. Scalo, A. Segura, C. M. Tang, J. M. Tiedje, M. C. Turnbull, L. M. Walkowicz, A. L. Weber, and R. E. Young  
 2007. A Reappraisal of The Habitability of Planets around M Dwarf Stars. *Astrobiology*, 7(1):30–65.
- Terasawa, T., M. Hoshino, J. I. Sakai, and T. Hada  
 1986. Decay instability of finite-amplitude circularly polarized Alfvén waves: A numerical simulation of stimulated Brillouin scattering. *JGR*, 91(A4):4171–4187.
- Tian, F.  
 2009. Thermal Escape from Super Earth Atmospheres in the Habitable Zones of M Stars. *ApJ*, 703(1):905–909.
- Tian, F. and S. Ida  
 2015. Water contents of Earth-mass planets around M dwarfs. *Nature Geoscience*, 8(3):177–180.
- Tsiropoula, G., K. Tziotziou, I. Kontogiannis, M. S. Madjarska, J. G. Doyle, and Y. Suematsu  
 2012. Solar Fine-Scale Structures. I. Spicules and Other Small-Scale, Jet-Like Events at the Chromospheric Level: Observations and Physical Parameters. *SSRv*, 169(1-4):181–244.
- Ulmschneider, P.  
 1979. Stellar Chromospheres. *SSRv*, 24(1):71–100.
- Ulmschneider, P., D. Fawzy, Z. E. Musielak, and K. Stępień  
 2001a. Wave Heating and Range of Stellar Activity in Late-Type Dwarfs. *ApJL*, 559(2):L167–L170.
- Ulmschneider, P., Z. E. Musielak, and D. E. Fawzy  
 2001b. Magnetic wave energy fluxes for late-type stars. I. Longitudinal tube waves. *A&A*, 374:662–674.
- Vaiana, G. S., J. P. Cassinelli, G. Fabbiano, R. Giacconi, L. Golub, P. Gorenstein, B. M. Haisch, J. Harnden, F. R., H. M. Johnson, J. L. Linsky, C. W. Maxson, R. Mewe, R. Rosner, F. Seward, K. Topka, and C. Zwaan  
 1981. Results from an extensive Einstein stellar survey. *ApJ*, 245:163–182.
- Vaiana, G. S., A. S. Krieger, A. F. Timothy, and M. Zombeck  
 1976. ATM Observations, X-Ray Results. *Ap&SS*, 39(1):75–101.
- Valenti, J. A. and D. A. Fischer  
 2005. Spectroscopic Properties of Cool Stars (SPOCS). I. 1040 F, G, and K Dwarfs from Keck, Lick, and AAT Planet Search Programs. *ApJS*, 159(1):141–166.
- van der Holst, B., I. V. Sokolov, X. Meng, M. Jin, I. Manchester, W. B., G. Tóth, and T. I. Gombosi  
 2014. Alfvén Wave Solar Model (AWSOM): Coronal Heating. *ApJ*, 782(2):81.
- Vaughan, A. H., S. L. Baliunas, F. Middelkoop, L. W. Hartmann, D. Mihalas, R. W. Noyes, and G. W. Preston  
 1981. Stellar rotation in lower main-sequence stars measured from time variations in H and K emission-line fluxes. I. Initial results. *ApJ*, 250:276–283.
- Velli, M., R. Grappin, and A. Mangeney  
 1989. Turbulent cascade of incompressible unidirectional Alfvén waves in the interplanetary medium. *PhRvL*, 63(17):1807–1810.

- Vernazza, J. E., E. H. Avrett, and R. Loeser  
1981. Structure of the solar chromosphere. III. Models of the EUV brightness components of the quiet sun. *ApJS*, 45:635–725.
- Vidotto, A. A. and V. Bourrier  
2017. Exoplanets as probes of the winds of host stars: the case of the M dwarf GJ 436. *MNRAS*, 470(4):4026–4033.
- Vidotto, A. A., M. Jardine, J. Morin, J. F. Donati, M. Opher, and T. I. Gombosi  
2014. M-dwarf stellar winds: the effects of realistic magnetic geometry on rotational evolution and planets. *MNRAS*, 438(2):1162–1175.
- Vidotto, A. A., M. Jardine, M. Opher, J. F. Donati, and T. I. Gombosi  
2011. Powerful winds from low-mass stars: V374 Peg. *MNRAS*, 412(1):351–362.
- Wang, Y. and T. Yokoyama  
2020. Simulation of Alfvén Wave Propagation in the Magnetic Chromosphere with Radiative Loss: Effects of Nonlinear Mode Coupling on Chromospheric Heating. *ApJ*, 891(2):110.
- Washinoue, H. and T. K. Suzuki  
2019. Coronae of Zero/Low-metal, Low-mass Stars. *ApJ*, 885(2):164.
- Weber, E. J. and J. Davis, Leverett  
1967. The Angular Momentum of the Solar Wind. *ApJ*, 148:217–227.
- West, A. A., K. L. Weisenburger, J. Irwin, Z. K. Berta-Thompson, D. Charbonneau, J. Dittmann, and J. S. Pineda  
2015. An Activity-Rotation Relationship and Kinematic Analysis of Nearby Mid-to-Late-Type M Dwarfs. *ApJ*, 812(1):3.
- Wiegmann, T. and S. K. Solanki  
2004. Similarities and Differences between Coronal Holes and the Quiet Sun: Are Loop Statistics the Key? *Sol. Phys.*, 225(2):227–247.
- Williams, P. K. G., B. A. Cook, and E. Berger  
2014. Trends in Ultracool Dwarf Magnetism. I. X-Ray Suppression and Radio Enhancement. *ApJ*, 785(1):9.
- Wilson, O. C.  
1966a. Stellar Chromospheres. *Science*, 151(3717):1487–1498.
- Wilson, O. C.  
1966b. Stellar Convection Zones, Chromospheres, and Rotation. *ApJ*, 144:695.
- Wilson, O. C.  
1978. Chromospheric variations in main-sequence stars. *ApJ*, 226:379–396.
- Withbroe, G. L. and R. W. Noyes  
1977. Mass and energy flow in the solar chromosphere and corona. *ARA&A*, 15:363–387.
- Wolff, S. C., A. M. Boesgaard, and T. Simon  
1986. Activity in F Stars. *ApJ*, 310:360.

- Wood, B. E., J. L. Linsky, H.-R. Müller, and G. P. Zank  
 2001. Observational Estimates for the Mass-Loss Rates of  $\alpha$  Centauri and Proxima Centauri Using Hubble Space Telescope Ly $\alpha$  Spectra. *ApJL*, 547(1):L49–L52.
- Wood, B. E., H.-R. Müller, G. P. Zank, and J. L. Linsky  
 2002. Measured Mass-Loss Rates of Solar-like Stars as a Function of Age and Activity. *ApJ*, 574(1):412–425.
- Wood, B. E., H. R. Müller, G. P. Zank, J. L. Linsky, and S. Redfield  
 2005a. New Mass-Loss Measurements from Astrospheric Ly $\alpha$  Absorption. *ApJL*, 628(2):L143–L146.
- Wood, B. E., S. Redfield, J. L. Linsky, H.-R. Müller, and G. P. Zank  
 2005b. Stellar Ly $\alpha$  Emission Lines in the Hubble Space Telescope Archive: Intrinsic Line Fluxes and Absorption from the Heliosphere and Astrospheres. *ApJS*, 159(1):118–140.
- Woolley, R. D. V. R. and C. W. Allen  
 1948. The Coronal Emission Spectrum. *MNRAS*, 108:292.
- Wright, N. J. and J. J. Drake  
 2016. Solar-type dynamo behaviour in fully convective stars without a tachocline. *Nature*, 535(7613):526–528.
- Wright, N. J., J. J. Drake, E. E. Mamajek, and G. W. Henry  
 2011. The Stellar-activity-Rotation Relationship and the Evolution of Stellar Dynamos. *ApJ*, 743(1):48.
- Wright, N. J., E. R. Newton, P. K. G. Williams, J. J. Drake, and R. K. Yadav  
 2018. The stellar rotation-activity relationship in fully convective M dwarfs. *MNRAS*, 479(2):2351–2360.
- Yasuda, Y., T. K. Suzuki, and T. Kozasa  
 2019. Alfvén Wave-driven Wind from RGB and AGB Stars. *ApJ*, 879(2):77.
- Youngblood, A., K. France, R. O. P. Loyd, A. Brown, J. P. Mason, P. C. Schneider, M. A. Tilley, Z. K. Berta-Thompson, A. Buccino, C. S. Froning, S. L. Hawley, J. Linsky, P. J. D. Mauas, S. Redfield, A. Kowalski, Y. Miguel, E. R. Newton, S. Rugheimer, A. Segura, A. Roberge, and M. Veytes  
 2017. The MUSCLES Treasury Survey. IV. Scaling Relations for Ultraviolet, Ca II K, and Energetic Particle Fluxes from M Dwarfs. *ApJ*, 843(1):31.
- Zhang, Y. Z., K. Shibata, J. X. Wang, X. J. Mao, T. Matsumoto, Y. Liu, and J. T. Su  
 2012. Revision of Solar Spicule Classification. *ApJ*, 750(1):16.



## Chapter 2

# Energy Transfer by Nonlinear Alfvén Waves in the Solar Chromosphere, and Its Effect on Spicule Dynamics, Coronal Heating, and Solar Wind Acceleration

Alfvén waves are responsible for the transfer of magnetic energy in the magnetized plasma. They are involved in heating solar atmosphere and driving solar wind through various nonlinear processes. Because the magnetic field configurations directly affect the nonlinearity of Alfvén waves, it is important to investigate how they relate to the solar atmosphere and wind structure through the nonlinear propagation of Alfvén waves. In this study, we carried out one-dimensional magnetohydrodynamic simulations to realize the above relation. The results show that when the nonlinearity of Alfvén waves in the chromosphere exceeds a critical value, the dynamics of the solar chromosphere (e.g., spicule) and the mass-loss rate of solar wind tend to be independent of the energy input from the photosphere. In a situation where the Alfvén waves are highly nonlinear, the strong shear torsional flow generated in the chromosphere “fractures” the magnetic flux tube. This corresponds to the formation of chromospheric intermediate shocks, which limit the transmission of the Poynting flux into the corona by Alfvén waves and also inhibits the propagation of chromospheric slow shock.

### 2.1 Introduction

The solar atmosphere consists of magnetized plasma with various thermal properties. A 1 MK corona is characterized by tenuous, fully ionized, and low- $\beta$  plasma. It is the envelope of a cool ( $\sim 10^4$  K), dense, and partially ionized chromosphere. Coronal and chromospheric heating problems arise from the question regarding the manner of how energy is steadily supplied and deposited to maintain such a thermal structure of solar atmosphere. These problems are directly related to the physical mechanism for solar wind acceleration.

The nonlinear propagation of Alfvén waves is one of the promising physical mechanisms to solve this

problem. That is because this incompressible wave is responsible for the transfer of magnetic energy in the magnetized plasma and is involved in the energy conversion to the kinetic or thermal energy of the background media through the nonlinear processes. Numerous theoretical studies have developed the scenarios relating Alfvén waves to atmospheric heating (Alfvén, 1947; Osterbrock, 1961; Coleman, 1968; Heyvaerts and Priest, 1983), solar wind acceleration (Belcher and MacGregor, 1976; Heinemann and Olbert, 1980), and spicule dynamics (Hollweg et al., 1982; Kudoh and Shibata, 1999). These ideas have been examined using spaceborne observations that confirmed the ubiquitous existence of Alfvén waves from the chromosphere (De Pontieu et al., 2007; Okamoto and De Pontieu, 2011), corona (Cirtain et al., 2007; Banerjee et al., 2009; Hahn and Savin, 2013) to interplanetary space (Belcher and Davis, 1971; Bavassano et al., 1982; Bavassano et al., 2001).

Recent magnetohydrodynamics (MHD) simulations enable a more seamless description of the relationship between Alfvén wave propagation and the dynamics of the solar atmosphere and wind. Because of the inhomogeneous, time-dependent, and stratified solar atmosphere, Alfvén wave propagation can be affected by various physical mechanisms in each layer of the solar atmosphere. Matsumoto and Suzuki (2012) and Matsumoto and Suzuki (2014) carried out a 2.5 dimensional simulation and showed the self-consistent transition of heating mechanisms from shock heating to incompressible processes across the transition layer. On the basis of their 3D simulation, Shoda et al. (2019) confirmed that the density fluctuation caused by the parametric decay instability (Goldstein, 1978; Derby, 1978; Terasawa et al., 1986) is essential in exciting Alfvén wave turbulence in the solar wind.

Aside from the above-mentioned multidimensional models, one-dimensional (1D) simulations are still helpful, particularly in investigating the diversity or universality of solar and stellar atmospheres and wind. They have contributed to understanding how Alfvén waves are involved with spicules (Hollweg et al., 1982; Matsumoto and Shibata, 2010), the solar and stellar wind (Suzuki and Inutsuka, 2005; Suzuki, 2007; Suzuki, 2018; Yasuda et al., 2019), and the coronal loop (Moriyasu et al., 2004; Antolin and Shibata, 2010; Washinoue and Suzuki, 2019). Despite these extensive works, there have been few studies focused on the chromospheric magnetic field environment in terms of their influence on the solar atmosphere and wind. The magnetic field in the solar atmosphere is highly inhomogeneous and variable with time. Thus, it directly affects the profile of the Alfvén speed with respect to height, which determines the reflection efficiency of Alfvén waves (An et al., 1990; Velli, 1993) and induces Alfvén resonance (Hollweg, 1978; Matsumoto and Shibata, 2010). The expanding magnetic flux tube in the lower atmosphere, additionally, is related to the rapid evolution of the Alfvén wave amplitude. That leads to the dissipation of Alfvén waves through direct steepening (Hollweg et al., 1982) or nonlinear mode coupling (Hollweg, 1992; Kudoh and Shibata, 1999; Wang and Yokoyama, 2020). Coronal heating and solar wind acceleration are sustained with a slight transmission of Alfvén waves from the chromosphere. Therefore, it is worthwhile to examine how robustly Alfvén waves can transport magnetic energy across the chromosphere even in different magnetic field configurations in the lower atmosphere.

In this study, we performed time-dependent 1D MHD simulations similar to Kudoh and Shibata (1999) or Suzuki and Inutsuka (2005). Unlike them, we pay particular attention to the dependence of the spicule dynamics, coronal heating, and solar wind acceleration on the magnetic field configuration in the lower atmosphere.

## 2.2 Numerical Setting

### 2.2.1 Basic Equations

We used 1D magnetohydrodynamic equations based on the axial symmetry assumption of the magnetic flux tube. The surface of the axisymmetric flux tube is defined by the poloidal and toroidal axes, which are noted in this study by  $x$  and  $\phi$ . The basic equations in cgs units are written as follows:

The mass conservation law is presented by

$$\frac{\partial \rho}{\partial t} + \frac{1}{A} \frac{\partial}{\partial x} (\rho v_x A) = 0, \quad (2.1)$$

where  $\rho$ ,  $v_x$  and  $A$  are the mass density, poloidal component of velocity, and cross section of the flux tube, respectively.

The energy conservation law is presented by

$$\begin{aligned} & \frac{\partial}{\partial t} \left( \frac{p}{\gamma - 1} + \frac{1}{2} \rho v^2 + \frac{B^2}{8\pi} \right) \\ & + \frac{1}{A} \frac{\partial}{\partial x} \left[ A \left\{ \left( \frac{\gamma p}{\gamma - 1} + \frac{\rho v^2}{2} + \frac{B_\phi^2}{4\pi} \right) v_x - \frac{B_x}{4\pi} (B_\phi v_\phi) \right\} \right] \\ & = \rho v_x \frac{\partial}{\partial x} \left( \frac{GM_\odot}{r} \right) - \frac{1}{A} \frac{\partial}{\partial x} (AF_c) - Q_{\text{rad}}, \end{aligned} \quad (2.2)$$

where  $p$ ,  $B_x$ ,  $B_\phi$ ,  $v_\phi$  and  $\gamma$  are the gas pressure, poloidal and toroidal components of magnetic field, toroidal component of velocity, and the specific heat, ratio which is set to 5/3, respectively.  $v^2 = v_x^2 + v_\phi^2$  and  $B^2 = B_x^2 + B_\phi^2$ .  $G$  and  $M_\odot$  are gravitational constant and the solar mass.  $r$  is the distance from the Sun center.  $F_c$  and  $Q_{\text{rad}}$  represent the heat conduction flux and radiative cooling term, respectively, as described in Section 2.2.3.

The poloidal component of the equation of motion is presented by:

$$\begin{aligned} & \frac{\partial(\rho v_x)}{\partial t} + \frac{\partial p}{\partial x} + \frac{1}{A} \frac{\partial}{\partial x} \left\{ \left( \rho v_x^2 + \frac{B_\phi^2}{8\pi} \right) A \right\} \\ & - \rho v_\phi^2 \frac{\partial \ln \sqrt{A}}{\partial x} - \rho \frac{\partial}{\partial x} \left( \frac{GM_\odot}{r} \right) = 0. \end{aligned} \quad (2.3)$$

The toroidal component of the equation of motion is presented by

$$\frac{\partial(\rho v_\phi)}{\partial t} + \frac{1}{A\sqrt{A}} \frac{\partial}{\partial x} \left\{ A\sqrt{A} \left( \rho v_x v_\phi - \frac{B_x B_\phi}{4\pi} \right) \right\} = 0. \quad (2.4)$$

The toroidal component of the induction equation is presented by

$$\frac{\partial B_\phi}{\partial t} + \frac{1}{\sqrt{A}} \frac{\partial}{\partial x} \left( \sqrt{A} (v_x B_\phi - v_\phi B_x) \right) = 0. \quad (2.5)$$

The poloidal magnetic flux conservation is presented by

$$B_x A = \text{const}. \quad (2.6)$$

Finally, we note that the poloidal axis  $x$  is not always parallel to the radial axis  $r$ . They are related to each other as follows:

$$\frac{dx}{dr} = \sqrt{1 + \left( \frac{d\sqrt{A}}{dr} \right)^2}. \quad (2.7)$$

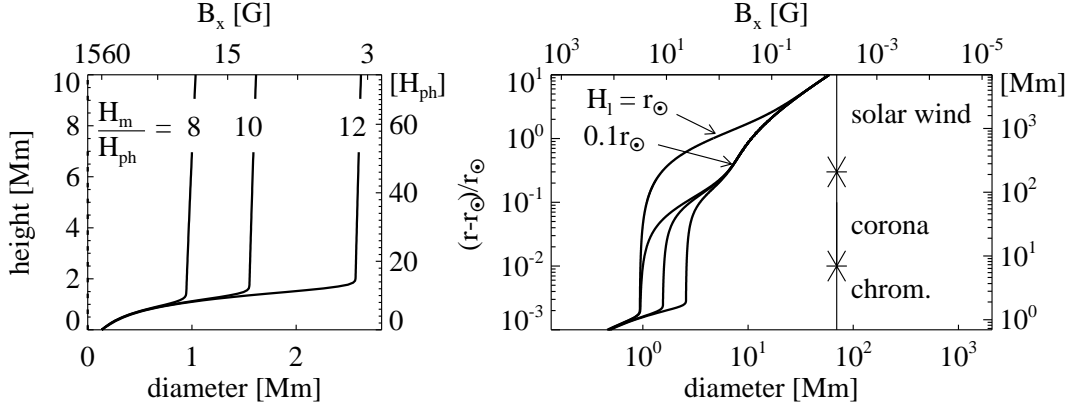


Figure 2.1: Poloidal magnetic field configurations characterized with the free parameters ( $H_m$ ,  $H_l$ ), where  $H_m$ ,  $H_l$  and  $H_{\text{ph}}$  are the merging height, loop height, and the pressure scale height on the photosphere, respectively. The left and right panels show it in the lower and outer atmosphere.

### 2.2.2 Magnetic Flux Tube Model

The assumption of the background magnetic field is described here in detail. The cross section of the flux tube  $A$  is related to  $r$  through the filling factor  $f$  as  $A(r) = 4\pi r^2 f(r)$ .  $f$  determines the geometry of the flux tube. We consider the axisymmetric magnetic flux tube from the photosphere to interplanetary space. The outer boundary of our simulation is set to 0.5 au. In the lower atmosphere, the magnetic flux tube expands exponentially such that the magnetic pressure inside the flux tube balances out with the ambient plasma gas pressure, which decreases with the scale height  $H_{\text{ph}} = R_g T_{\text{eff}} / (\mu_{\text{ph}} g_{\odot})$ . Here,  $R_g = 8.31 \times 10^7 \text{ erg K}^{-1} \text{ mol}^{-1}$  is the gas constant,  $T_{\text{eff}} = 5770 \text{ K}$ ,  $\mu_{\text{ph}} = 1.3$  is the mean molecular weight on the photosphere, and  $g_{\odot}$  is the gravitational acceleration on the solar surface. The filling factor  $f$  in this layer is expected to be  $f_{\text{atm}}(r) = f_{\text{ph}} \exp\{r_{\odot} / (2H_{\text{ph}})(1 - r_{\odot}/r)\}$ , where  $f_{\text{ph}}$  is the coverage of the open magnetic flux tube on the photosphere. By using  $f_{\text{atm}}$ ,  $B_x = r_{\odot}^2 f_{\text{ph}} B_{\text{ph}} / (r^2 f_{\text{atm}})$  satisfies the condition that  $B_x^2 / (8\pi) = p_{\text{atm}}$ , where  $p_{\text{atm}}$  is the solution of the hydrostatic equilibrium. In the lower atmosphere where  $r = r_{\odot} + h$  ( $h \ll r_{\odot}$ ), we obtain  $f_{\text{atm}}(h) = f_{\text{ph}} e^{h/(2H_{\text{ph}})}$ . This exponential expansion of flux tube is assumed to stop at some height where it merges with the neighboring flux tube. Above this height (i.e., the merging height  $H_m$ ), the magnetic pressure dominates the gas pressure and the flux tube extends vertically. The poloidal magnetic field strength in this layer is assumed to be almost constant around  $\bar{B} = B_{\text{ph}} f_{\text{ph}} / f_{\text{atm}}(H_m) = B_{\text{ph}} e^{-H_m/(2H_{\text{ph}})}$  through the upper chromosphere and coronal base. Thus,  $\bar{B} = B_{\text{ph}} e^{-H_m/(2H_{\text{ph}})}$  roughly represents the area-averaged magnetic field strength in the coronal hole from which the solar wind emanates. It should be noted that various flux tube models in the lower atmosphere have been considered, for example, by [Hasan et al. \(2003, 2005\)](#) and [Cranmer and van Ballegooijen \(2005\)](#). The different magnetic field geometries would lead to different results. Their significance should be tested in future studies as long as we rely on the 1D simulation.

The flux tube is assumed to expand superradially again in the extended corona such that the interplanetary space is filled with the open flux tube. We characterize this expansion with the coronal loop height  $H_l$ . The functional form of the filling factor in this layer  $f_{\text{wind}}(r)$  is suggested by [Kopp and Holzer \(1976\)](#). Based on these considerations, the profile of the filling factor  $f(r)$  is determined as follows:

$$f_{\text{atm}}(r) = f_m \tanh \left[ \frac{f_{\text{ph}}}{f_m} \exp \left\{ \frac{r_{\odot}}{2H_{\text{ph}}} \left( 1 - \frac{r_{\odot}}{r} \right) \right\} \right], \quad (2.8)$$

where  $f_m = f_{\text{ph}} e^{H_m/(2H_{\text{ph}})}$

$$f_{\text{wind}}(r) = \frac{e^{(r-r_{\odot}-H_l)/\sigma_l} + f_m - (1-f_m)e^{-(H_l/\sigma_l)}}{e^{(r-r_{\odot}-H_l)/\sigma_l} + 1} \quad (2.9)$$

$$\hat{f}(r) = f_{\text{atm}}(r) + \frac{1}{2} \left( \max[f_{\text{wind}}(r), f_m] - f_{\text{atm}}(r) \right) \times \left\{ 1 + \tanh \left( \frac{r - r_{\odot} - H_l}{H_l} \right) \right\} \quad (2.10)$$

$$f(r) = f_{\text{ph}} + (1 - f_{\text{ph}}) \frac{\hat{f}(r) - \hat{f}(r_{\odot})}{1 - \hat{f}(r_{\odot})}. \quad (2.11)$$

The key parameters of  $f(r)$  are  $f_{\text{ph}}$ ,  $H_m$ , and  $H_l$ .  $\sigma_l$  in Equation (2.9) is set to  $H_l$ . The manner by which the properties of solar and stellar wind depend on  $f_{\text{ph}}$  has already been well investigated in previous studies (Suzuki, 2006; Suzuki et al., 2013). Thereafter, we use the fixed value of 1/1600 for  $f_{\text{ph}}$  by referring to Suzuki et al. (2013). Note that, when  $f_{\text{ph}} = 1/1600$ , the magnetic field strength at  $r = 1$  au is 2.1nT, which is within the typical observed value (Wang et al., 2000). The configuration of the magnetic flux tube with  $f_{\text{ph}} = 1/1600$  is depicted in Figure 2.1. As shown in this figure, the merging height  $H_m$  is the parameter defining the magnetic field strength  $\bar{B}$  from the chromosphere up to the lower corona. The higher merging height corresponds to a weaker magnetic field  $\bar{B}$ , and, in particular,  $H_m/H_{\text{ph}} = 8, 12$  are used in this study. It should be noted that  $H_m/H_{\text{ph}} = 8, 10, 12$  correspond to  $\bar{B} = 29, 11, 4$  G, respectively. These magnetic field strengths are comparable to the typical value for the area-averaged magnetic field strength in the coronal hole (3–36 G near the solar activity maximum and 1–7 G close to the minimum, according to Harvey et al. (1982); see also review by Wiegmann and Solanki (2004)). By adopting a higher coronal loop height  $H_l$ , the magnetic field strength in the upper corona can be larger (Figure 2.1), but  $H_l/r_{\odot}$  is fixed at 0.1.

### 2.2.3 Heat Conduction and Radiative Cooling

The equation of state is  $p = \rho R_g T / [\mu_{\text{ph}}(1 - \chi(T)/2)]$ , where  $\chi(T)$  is the ionization degree as a function of temperature, which is calculated by referring to Carlsson and Leenaarts (2012). The radiative cooling  $Q_{\text{rad}}$  is given by the empirical formulae, which is composed of three distinct terms, i.e., the photospheric radiation  $Q_{\text{ph}}$ , chromospheric radiation  $Q_{\text{ch}}$ , and coronal radiation  $Q_{\text{cr}}$ :

$$Q_{\text{rad}} = (1 - \xi_1)(1 - \xi_2)Q_{\text{ph}} + \xi_1(1 - \xi_2)Q_{\text{ch}} + \xi_2Q_{\text{cr}}, \quad (2.12)$$

where  $\xi_1$  and  $\xi_2$  are assumed to be as follows:

$$\xi_1 = \frac{1}{2} \left[ 1 + \tanh \left( \frac{r - r_{\odot}}{H_{\text{ph}}} - 3 \right) \right], \quad (2.13)$$

$$\xi_2 = \exp \left( -4 \times 10^{-20} \int_{\infty}^r n_{\text{HI}} dr' \right), \quad (2.14)$$

$n_{\text{HI}} = (1 - \chi(T))\rho/m_p$  is the neutral hydrogen density Each term in Equation (2.12) is defined as follows:

$$Q_{\text{ph}} = 4\rho\kappa_R\sigma_{\text{SB}}T^4 \max \left( \frac{T^4}{T_{\text{ref}}^4} - 1, -e^{-(r-r_{\odot})^2/H_{\text{ph}}^2} \right), \quad (2.15)$$

$$\text{where } T_{\text{ref}} = T_{\text{eff}} \left( \frac{3}{4} \rho \kappa_R H_{\text{ph}} + \frac{1}{2} \right)^{1/4}, \quad (2.16)$$

$$Q_{\text{ch}} = 4.9 \times 10^9 \text{ [erg g}^{-1} \text{ s}^{-1}] \rho, \quad Q_{\text{cr}} = \chi(T) (\rho/m_p)^2 \Lambda(T). \quad (2.17)$$

$\kappa_R = 0.2 \text{ cm}^2 \text{ g}^{-1}$  pertains to the Rosseland opacity on the photosphere.  $\sigma_{SB}$  is the Stefan–Boltzmann constant.  $Q_{\text{ch}}$  and  $Q_{\text{cr}}$  are the same functions used in [Hori et al. \(1997\)](#), which are always positive.  $\Lambda(T)$  in Equation () is the radiative loss function for the optically thin plasma.  $Q_{\text{ph}}$  in Equation 2.15 is allowed to be negative where  $e^{-(r-r_\odot)^2/H_{\text{ph}}^2} \sim 1$ , which represents the radiative heating.

The heat conductive flux is presented by

$$F_c = -\kappa(T) \frac{\partial T}{\partial x} \quad (2.18)$$

where  $\kappa(T)$  is the heat conductivity as a function of the temperature. That is composed of the collisional and collisionless terms:

$$\kappa(T) = q\kappa_{\text{coll}} + (1 - q)\kappa_{\text{sat}} \quad (2.19)$$

where  $q = \max(0, \min(1, 1 - 0.5\kappa_{\text{coll}}/\kappa_{\text{sat}}))$ .  $\kappa_{\text{coll}}(T)$  is adopted from [Nagai \(1980\)](#), which agrees with the Spitzer–Härm heat conductivity ([Spitzer and Härm, 1953](#))  $\kappa_0 T^{5/2}$  ( $\kappa_0 = 10^{-6}$  in CGS unit) when  $T > 10^6$  K.  $\kappa_{\text{sat}}$  is given by

$$\kappa_{\text{sat}} = \frac{3}{2} p v_{e,\text{thr}} \frac{r}{T} \quad (2.20)$$

where  $v_{e,\text{thr}}$  is the thermal speed of the electron.  $\kappa_{\text{sat}}$  represents the saturation of heat flux caused by the collisionless effect ([Parker, 1964](#); [Bale et al., 2013](#)). The above expression of  $\kappa_{\text{sat}}$  means that the transition of heat conductivity from  $\kappa_{\text{coll}}$  to  $\kappa_{\text{sat}}$  occurs around  $r \sim \lambda_{e,\text{mfp}}$  ( $\lambda_{e,\text{mfp}}$  is the electron mean free path) and that the heat flux is limited to  $\frac{3}{2} \alpha p v_{e,\text{thr}}$  in the distance where  $T \sim r^{-\alpha}$  ( $\alpha = 0.2 - 0.4$  for winds faster than  $500 \text{ km s}^{-1}$ ; [Marsch et al. \(1989\)](#)). Based on the foregoing heat conductivity, heat conduction is solved by the super-time-stepping method ([Meyer et al., 2012](#); [Meyer et al., 2014](#)).

## 2.2.4 Initial and Boundary Condition

We set the static atmosphere with a temperature of  $10^4$  K as the initial state. The temperature on the bottom boundary is promptly cooled down to  $T_{\text{eff}} = 5770$  K after the initiation of the simulation. The mass density and poloidal magnetic field strength on the photosphere are  $\rho_{\text{ph}} = 2.5 \times 10^{-7} \text{ g cm}^{-3}$  and  $B_{\text{ph}} = 1560$  G, respectively. To excite the outwardly propagating Alfvén wave, the toroidal velocity  $v_\phi$  on the bottom boundary is oscillated artificially, which represents convective motion on the solar photosphere. We consider it as a frequency-dependent fluctuation with the following power spectrum.

$$v_{\text{conv}}^2 \propto \int_{\nu_{\text{min}}}^{\nu_{\text{max}}} \nu^{-1} d\nu, \quad (2.21)$$

where  $v_{\text{conv}}$  is the free parameter corresponding to the amplitude of the convective velocity.  $\nu_{\text{min}}^{-1}$  and  $\nu_{\text{max}}^{-1}$  are 30 minutes and 20 s, respectively. The phase offsets of fluctuation are randomly assigned. The amplitude of fluctuation  $v_{\text{conv}}$  is the subject of survey in this study, e.g.,  $v_{\text{conv}}/c_{\text{sph}} = 0.07, 0.14, 0.21, 0.42, 0.85$

( $c_{\text{sph}} = \sqrt{\gamma R_g T_{\text{eff}} / \mu_{\text{ph}}} = 7.8 \text{ km s}^{-1}$  is the adiabatic sound speed on the photosphere). This parameter range includes the typical velocity of horizontal convective motion,  $1.1 \text{ km s}^{-1}$  (Matsumoto and Kitai, 2010).

To excite the purely outward Alfvén waves on the bottom boundary, the toroidal magnetic field  $B_\phi$  is determined by  $B_\phi = -\sqrt{4\pi\rho}v_\phi$ . This means that the Elsässer variables (i.e.,  $z_{\text{out}} = v_\phi - B_\phi/\sqrt{4\pi\rho}$ , and  $z_{\text{in}} = v_\phi + B_\phi/\sqrt{4\pi\rho}$ ) on the bottom boundary satisfy the conditions, i.e.,  $z_{\text{out}} = 2v_\phi$  and  $z_{\text{in}} = 0$ . The longitudinal velocity component  $v_x$  on the bottom boundary is also given as the fluctuation with the amplitude  $v_{\text{conv}}$ , the power spectrum similar to that of the foregoing, and the randomly assigned phase offsets. We performed a few simulations with  $v_x = 0$  on the bottom boundary. We were able to confirm that  $v_x \neq 0$  on the photosphere does not have any influence on the solar wind structure, but the spicule height can depend on it.

The upper boundary is treated as the free boundary. A total of 19,200 grids are placed nonuniformly in between. The numerical scheme is based on the HLLD Riemann solver (Miyoshi and Kusano, 2005) with the second-order MUSCL interpolation and the third-order TVD Runge—Kutta method (Shu and Osher, 1988).

## 2.3 Results

### 2.3.1 Solar Wind Profiles

After several tens of hours, the solar wind in the simulation box reaches the quasi-steady state with numerous wave signatures (Figure 2.2). Figure 2.3 shows the simulation results, including the snapshots of solar wind velocity, mass density, temperature profiles, and temporally averaged profiles of Alfvén wave amplitude and Alfvén speed in the solar wind. The black and red lines in each figure correspond to the results in the cases of  $\bar{B} = 29$  and 4 G, respectively.

The top panel of Figure 2.3 shows that the solar wind in the  $\bar{B} = 4$  G case is found to be faster than that in  $\bar{B} = 29$  G case. The Alfvén speed at the coronal base is much higher in the  $\bar{B} = 29$  G case than in  $\bar{B} = 4$  G. In the outer space above the coronal loop height, where the magnetic field strengths in both cases are the same, the Alfvén speed in  $\bar{B} = 4$  G case is larger than in  $\bar{B} = 29$  G, clearly indicating denser wind in the  $\bar{B} = 29$  G case. With regard to the higher Alfvén speed at the coronal base in  $\bar{B} = 29$  G, the Alfvén speed steeply declines above the coronal loop height due to the largely expanding magnetic flux tube. This induces the strong interference between the outward and inward Alfvén waves, resulting in the humps of the Alfvén wave amplitude profiles below  $0.1r_\odot$ .

The most significant discrepancy between the solar winds in different merging heights is found in the wind’s mass-loss rate. Figure 2.4 shows the mass-loss rates as a function of the energy input from the photosphere ( $F_{A0} = \rho_{\text{ph}}v_{\text{conv}}^2V_{\text{Aph}}$ ). The filled and open circles show the results for  $\bar{B} = 29$  and 4 G, respectively. While the wind’s mass-loss rate monotonically increases with a larger energy input from the photosphere in the case of  $\bar{B} = 29$  G, that in  $\bar{B} = 4$  G is almost independent of the energy input. The mass-loss rate in  $\bar{B} = 4$  G is limited to  $\sim 10^{-15} M_\odot \text{ yr}^{-1}$  even in the largest energy input case of  $v_{\text{conv}}/c_{\text{sph}} = 0.42$ , which is two orders of magnitude smaller than that in the  $\bar{B} = 29$  G case.

### 2.3.2 Spicule Dynamics

Figure 2.5 shows the time-slice diagrams of the mass density in the lower atmosphere. The top of the chromosphere ( $\rho/\rho_{\text{ph}} \sim 10^{-7}$ ) shows the upward and downward motions representing the spicule dynamics. Figure 2.5(a) and (b) are the results in the cases of  $\bar{B} = 29$  G for  $v_{\text{conv}}/c_{\text{sph}} = 0.21$  and 0.42, respectively.

The height of the spicule becomes taller with a larger  $v_{\text{conv}}/c_{\text{sph}}$ . On the other hand, the height of the spicule in the  $\bar{B} = 4$  G case is less dependent on  $v_{\text{conv}}$ , as shown in Figure 2.5(c) and (d). The average

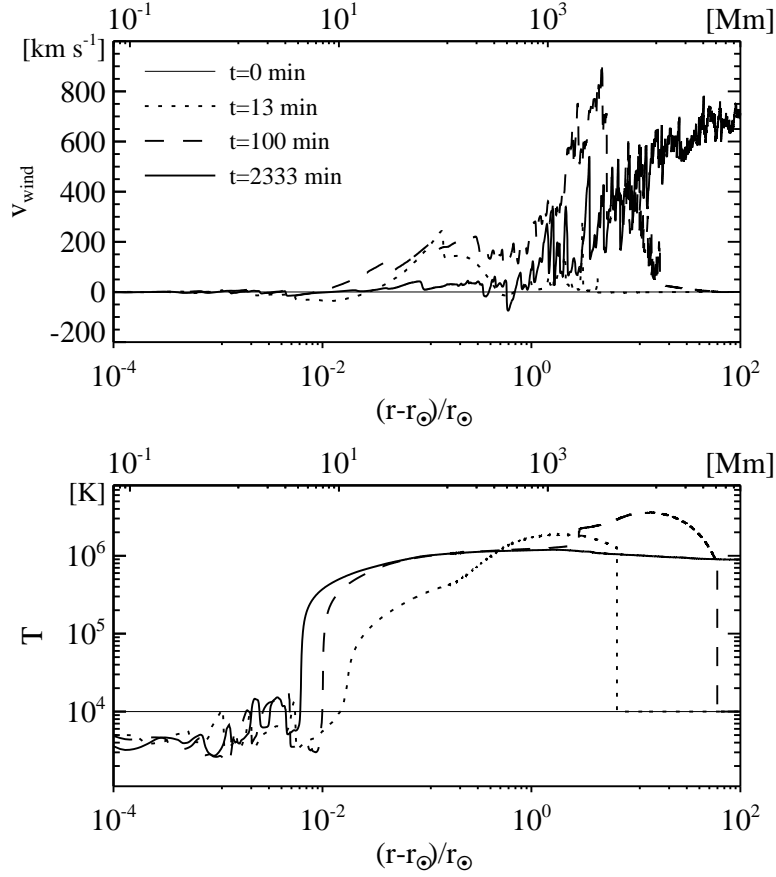


Figure 2.2: The temporal variations of the solar wind velocity (upper) and temperature (lower) given that the simulation starts in the case of  $\bar{B} = 29$  G and  $v_{\text{conv}}/c_{\text{sph}} = 0.21$ .

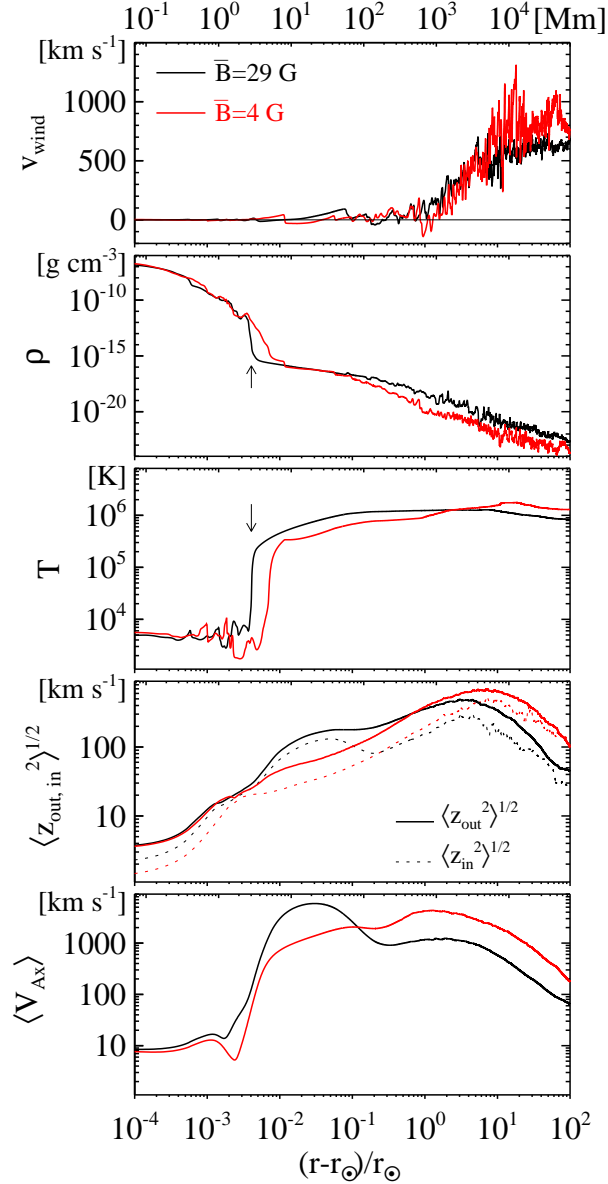


Figure 2.3: The snapshots of solar wind velocity, mass density, temperature profiles, and temporally averaged profiles of the Alfvén wave amplitude and Alfvén speed in the solar wind. The black and red lines represent the profiles in the cases of  $\bar{B} = 29$  and 4 G, respectively.  $v_{\text{conv}}/c_{\text{sph}} = 0.21$ . The corresponding times of the presented snapshots is  $t = 62$  hr in the  $\bar{B} = 29$  G case and  $t = 45$  hr in the  $\bar{B} = 4$  G case. The arrows in the second and third panels indicate the top of chromosphere ( $T = 4 \times 10^4$  K,  $\rho = 10^{-14}$  g cm $^{-3}$ ).

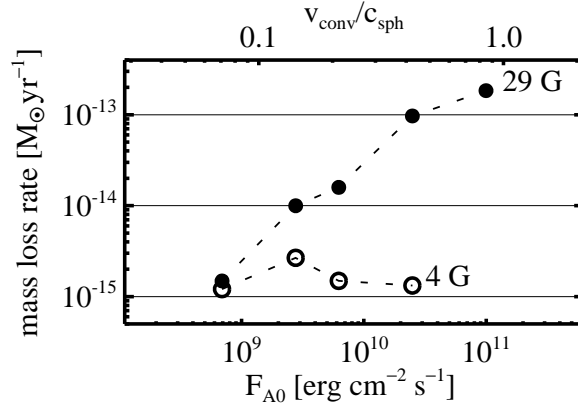


Figure 2.4: The mass-loss rates of solar wind as a function of the energy input from the photosphere ( $F_{A0}$ ). The filled and open symbols correspond to the simulation results with  $\bar{B} = 29$  and 4 G.

spicule height, as a function of  $v_{\text{conv}}$ , is summarized in Figure 2.6. The line styles and symbols are the same as those used in Figure 2.4. The spicule height is measured by tracking the isothermal contour of  $4 \times 10^4$  K, the typical temperature of the transition layer (Hegglund et al., 2011; Iijima and Yokoyama, 2015). By fitting the oscillatory pattern of the isothermal contour with the trajectories of the Lagrange particles, the individual spicules are identified, which enables us to do statistical analysis.

A common feature can be confirmed in the behaviors of the wind’s mass-loss rate (Figure 2.4) and the average spicule height (Figure 2.6). The spicule becomes monotonically taller with a larger  $v_{\text{conv}}$  in the  $\bar{B} = 29$  G case, while in  $\bar{B} = 4$  G case, it is almost independent of  $v_{\text{conv}}$ .

The less dependence of the simulated solar wind on  $v_{\text{conv}}$  implies significant wave damping below the transition layer, i.e., in the chromosphere. The difference in the spicule dynamics between  $\bar{B} = 4$  and 29 G also suggests that the propagation of a chromospheric shock wave is qualitatively affected by the parameter  $\bar{B}$ . These possibilities are further investigated in the following section.

## 2.4 Analyses

### 2.4.1 Poynting Flux by Alfvén Waves

To investigate the energy transfer by Alfvén waves, the time-averaged Poynting flux of the magnetic tension force ( $F_A = -B_\phi v_\phi B_x / (4\pi)$ ) is plotted as a function of height in Figure 2.7. The black and red lines correspond to the results in the cases of  $\bar{B} = 29$  and 4 G, respectively. Although the velocity amplitude on the photosphere is fixed at  $v_{\text{conv}}/c_{\text{sph}} = 0.21$ ,  $F_A$  below 1 Mm in the  $\bar{B} = 4$  G case is slightly larger than that in the  $\bar{B} = 29$  G case. This is caused by the reflection of the Alfvén waves at the merging height. The energy flux of the reflected (inward) Alfvén waves is plotted in Figure 2.7(b) using dotted lines, where  $F_A^{\text{out,in}} = \frac{1}{4} \rho z_{\text{out,in}}^2 V_{Ax}$ ,  $F_A = F_A^{\text{out}} - F_A^{\text{in}}$ . As seen in this plot, the inward Alfvén waves below 1 Mm comes mainly from the merging height, above which the Alfvén speed exponentially increases (Figure 2.7(c)). The energy flux of the inward Alfvén waves below 1 Mm is, therefore, related to the outward energy flux at the merging height. This leads to the smaller net energy flux when the merging height is lower.

The most remarkable feature in Figure 2.7(a) is the significant decrease in the energy flux around the transition layer in the case of  $\bar{B} = 4$  G (red line). Figure 2.8(a) shows the dependence of the  $F_A$  height

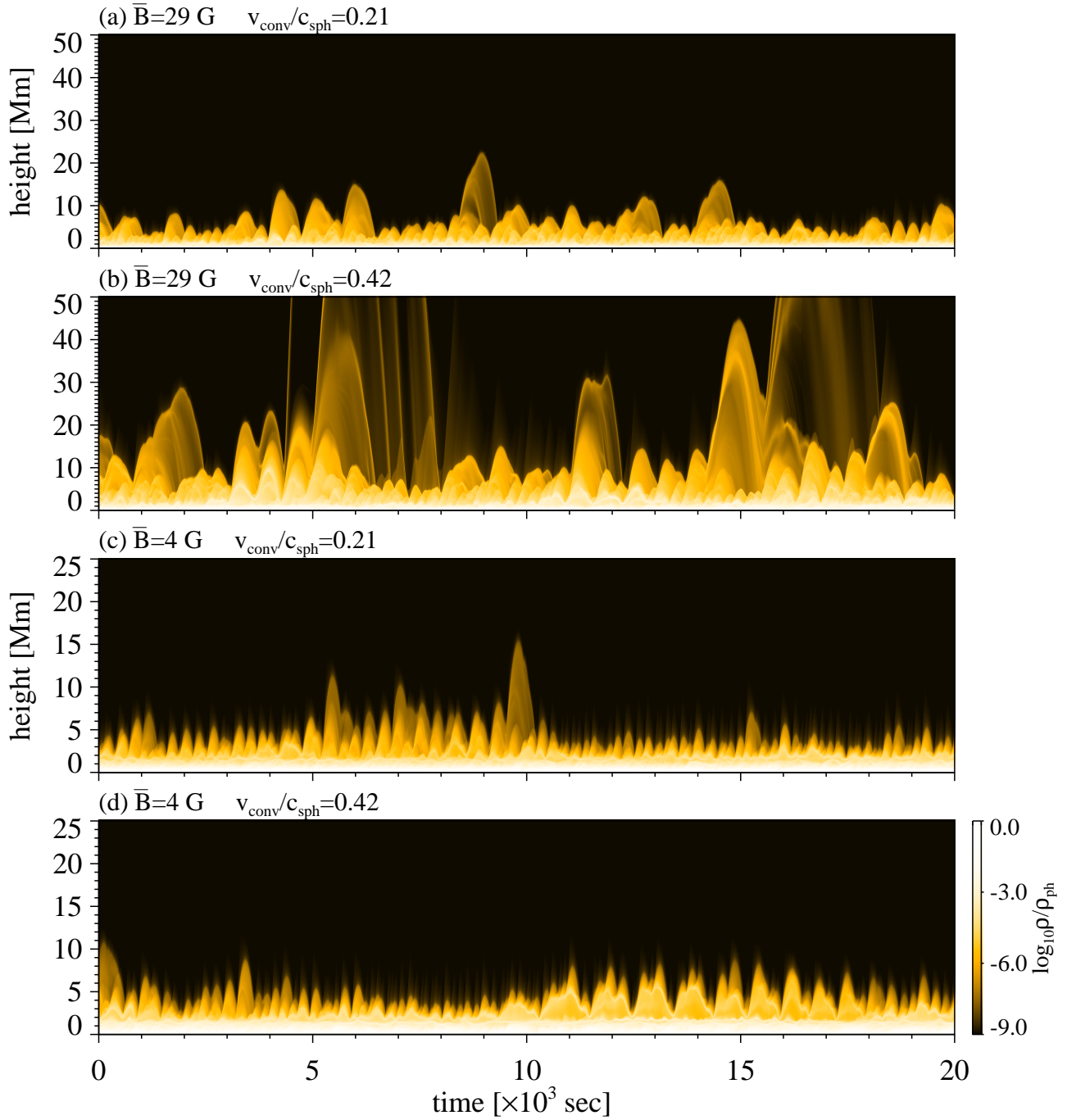


Figure 2.5: The time-slice diagrams of the mass density in the lower atmosphere. Note that the scale of height used in (a) and (b) is twice as large as that in (c) and (d). The top of the chromosphere ( $\rho/\rho_{\text{ph}} \sim 10^{-7}$ ) shows the upward and downward motions, which correspond to the spicule dynamics. The dependence of spicule dynamics on  $\bar{B}$  and  $v_{\text{conv}}$  is clearly seen in these panels. Panels (a) and (b) show the results in the cases of  $\bar{B} = 29$  G and  $v_{\text{conv}}/c_{\text{sph}} = 0.21, 0.42$ , respectively. Panels (c) and (d) correspond to the cases of  $\bar{B} = 4$  G.

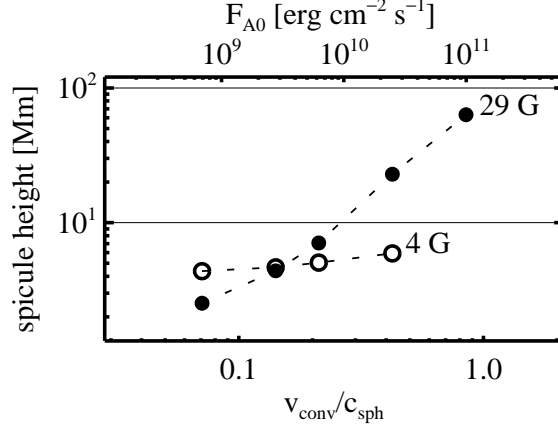


Figure 2.6: The average spicule height as a function of the velocity amplitude on the photosphere. The filled (open) circles correspond to the simulation results in the case of  $\bar{B} = 29$  G (4 G).

profile on  $v_{\text{conv}}$  in the case of  $\bar{B} = 4$  G. Although a larger  $v_{\text{conv}}$  produces a larger  $F_A$  on the bottom boundary ( $F_{A0} = 6 \times 10^8 - 2 \times 10^{10}$  erg cm $^{-2}$  s $^{-1}$  for  $v_{\text{conv}}/c_{\text{sph}} = 0.07 - 0.42$ ), the transmitted energy fluxes into the corona do not show the significant increase from  $F_A \sim 10^5$  erg cm $^{-2}$  s $^{-1}$  ( $F_A(A/A_0) \sim$  a few  $\times 10^7$  erg cm $^{-2}$  s $^{-1}$ ). In other words, the additional energy input associated with a larger  $v_{\text{conv}}$  is completely lost below the transition layer. This cannot be seen in the case of  $\bar{B} = 29$  G. Figure 2.8(b) shows that a larger energy input from the photosphere always leads to larger transmitted energy flux when  $\bar{B} = 29$  G.

## 2.4.2 Alfvén Waves in the Chromosphere

In the previous subsection, it was determined that the transmission of energy flux into the corona is limited to  $\sim 10^5$  erg cm $^{-2}$  s $^{-1}$  when the merging height is higher ( $\bar{B} = 4$  G). This suggests that Alfvén waves cannot be responsible for a Poynting flux across the chromosphere that is larger than a certain upper limit in the case of  $\bar{B} = 4$  G. Therefore, how the oscillations of toroidal velocity and magnetic field depend on the poloidal magnetic field configuration in the chromosphere was investigated.

Figure 2.9 shows the twisting motion of the magnetic flux tube in the chromosphere. Figures 2.9(a1) and (b1) show the time-slice diagram of density in the lower atmosphere when  $\bar{B} = 29$  and 4 G, respectively. Figures 2.9(a2) and (b2) show the nonlinearity of Alfvén wave amplitude. Because of the weaker  $\bar{B}$ ,  $v_\phi/V_{Ax}$  are higher in the  $\bar{B} = 4$  G case. In addition, the toroidal velocity above and below the merging height (horizontal dashed lines) often have the opposite signs when  $\bar{B} = 4$  G. Such an antiphase oscillation is rarely seen when  $\bar{B} = 29$  G. This difference is more clearly seen in Figures 2.9(a3) and (b3). These panels show the comparison of the low frequency component of the  $v_\phi$  oscillation ( $\nu < 1$  mHz). The antiphase oscillation mentioned above appears in Figure 2.9(b3).

Figures 2.10 and 2.11 depict the typical time sequence of the magnetic field lines in the cases of  $\bar{B} = 4$  and 29 G, respectively. When the merging height is low and  $\bar{B}$  is large, the upper part of the flux tube above the merging height is twisted as its lower part rotates (Figure 2.11). On the other hand, Figure 2.10 shows that the upper part of the flux tube is counterrotating against the lower part, thereby causing the formation of the break in the magnetic field line. The close-up view around such a break in the magnetic field line is shown in Figure 2.12, which corresponds to the rectangle area in Figure 2.9. The break in the magnetic field line is represented by the dashed line in this figure, which agrees with the characteristics at  $v_x + B_x/\sqrt{4\pi\rho}$ .

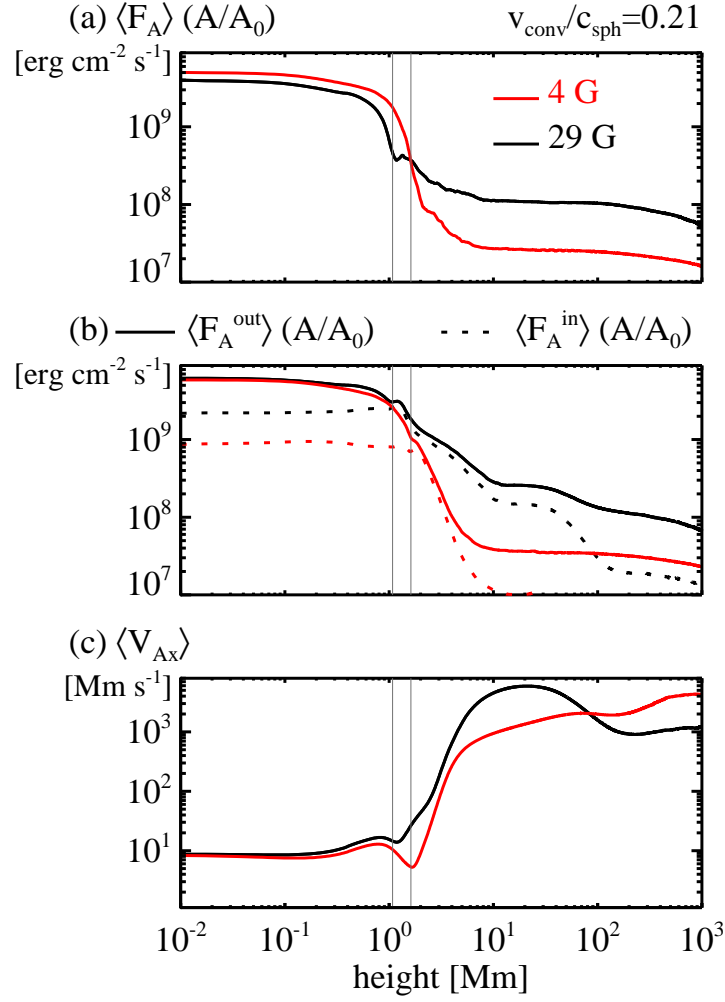


Figure 2.7: The dependence of transmissivity of Alfvén waves on different  $\bar{B}$ .  $v_{\text{conv}}/c_{\text{sph}} = 0.21$ . The black and red lines show the results in the cases of  $\bar{B} = 29$  and 4 G. Panel (a): Poynting flux by magnetic tension force  $(-B_\phi v_\phi B_x)/(4\pi)$  normalized by the cross section of the magnetic flux tube. Panel (b): outward (solid lines) and inward (dashed lines) Poynting flux by magnetic tension. Panel (c): temporally averaged profile of the Alfvén speed. The vertical gray lines correspond to the merging height  $H_m = 8, 12H_{\text{ph}}$ .

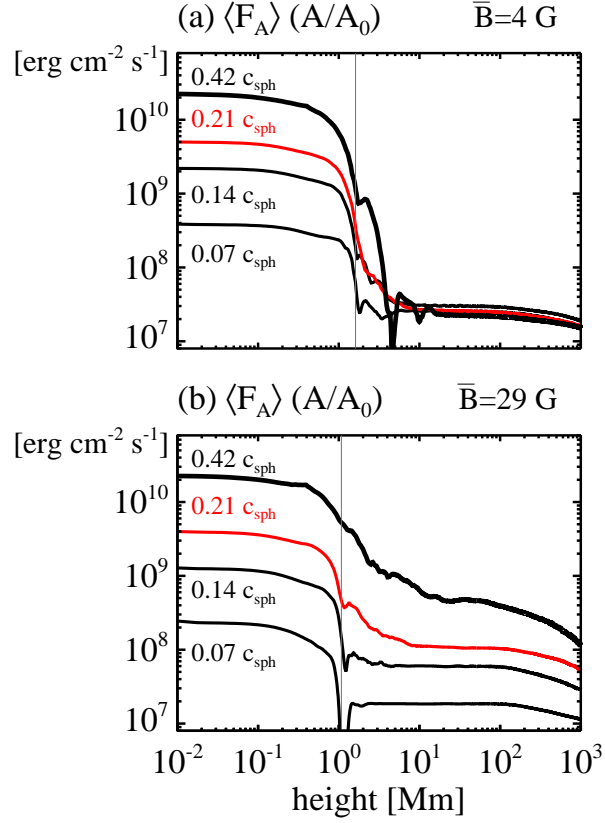


Figure 2.8: The dependence of the transmissivity of Alfvén waves on  $v_{\text{conv}}$  in the case of  $\bar{B} = 4 \text{ G}$  (panel (a)) and  $29 \text{ G}$  (panel (b)). Each profile represents the Poynting flux of the magnetic tension force normalized by the cross section of the magnetic flux tube. The thickest black line shows the simulation result with  $v_{\text{conv}}/c_{\text{sph}} = 0.42$  while the thick red and black lines show the results with  $v_{\text{conv}}/c_{\text{sph}} = 0.21, 0.14$ . The thin line corresponds to  $v_{\text{conv}}/c_{\text{sph}} = 0.07$ . Here,  $c_{\text{sph}} = \sqrt{\gamma R_g T_{\text{eff}}/\mu_{\text{ph}}}$  is the adiabatic sound speed on the photosphere.

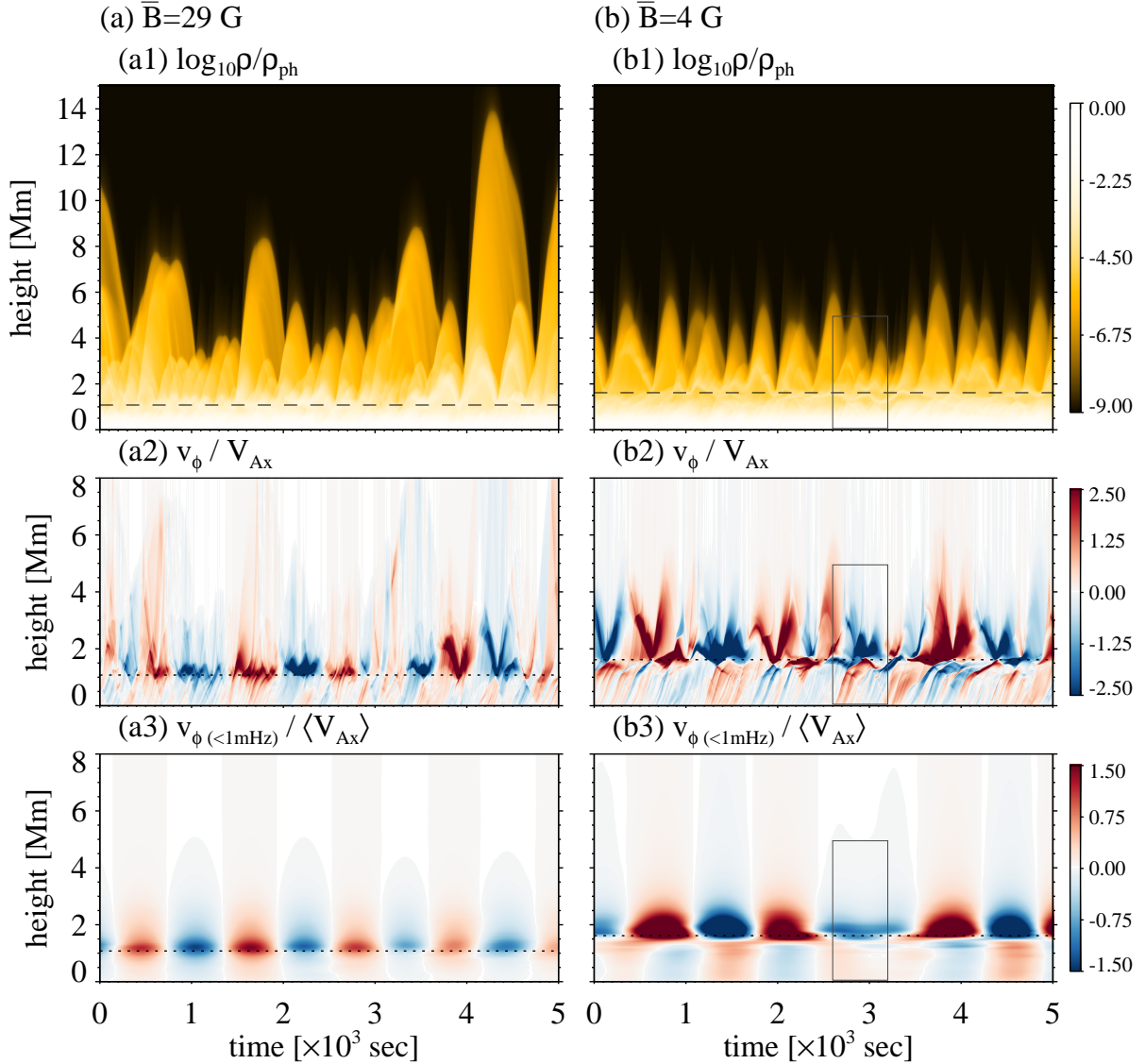


Figure 2.9: The twisting motion of the magnetic flux tube and its dependence on the merging height. The left and right columns show the results in the cases of  $\bar{B} = 29$  and 4 G, respectively.  $v_{\text{conv}}/c_{\text{sph}} = 0.21$ . The merging heights are indicated with the horizontal dashed lines. Panels (a1) and (b1): the time-slice diagram of density. Panels (a2) and (b2): the nonlinearity of toroidal velocity  $v_\phi$  with respect to the Alfvén speed  $B_x/\sqrt{4\pi\rho}$ . Panels (a3) and (b3): the nonlinearity of the low-frequency component of the toroidal velocity with respect to the Alfvén speed. The gray rectangle area corresponds to the frame of Figure 2.12.

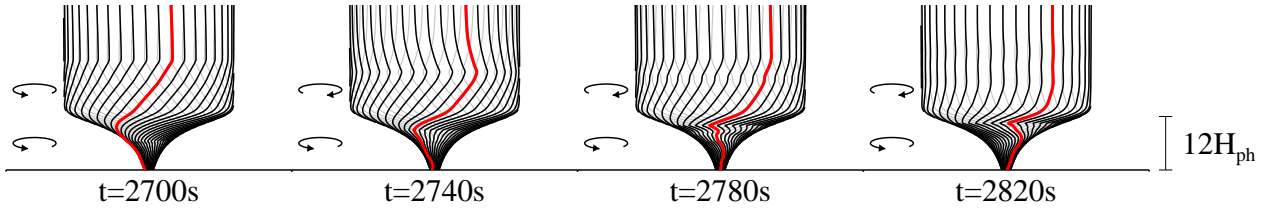


Figure 2.10: The schematic drawing of flux tube motion in the case of  $\bar{B} = 4$  G. Note that  $t = 0$  s corresponds to the same as used in Figure 2.9(b1)-(b3). This time range is within the gray rectangle in Figure 2.9.

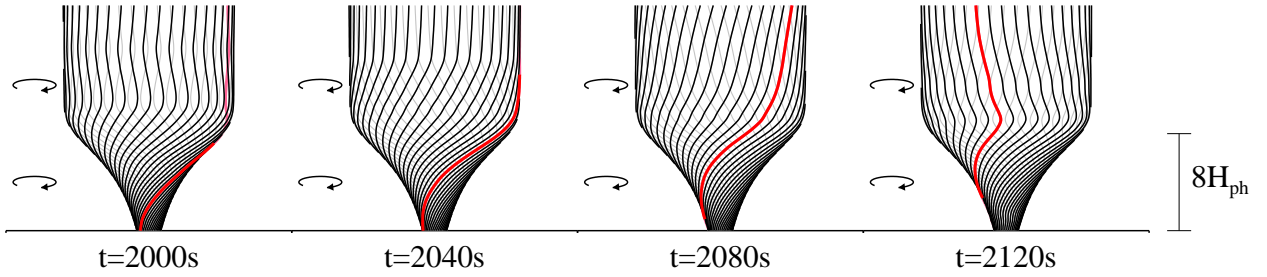


Figure 2.11: The schematic drawing of flux tube motion in the case of  $\bar{B} = 29$  G. Note that  $t = 0$  s corresponds to the same time used in Figure 2.9(a1)-(a3).

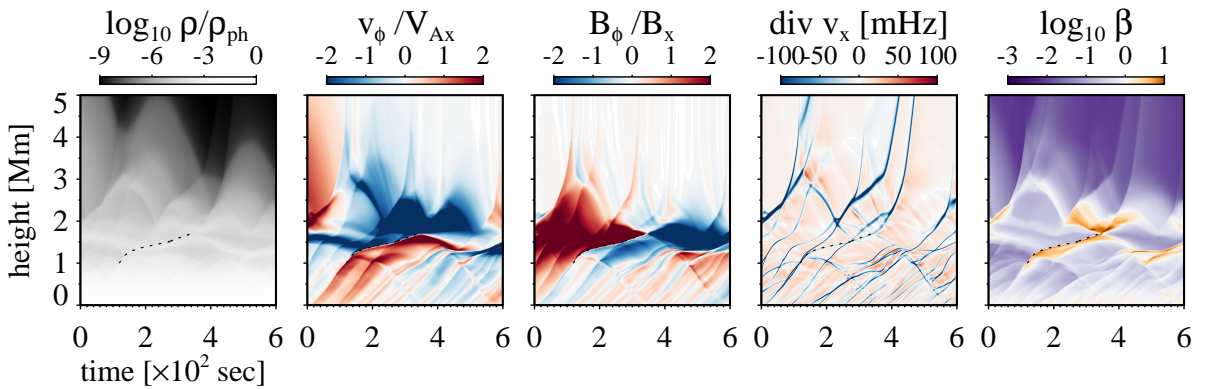


Figure 2.12: The time-slice diagram of  $B_\phi/B_x$ ,  $\text{div } v_x$ , and plasma  $\beta$  in the chromosphere, showing the highly sheared toroidal magnetic field with strong compression. The dashed line represents the propagation of the intermediate shock.  $t = 0$  s in these diagrams corresponds to  $t = 2600$  s in Figure 2.9 (The time range of this diagram corresponds to the gray rectangle in Figure 2.9.).

Figure 2.9 shows that this signature appears transiently and is associated with a compression that is strong enough to significantly enhance the plasma  $\beta$  in the downstream. The break in the magnetic field line is, therefore, identified as the intermediate shock.

### 2.4.3 Slow / Fast Shocks in the Chromosphere

The previous subsections revealed that the energy transfer by Alfvén waves is restricted in the case of a weak magnetic field ( $\bar{B} = 4$  G). Aside from such a nearly incompressible wave, the propagation of magnetoacoustic shocks, including slow and fast shocks, are possibly dependent on the magnetic field configuration in the chromosphere. In fact, Figure 2.6 shows the dependence of the average spicule height on  $v_{\text{conv}}$  changes in accordance with the magnetic field strength  $\bar{B}$ . For a comprehensive discussion, we investigated the propagation of slow and fast shocks.

The relatively strong compressible wave can be distinguished as the propagating spiky signatures with  $-\partial_x v_x > 0$ . After tracing these signatures, the Alfvén Mach number of the shock wave ( $M_A$ ) is calculated using the following formula (the derivation is described in Appendix 2.A):

$$M_A = -\frac{1}{V_A} \left( \frac{\partial v_x}{\partial x} \right)^{-1} \left\{ \frac{1}{\rho} \frac{\partial p_{\text{tot}}}{\partial x} - \frac{\partial}{\partial x} \left( \frac{GM_\odot}{r} \right) \right\} \quad (2.22)$$

where  $p_{\text{tot}} = p + B_\phi^2/(8\pi)$ . By expressing the fast- and slow-mode Mach numbers with  $M_f = M_A V_A / V_{\text{fast}}$  and  $M_s = M_A V_A / V_{\text{slow}}$  where  $V_{\text{fast}}$  and  $V_{\text{slow}}$  are the fast- and slow-mode speeds, the detected shock is specified as the fast shock when  $|M_f - 1| < |M_s - 1|$ , or, otherwise, the slow shock. This classification is justified when both fast and slow shocks are relatively weak, i.e.,  $M_f \sim 1$  and  $M_s \sim 1$ . By counting the fast (slow) shocks with  $M_f$  ( $M_s$ ) propagating around the mass density  $\rho$  in the stratified atmosphere, the distribution function of  $M_f$  or  $M_s$ , with respect to  $\rho$ , is defined as follows:

$$\frac{dN}{d \log_{10} \rho dM}(\rho, M) = \frac{dN(\rho \in [\rho_i, \rho_{i+1}], M \in [M_j, M_{j+1}])}{(\log_{10} \rho_{i+1} - \log_{10} \rho_i)(M_{j+1} - M_j)}, \quad (2.23)$$

where  $dN(\rho, M)$  is the expected number of shocks characterized with  $(\rho, M)$  in one snapshot and the subscripts  $i$  and  $j$  represent the discretization.

Figure 2.13 shows the distribution functions calculated from the simulation results in the cases of  $\bar{B} = 29$  G (upper panels) and 4 G (lower panels).  $v_{\text{conv}}/c_{\text{sph}}$  is fixed at 0.21. The vertical dotted line in each panel corresponds to the mean mass density at the transition layer. The distribution around the transition layer is artificially sparse in all panels. This is because the shock crossing the transition layer is hardly detected in this analysis (we used the time series data over 50,000 s with an interval of 4 s. This interval is much longer than that of the shock-crossing timescale across the transition layer). The cross symbol represents the most frequently appearing Mach number in each bin of  $\rho$ . Thus, the gradual rise of cross symbols seen around  $\rho \gtrsim 10^{-12}$  g cm $^{-3}$  in Figure 2.13(a2) shows the growth of the chromospheric slow shock. Note that the coronal slow shocks in Figures 2.13(a2) and (b2) are concentrated on  $M_s \sim 1/\sqrt{\gamma}$  rather than  $M_s \sim 1$ . This is because we calculated  $M_s$  by assuming  $\gamma = 5/3$  without any considerations of nonadiabatic effects. The phase speed of slow shock in the corona tends to be the isothermal sound speed  $\sim \sqrt{p/\rho}$  due to the strong heat conduction. This leads to the underestimation of  $M_s$  by a factor of  $\sim 1/\sqrt{\gamma}$  in the corona.

The most remarkable feature in this figure is that the slow shock vanishes around  $\rho \sim 10^{-11}$  g cm $^{-3}$  in Figure 2.13(b2).  $\rho = 10^{-11}$  g cm $^{-3}$  is three orders of magnitude higher than the mass density at the transition layer and roughly corresponds to the mass density around the merging height. Therefore, this disappearance of slow shock is not related to the above-mentioned artificial sparse distribution around the transition layer. Instead, it is implied that the slow shock can be evanescent in the chromosphere when the magnetic field is weak.

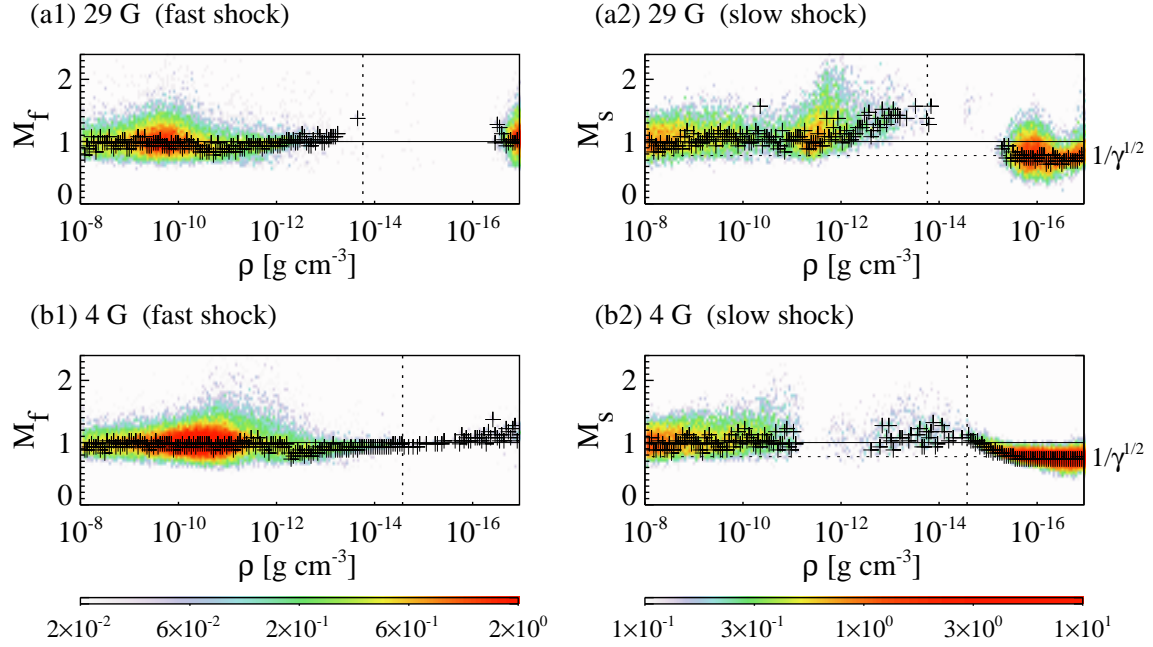


Figure 2.13: The distribution functions of the Mach number of the fast or slow shocks with respect to the atmospheric mass density  $\rho$ . The color shows the quantities defined by Equation (2.23); the expected number of shocks found in one snapshot. The cross symbol represents the most frequently appearing Mach number in each bin of  $\rho$ . Panels (a1) and (a2) show the analysis result for the case of  $\bar{B} = 29$  G while (b1) and (b2) correspond to the  $\bar{B} = 4$  G case.  $v_{\text{conv}}/c_{\text{sph}} = 0.21$ . The vertical dotted line in each panel corresponds to the mean mass density at the transition layer. The horizontal dotted lines in panels (a2) and (b2) correspond to  $M_s = 1/\sqrt{\gamma}$ .

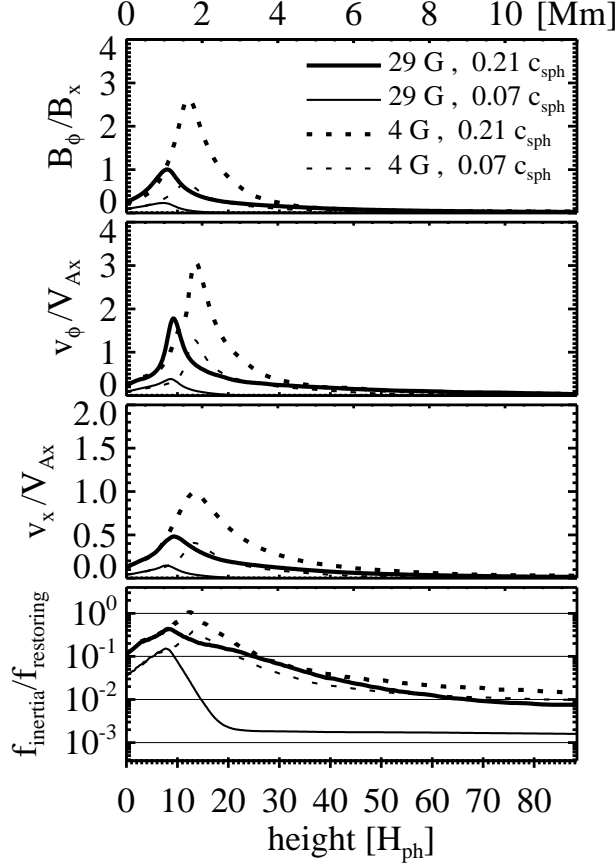


Figure 2.14: The nonlinearity of  $B_\phi$ ,  $v_\phi$ ,  $v_x$  in the lower atmosphere. The solid and dashed lines show the results in the cases of  $\bar{B} = 29$  and 4 G, respectively. The thick and thin lines show the results in the cases of  $v_{\text{conv}}/c_{\text{sph}} = 0.21$  and 0.07, respectively.

## 2.5 Discussion

### 2.5.1 Intermediate Shock in the Chromosphere

We discuss here the causal relationship between the high nonlinearity of Alfvén waves in the chromosphere and the limit on the energy transmission into the corona (Section 2.4.1).

Figure 2.14 shows the temporally averaged profiles of nonlinearity regarding  $B_\phi$ ,  $v_\phi$ , and  $v_x$ . Note that we abbreviated  $\langle (B_\phi/B_x)^2 \rangle^{1/2}$ ,  $\langle (v_\phi/V_{Ax})^2 \rangle^{1/2}$ ,  $\langle (v_x/V_{Ax})^2 \rangle^{1/2}$  into  $B_\phi/B_x$ ,  $v_\phi/V_{Ax}$ ,  $v_x/V_{Ax}$ .  $B_\phi/B_x$  and  $v_\phi/V_{Ax}$  represent the nonlinearity of Alfvén waves. The maximum level of nonlinearity is always found around the merging height. The higher merging height is responsible for the higher maximum nonlinearity of torsional ( $B_\phi$  and  $v_\phi$ ) and longitudinal ( $v_x$ ) oscillation. In particular, the high level of nonlinearity of  $v_x$  corresponds to the large inertia of the magnetic flux tube.

By using the mass conservation (Equation (3.4)) and poloidal magnetic flux conservation (Equation (2.6)), the toroidal component of the equation of motion (Equation (3.7)) can be expressed as below:

$$\frac{\partial v_\phi}{\partial t} + \frac{v_x}{\sqrt{A}} \frac{\partial(\sqrt{A}v_\phi)}{\partial x} - \frac{B_x}{4\pi\rho\sqrt{A}} \frac{\partial(\sqrt{A}B_\phi)}{\partial x} = 0. \quad (2.24)$$

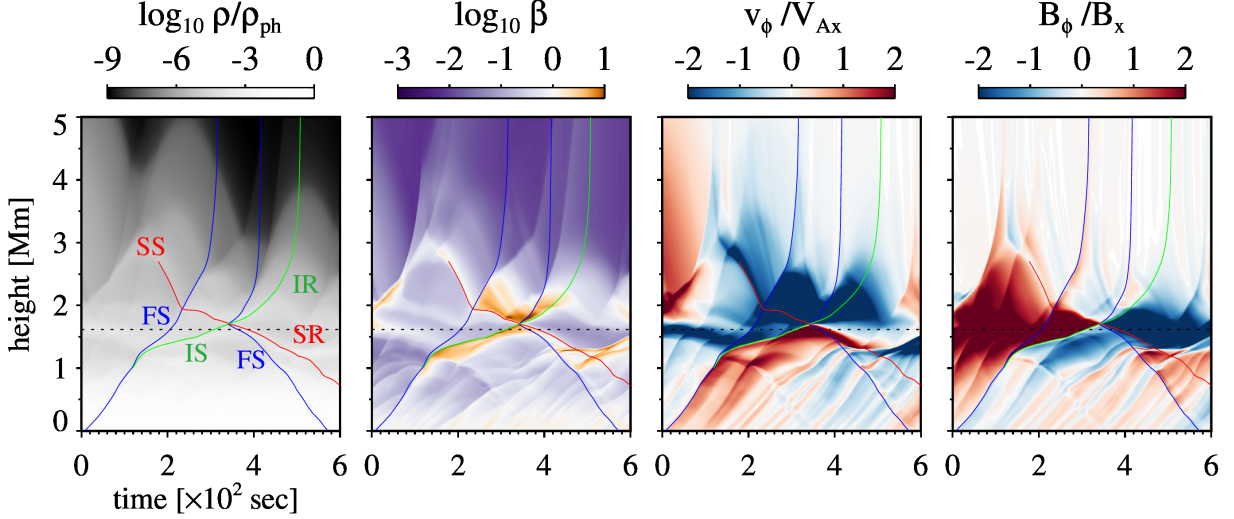


Figure 2.15: The typical scene of formation of the intermediate shock which deviates from the fast shock.  $t = 0$  s in these diagrams corresponds to  $t = 2600$  s in Figure 2.9. The intermediate shock immediately interacts with the downward slow shock and results in the intermediate rarefaction wave with negative Poynting flux. “SS”, “FS”, “IS”, “IR”, and “SR” in the leftmost panel stand for the slow shock, fast shock, intermediate shock, and intermediate rarefaction wave, slow rarefaction wave, respectively. The colored lines correspond to the trajectories of the characteristics. The horizontal dashed line represents the merging height  $H_m = 12H_{\text{ph}}$ .

The variables in the above equation are the same as those used in Section 2.2.1. The second term represents the inertia term. It can be competitive against the Lorentz force (the third term) when the longitudinal oscillation is highly nonlinear. The last panel of Figure 2.14 shows the ratio of the temporally averaged absolute value of the inertia term in relation to that of the restoring term in Equation (2.24). Here, we define the following:

$$f_{\text{inertia}} = \left\langle \left| \frac{v_x}{\sqrt{A}} \frac{\partial(\sqrt{A}v_\phi)}{\partial x} \right| \right\rangle \quad (2.25)$$

$$f_{\text{restoring}} = \left\langle \left| \frac{B_x}{4\pi\rho\sqrt{A}} \frac{\partial(\sqrt{A}B_\phi)}{\partial x} \right| \right\rangle. \quad (2.26)$$

The low ratio in the corona means that Alfvén waves can propagate without a significant nonlinear effect while the ratio around unity implies that wave propagation is strongly affected by the inertia term. In the case of the higher merging height ( $\bar{B} = 4$  G), the ratio reaches unity around the merging height, as shown with the red thick line in Figure 2.15. Due to this large inertia of the magnetic flux tube, the rotation of the upper part of the flux tube cannot be restored so easily by the twisting motion injected from the photosphere. That would result in the antiphase oscillation between the upper and lower parts of the flux tube (Figure 2.9). The highly sheared torsional flow and nonlinear longitudinal oscillation can cause the “fracture” of the flux tube, i.e., the formation of the intermediate shock (Figure 2.10). Once the intermediate shock is formed in the chromosphere, the Poynting flux associated with it hardly transmits into the corona. That is because the intermediate shock easily interacts with the slow and fast shocks or contact discontinuity, including the transition layer itself. Among these interactions, the collision of intermediate shock with the transition layer

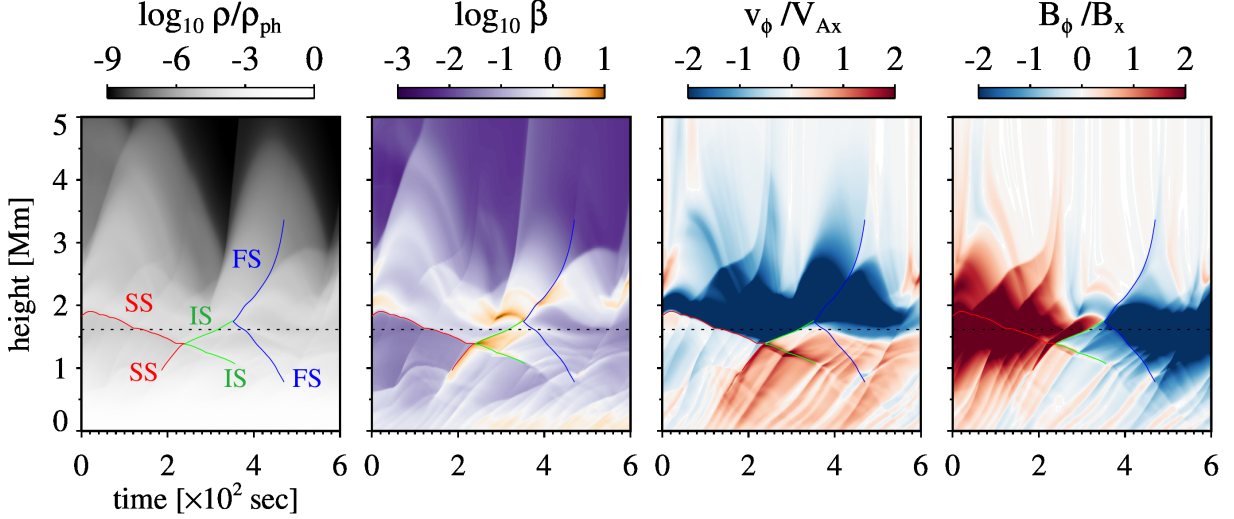


Figure 2.16: The typical scene of formation of the intermediate shock which results from the head-on collision of slow shocks.  $t = 0$  s in these diagrams corresponds to  $t = 1100$  s in Figure 2.9. “SS”, “FS”, and “IS” in the leftmost panel stand for the slow shock, fast shock, and intermediate shock, respectively. The colored lines correspond to the trajectories of characteristics. The horizontal dashed line represents the merging height  $H_m = 12H_{\text{ph}}$ .

results in the transmitted waves composed of fast rarefaction wave and slow shock. As both of them have negative Poynting fluxes, the magnetic energy transferred by the chromospheric intermediate shock is, in this sense, confined below the transition layer until its dissipation.

Figures 2.15 and 2.16 show examples on the formation of chromospheric intermediate shock. In Figure 2.15, the intermediate shock deviates from the fast shock at around  $t = 120$  s and collides with the downward slow shock at around  $t = 340$  s. Although the upward fast shock generated by this collision has a positive Poynting flux, the other resultant waves, including the upward intermediate rarefaction wave, transport the magnetic energy downward. The formation of the intermediate shock in Figure 2.16 is a result of the head-on collision of upward and downward slow shocks, which is associated with the encounter of large shear flow. The upward intermediate shock finally becomes bidirectional fast shocks after the interaction with the other waves. The dissipation of the intermediate shock is clearly exemplified in Figure 2.17. In this scene, the interaction between the sequence of intermediate shocks and the downward slow shock results in the bidirectional slow shocks. As a result, the highly sheared magnetic field line is rapidly relaxed and the super-Alfvénic torsional flow is generated.

## 2.5.2 Wave Nonlinearity in the Chromosphere

Figure 2.14 shows that the wave nonlinearity such as  $B_\phi/B_x$ ,  $v_\phi/V_{Ax}$ , and  $v_x/V_{Ax}$  is highest around the merging height. It demonstrates that higher merging height (or weaker  $\bar{B}$ ) and larger  $v_{\text{conv}}/c_{\text{sph}}$  are always associated with higher wave nonlinearity in the chromosphere. By focusing on the maximum values of the profiles plotted in Figure 2.14, the scaling relations between  $v_{\text{conv}}/c_{\text{sph}}$  and wave nonlinearity were summarized in Figure 2.18.

Figure 2.18(a) shows that the ratio of the inertia force to the restoring force is clearly correlated to

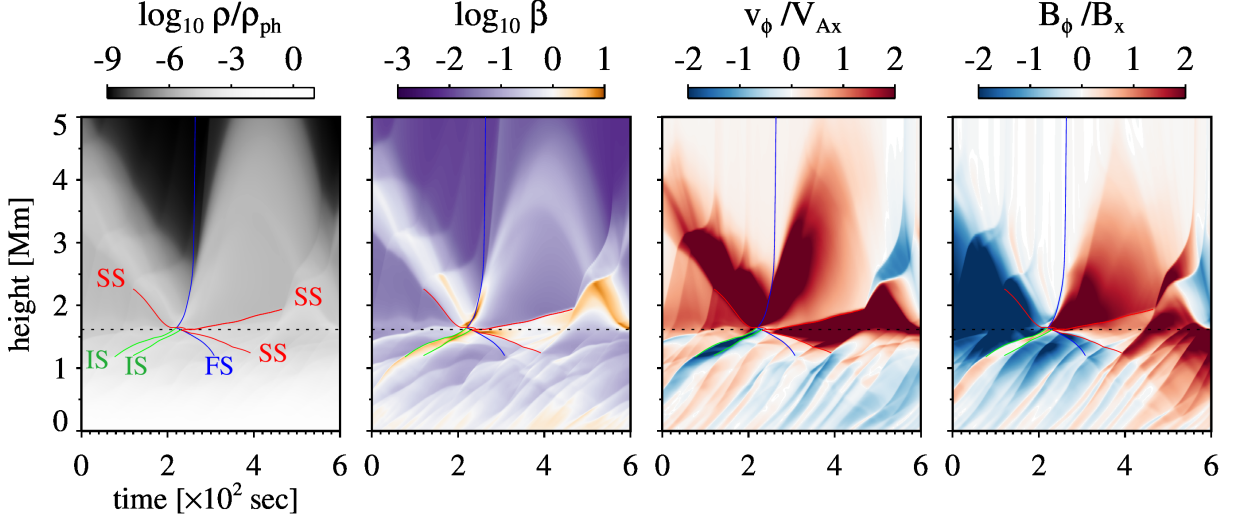


Figure 2.17: The typical scene of rapid dissipation of the intermediate shock.  $t = 0$  s in these diagrams corresponds to  $t = 400$  s in Figure 2.9. The collision between the sequences of upward intermediate shocks with the downward slow shock leads to the bidirectional slow shocks. “SS”, “FS”, and “IS” in the leftmost panel stand for the slow shock, fast shock, and intermediate shock, respectively. The colored lines correspond to the trajectories of characteristics. The horizontal dashed line represents the merging height  $H_m = 12H_{\text{ph}}$ .

$(v_{\text{conv}}/c_{\text{sph}})(\bar{B}/B_{\text{ph}})^{-1/2}$ , i.e.,

$$f_{\text{inertia}}/f_{\text{restoring}} = 0.28[(v_{\text{conv}}/c_{\text{sph}})(\bar{B}/B_{\text{ph}})^{-1/2}]^{-0.89}. \quad (2.27)$$

This scaling is composed of the relation between  $f_{\text{inertia}}/f_{\text{restoring}}$  with  $v_x/V_{Ax}$  (Figure 2.18(b)) and that between  $v_x/V_{Ax}$  with  $(v_{\text{conv}}/c_{\text{sph}})(\bar{B}/B_{\text{ph}})^{-1/2}$  (Figure 2.18(c)). In fact, Equations (2.25) and (2.26) indicate that  $f_{\text{inertia}} \sim v_x v_\phi / \lambda_A$  and  $f_{\text{restoring}} \sim B_x B_\phi / (4\pi \rho \lambda_A)$ , where  $\lambda_A$  is the wavelength of the Alfvén waves. Therefore,  $f_{\text{inertia}}/f_{\text{restoring}}$  tends to be  $v_x/V_{Ax}$  when  $v_\phi \sim B_\phi / \sqrt{4\pi\rho}$ . The amplitude of  $v_x$  basically follows the energy flux conservation for the longitudinal wave in the isothermal atmosphere. That means  $\rho v_x^2 / B_x \sim \text{constant}$  and  $v_x/V_{Ax} \propto B_x^{-1/2}$ . By using these scaling relations, it is inferred that there is a critical  $v_{\text{conv}}/c_{\text{sph}}$  or  $\bar{B}/B_{\text{ph}}$  across which the chromosphere is too highly nonlinear such that the Lorentz force associated with Alfvén wave propagation ( $f_{\text{restoring}}$ ) can no longer twist the flux tube against the large inertia force ( $f_{\text{inertia}}$ ). From Equation (2.27), we replace this critical condition of  $f_{\text{inertia}} \gtrsim f_{\text{restoring}}$  with  $0.28[(v_{\text{conv}}/c_{\text{sph}})/\sqrt{\bar{B}/B_{\text{ph}}}]^{-0.89} \gtrsim 1$  or

$$v_{\text{conv}}/c_{\text{sph}} \gtrsim 4.2\sqrt{\bar{B}/B_{\text{ph}}}. \quad (2.28)$$

This implies the following: first, for a given flux tube with  $\bar{B}/B_{\text{ph}}$ , the energy input from the photosphere larger than  $F_{A,\text{cr}} = \rho_{\text{ph}} v_{\text{conv,cr}}^2 V_{A\text{ph}}$  does not contribute to the coronal heating. As such,

$$F_{A,\text{cr}} = 2.4 \times 10^{12} \text{ erg cm}^{-2} \text{ s}^{-1} (\bar{B}/B_{\text{ph}}). \quad (2.29)$$

When  $\bar{B} = 4$  G and  $B_{\text{ph}} = 1560$  G, we find  $(v_{\text{conv}}/c_{\text{sph}})_{\text{cr}} \sim 0.21$  and  $F_{A,\text{cr}} = 6.3 \times 10^9 \text{ erg cm}^{-2} \text{ s}^{-1}$ . Second, for a given convection velocity of  $v_{\text{conv}}/c_{\text{sph}}$ , the magnetic flux tube with  $\bar{B}/B_{\text{ph}} < (\bar{B}/B_{\text{ph}})_{\text{cr}} = 0.057(v_{\text{conv}}/c_{\text{sph}})^2$  is unable to guide the magnetic energy from the lower atmosphere to the corona. When  $v_{\text{conv}}/c_{\text{sph}} = 0.21$  and  $B_{\text{ph}} = 1560$  G, we find  $\bar{B}_{\text{cr}} = 4$  G.

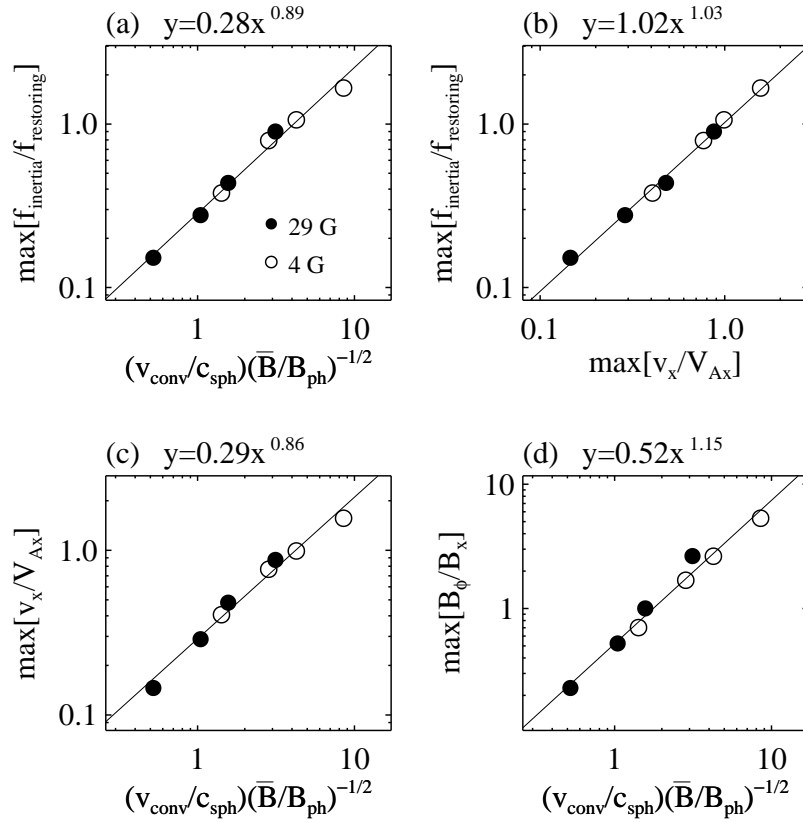


Figure 2.18: The scaling relation between  $v_{\text{conv}}/c_{\text{sph}}$  and wave nonlinearity in the chromosphere. The plotted quantities correspond to the maximum values of the profiles shown in Figure 2.14. The styles of the squares or circles are the same as those used in Figure 2.4.

Finally, it is notable that the wave nonlinearity of  $B_\phi/B_x$  follows  $B_\phi/B_x \propto (\bar{B}^{-1/2})^{1.15}$  (Figure 2.18(d)). This is accounted for by the energy flux conservation for the Alfvén waves propagating along the magnetic flux tube that expands like  $B_x^2 \propto \rho$ . Because  $\rho v_\phi^2 V_{Ax} A = \text{const.}$ , we find  $v_\phi \propto \rho^{-1/4}$  and  $B_\phi/B_x \sim v_\phi/V_{Ax} \propto \rho^{1/4}/B_x$ . Thus, when  $B_x^2 \propto \rho$ , it is obtained that  $B_\phi/B_x \propto B_x^{-1/2}$ . Hollweg (1971) and Shibata and Uchida (1985) discussed that large-amplitude Alfvén waves can be responsible for the longitudinal motion and derived the relationship of  $v_x/V_{Ax} \propto (B_\phi/B_x)^2$ . On the other hand, Figures 2.18(c) and (d) show  $v_x/V_{Ax} = 0.29[(v_{\text{conv}}/c_{\text{sph}})/\sqrt{(\bar{B}/B_{\text{ph}})}]^{0.86}$  and  $B_\phi/B_x = 0.52[(v_{\text{conv}}/c_{\text{sph}})/\sqrt{(\bar{B}/B_{\text{ph}})}]^{1.15}$ , leading to the following scaling law:

$$v_x/V_{Ax} = 0.51(B_\phi/B_x)^{0.75}. \quad (2.30)$$

### 2.5.3 Evanescence of Slow Shock in the Chromosphere

Figure 2.16 exhibits the formation of the intermediate shock as well as the disappearance of the upward slow shock. This reminds us of Figure 2.13, which shows that the slow shock is absent in the upper chromosphere when the magnetic field is weak. In addition to this head-on collision of the counterpropagating slow shocks, the head-on and rear-end collisions between the slow and intermediate shocks can disturb the upward propagation of the slow shock. These interactions would be encouraged in the highly nonlinear chromosphere, especially when the magnetic field is weak. This is because the crossing time scale of slow shock at a speed of  $\sim c_s B_x/B$  becomes longer as nonlinearity increases.

This evanescence of the slow shock in the chromosphere could result in the following two consequences about the spicule dynamics. First, the ejection speed of spicule would become smaller and less dependent on  $v_{\text{conv}}$ . Second, less frequent slow shocks in the upper chromosphere could reduce the chromospheric temperature, leading to a shorter density scale height in the chromosphere (Appendix 2.B). As a result of the smaller ejection speed and shorter density scale height, the average spicule height in the weak magnetic field tends to be lower than that in the strong magnetic field.

### 2.5.4 Comparison with Observation and Other Theoretical Studies

#### Solar Wind

The typical fast solar wind proton flux observed around 1 au is  $\sim 2 \times 10^8 \text{ cm}^{-2} \text{ s}^{-1}$  (Withbroe, 1989; Wang, 2010), comparable to the simulated value in the stronger magnetic field case ( $\sim 2.1 \times 10^8 \text{ cm}^{-2} \text{ s}^{-1}$  for  $\bar{B} = 29 \text{ G}$ ), but inconsistent with that in the weaker magnetic field case ( $\sim 0.20 \times 10^8 \text{ cm}^{-2} \text{ s}^{-1}$  for  $\bar{B} = 4 \text{ G}$ ). As discussed in Section 2.5.1, Poynting flux into the corona is limited to  $10^5 \text{ erg cm}^{-2} \text{ s}^{-1}$  when  $\bar{B} = 4 \text{ G}$ , which causes a significantly low-mass flux of solar wind. The inconsistency between the observed and simulated mass-loss rates in the  $\bar{B} = 4 \text{ G}$  case is, however, easily solved by considering the polarization of the Alfvén waves. In the present study, we used the axisymmetric coordinate system with linearly polarized Alfvén waves. The nonlinear propagation of circularly polarized Alfvén waves in the nonsteady solar wind was simulated by Suzuki and Inutsuka (2006) and Shoda et al. (2018) using the local spherically symmetric coordinate system (Shoda and Yokoyama, 2018). The differences between the axisymmetric and local spherically symmetric coordinate systems are summarized in Appendix 2.C. We also conducted a similar parameter survey on the solar atmosphere and wind structure in the local spherically symmetric coordinate system with circularly polarized Alfvén waves. Consequently, it is confirmed that the results qualitatively agree with those in the axisymmetric coordinate system. That means, even in the local spherically symmetric coordinate system, there is an upper limit on the transmitted Poynting flux into the corona when the merging height is higher ( $\bar{B} = 4 \text{ G}$ ). The wind's mass-loss rate and average spicule height

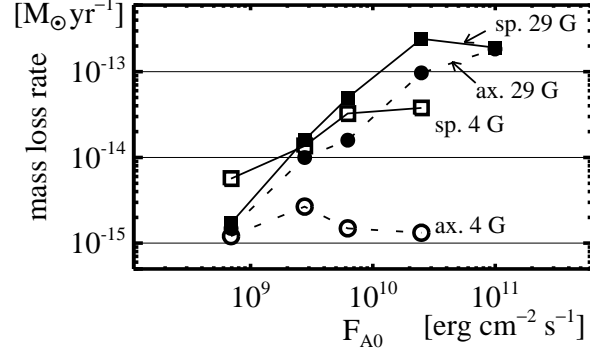


Figure 2.19: The mass-loss rates of solar wind as a function of the energy input from the photosphere ( $F_{A0}$ ). The circle (square) symbols correspond to the simulation results with the axisymmetric (local spherically symmetric) coordinate system. The filled (open) symbols mean the results of  $\bar{B}=29$  G (4 G) case.

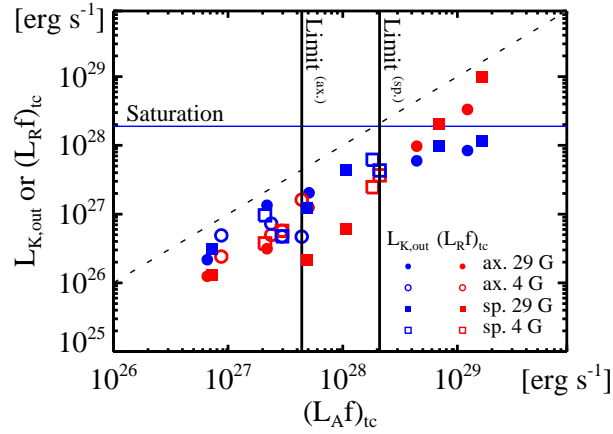


Figure 2.20: The kinetic energy flux (blue symbols) or radiative loss (red symbols) of the solar wind with respect to Poynting flux at the top of chromosphere ( $T = 2 \times 10^4$  K). This figure is analogous to Figure 8 in Suzuki et al. (2013). The blue horizontal line corresponds to the saturation level suggested by their study (Equation 2.33). The relation of  $y = x$  is also plotted using the dotted line. The thick vertical lines indicate the limit of transmitted Poynting flux found in our simulation with the axisymmetric (Limit $^{(ax.)}$ ) and local spherically symmetric coordinate systems (Limit $^{(sp.)}$ ).

become independent of the velocity amplitude on the photosphere ( $v_{\text{conv}}$ ) when  $v_{\text{conv}}/c_{\text{sph}} \gtrsim 4.2\sqrt{\bar{B}/B_{\text{ph}}}$  (Section 2.5.2). Figure 2.19 shows the mass-loss rates of solar wind as a function of the energy input from the photosphere. The filled and open circles are the same as those in Figure 2.4, and the square symbols are overplotted as the results in the local spherically symmetric coordinate system. The wind's mass-loss rate in the local spherically symmetric coordinate system with  $\bar{B} = 4$  G (open squares) appear to be constant for  $F_{A0} \gtrsim 10^{10}$  erg cm $^{-2}$  s $^{-1}$ . The upper limit of mass-loss rate simulated in the local spherically symmetric coordinate system is, however, much higher than that in the axisymmetric coordinate system. This is partly because the circularly polarized Alfvén waves transfer twice as much magnetic energy as the linearly polarized Alfvén waves when their amplitudes are the same. In other words, the critical Poynting flux  $F_{A,\text{cr}}$  (Equation (2.29)) in the local spherically symmetric coordinate system is calculated as  $F_{A,\text{cr}} = 2 \times \rho_{\text{ph}} v_{\text{conv,cr}}^2 V_{\text{Aph}}$ ,

$$F_{A,\text{cr}} = 4.8 \times 10^{12} \text{ erg cm}^{-2} \text{ s}^{-1} (\bar{B}/B_{\text{ph}}) \quad (2.31)$$

As a result, the upper limit of the transmitted Poynting flux into the corona is much larger than that in the axisymmetric coordinate system. As such, the resultant mass-loss rate can reach the observed level. Therefore, the above-mentioned inconsistency between the observed and simulated mass-loss rates in the axisymmetric coordinate system is merely an intrinsic problem of our 1D approximation.

Suzuki et al. (2013) reported their simulation results for solar and stellar winds, which showed that the wind's mass-loss rate saturates due to the enhanced radiative loss in the corona. From the time-steady energy equation, they paid attention to the following energy conservation law (in the local spherically symmetric coordinate system):

$$\left[ \rho v_r A \left( \frac{v_{\perp}^2}{2} + \frac{B_{\perp}^2}{4\pi\rho} \right) - B_r A \frac{v_{\perp} B_{\perp}}{4\pi} \right] \Big|_{r_{\text{tc}}} \approx \left[ \rho v_r A \frac{v_r^2}{2} \right] \Big|_{\infty} + \int_{r_{\text{tc}}}^{\infty} A Q_{\text{rad}} dr + \left[ \rho v_r A \frac{GM_{\odot}}{r} \right] \Big|_{r_{\text{tc}}}, \quad (2.32)$$

where  $v_{\perp}$  and  $B_{\perp}$  are the transverse components of the velocity and magnetic field.  $r_{\text{tc}}$  represents the top of the chromosphere, the position with the temperature  $T = 2 \times 10^4$  K, according to the definition by Suzuki et al. (2013). The foregoing expression means that the Poynting flux at  $r = r_{\text{tc}}$  (left-hand side) is converted to the kinetic energy of wind (the first term in the right-hand side) as well as the radiative loss and gravitational potential energy (the second and third terms in the right-hand side, respectively). While the kinetic energy of wind is positively correlated to the Alfvén waves energy at the top of the chromosphere, the large energy transmission into the corona can make radiative energy loss dominant over the kinetic energy term. That leads to the saturation of the wind's mass-loss rate. This kind of saturation is also seen in our simulation. Figure 2.20 is analogous to Figure 8 in Suzuki et al. (2013). It presents the comparison between the left-hand side of Equation (2.32) ( $(L_{Af})_{\text{tc}}$ ) with the first and second terms on the right-hand side ( $L_{K,\text{out}}$  and  $(L_{Rf})_{\text{tc}}$ ). As seen in this figure,  $(L_{Af})_{\text{tc}}$  larger than  $\sim 4 \times 10^{28}$  erg s $^{-1}$  leads to the saturation of  $L_{K,\text{out}}$ , which is associated with the enhanced  $(L_{Rf})_{\text{tc}}$ . The saturation level of  $L_{K,\text{out}}$  is almost consistent with that suggested by Suzuki et al. (2013) as shown below, indicated by the blue horizontal line in Figure 2.20.

$$L_{K,\text{out,sat}} = 2.05 \times 10^{28} \text{ erg s}^{-1} (B_{\text{ph}} f_{\text{ph}})^{1.84}. \quad (2.33)$$

This saturation is, however, not expected in the case of the higher merging height ( $\bar{B} = 4$  G). That is because the transmission of the Alfvén wave energy itself is limited due to its high nonlinearity in the chromosphere, as discussed in the previous subsection. This is why the open circles and squares are absent above a certain level of  $(L_{Af})_{\text{tc}}$ , indicated by the vertical thick lines in Figure 2.20.

## Spicule

The magnetic field configuration in the spicule has been investigated using spectropolarimetric observations (Trujillo Bueno et al., 2005; López Ariste and Casini, 2005; Orozco Suárez et al., 2015) or inferred from MHD seismology (Kim et al., 2008; Zaqarashvili et al., 2007). However, the statistics relating the spicule dynamics to magnetic field configuration have not yet been established (see Tsiropoula et al. (2012) for a review). Several observational studies suggest that the different magnetic field configurations between the quiet region and coronal hole are responsible for the difference in their spicule properties, such as their height as well as ascending and transverse speeds (Johannesson and Zirin, 1996; Zhang et al., 2012; Pereira et al., 2012). This relationship will be examined by future observations.

From the theoretical point of view, Iijima (2016) found that the average magnetic field strength is not primarily important for the length scale of a chromospheric jet based on his 2D radiation MHD simulation. On the other hand, he noted that the scale of chromospheric jets driven by torsional motion of a flux tube is possibly dependent on the average magnetic field strength. Saito et al. (2001) show that a taller spicule is associated with a lower density or stronger magnetic field based on their 1D MHD simulation. They explained, by referring to Shibata and Suematsu (1982), that a taller spicule is launched by the slow shock that grows with decreasing density or less expanding flux tube. In our simulation, the average spicule height is determined by the strength of slow shock reaching the transition layer and the density scale height in the chromosphere. When  $\bar{B} = 29$  G, the slow shock can grow with height (Figure 2.13) and drive the faster spicule. The larger  $v_{\text{conv}}$  leads to the amplified centrifugal force and the enhanced slow shock heating, both of which could contribute to the extension of density scale height in the chromosphere (Appendix 2.B). As a result, the average spicule height is taller with larger  $v_{\text{conv}}$  in the case of  $\bar{B} = 29$  G (Figure 2.6). On the other hand, when  $\bar{B} = 4$  G, the intermediate shock restricts the centrifugal force from being amplified, and the slow shock becomes evanescent in the upper chromosphere. This is why the average spicule height is less dependent on  $v_{\text{conv}}$  in the weaker  $\bar{B}$ .

### 2.5.5 Limitations to Our Model and Future Perspectives

As for the chromospheric intermediate shock, Snow and Hillier (2019) found that the decoupling of the neutral fluid against plasma can cause the intermediate shock when reconnection occurs in the partially ionized plasma. Our study and their study suggest that the chromospheric intermediate shock would be observed ubiquitously over a wide range of spatial scales in near future. The effect of partially ionized plasma can appear especially for the propagation of high-frequency Alfvén waves (Soler et al., 2019) and should be considered in future studies. Several limitations should be imposed on the application of the results of our study with regard to the real solar atmosphere and wind. The present study is based on a 1D approximation (symmetry assumption), flux tube model, and simplified radiation. Our study ignores solar rotation, collisionless effects, and various wave dissipation mechanisms, including phase-mixing and turbulent dissipation (Cranmer et al., 2007; Shoda et al., 2018). Nevertheless, it is worthwhile to emphasize that highly nonlinear Alfvén waves in the chromosphere could restrict the energy transfer from the photosphere to the corona. As such, our findings highlight the importance of the magnetic field configuration in the chromosphere in terms of the diversity of both solar and stellar atmosphere and wind structures.

## Appendix 2.A Measurement of Mach number of Fast / Slow Shocks

The Alfvén Mach numbers of fast and slow shocks in our simulation were calculated by Equation (2.22). The derivation is described here. Noting the subscripts  $u$  and  $d$  for the physical quantities in upstream and

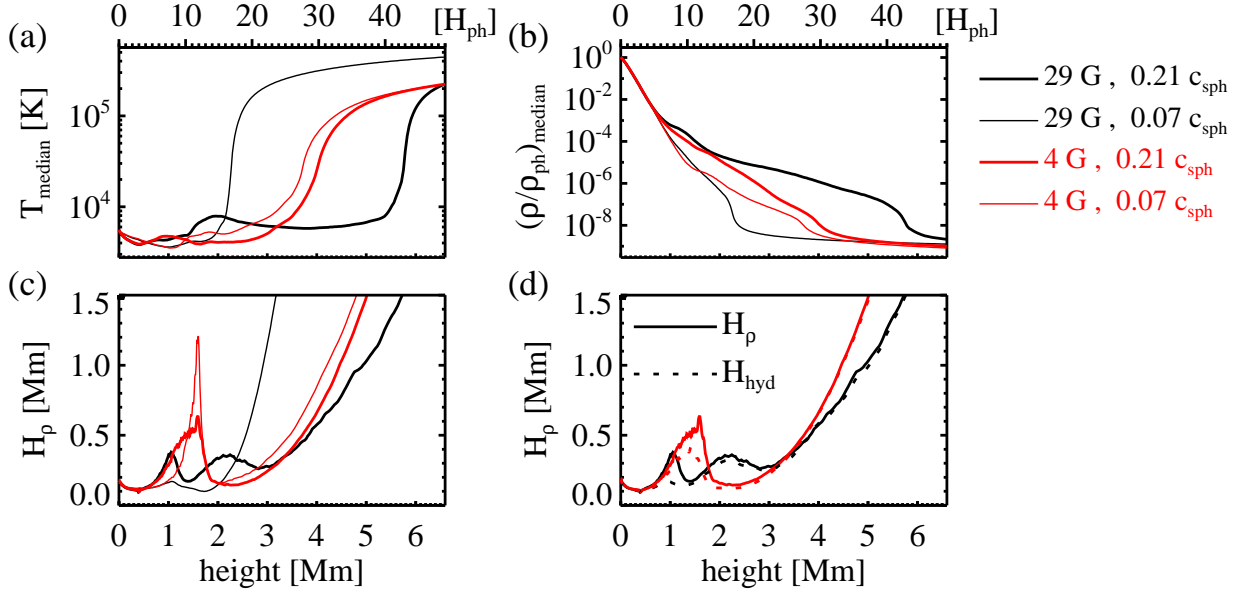


Figure 2.21: The median profile of the (a) temperature, (b) density, and averaged density scale height (c) in lower atmosphere. The black and red lines correspond to the simulation results in the cases of  $\bar{B} = 29$  and 4 G, respectively. The thin and thick lines represent the results with  $v_{\text{conv}}/c_{\text{sph}} = 0.07$  and 0.21, respectively. In panel (d), the density scale heights in the case of  $v_{\text{conv}}/c_{\text{sph}} = 0.21$  are compared to their constituents related to the stratification by gravitational acceleration and temperature gradient (dotted lines).

downstream of the shock wave, the jump condition of momentum flux across the shock front is expressed as follows:

$$\left[ \rho v_x^2 + p + \frac{B_\phi^2}{8\pi} \right]_d^u = 0. \quad (2.34)$$

Because  $\rho_u v_{xu} = \rho_d v_{xd}$  from the mass conservation,  $\rho_u v_{xu}(v_{xu} - v_{xd}) = -(p_{\text{tot}u} - p_{\text{tot}d})$ , and thus, we have

$$M_{Au} = \frac{v_{xu}}{V_{Au}} = -\frac{p_{\text{tot}u} - p_{\text{tot}d}}{\rho_u V_{Au}(v_{xu} - v_{xd})}, \quad (2.35)$$

where  $p_{\text{tot}} = p + B_\phi^2/(8\pi)$ . The above expression is, meanwhile, not practical for the estimation of the Mach number especially in the stratified atmosphere. Actually, when  $v_{xu} - v_{xd}$  approaches 0,  $|p_{\text{tot}u} - p_{\text{tot}d}|$  tends to  $\rho g_\odot \Delta x$  ( $\Delta x$  is the discretization) because of the stratification. This leads to the overestimation of the Mach number for weak shock in the lower atmosphere. In order to correct it, we used the following formula:

$$M_{Au} = -\frac{1}{V_A} \left( \frac{\partial v_x}{\partial x} \right)^{-1} \left\{ \frac{1}{\rho} \frac{\partial}{\partial x} \left( p + \frac{B_\phi^2}{8\pi} \right) - \frac{\partial}{\partial x} \left( \frac{GM_\odot}{r} \right) \right\}. \quad (2.36)$$

## Appendix 2.B Density Scale Height of the Atmosphere

The density scale height of the atmosphere follows the dynamic equilibrium determined by the poloidal component of the equation of motion:

$$\frac{\partial v_x}{\partial t} + v_x \frac{\partial v_x}{\partial x} + \frac{1}{\rho} \frac{\partial p}{\partial x} + \frac{1}{\rho} \frac{\partial}{\partial x} \left( \frac{B_\phi^2}{8\pi} \right) + \frac{B_\phi^2}{4\pi\rho} \frac{\partial \ln \sqrt{A}}{\partial x} - v_\phi^2 \frac{\partial \ln \sqrt{A}}{\partial x} - \frac{\partial}{\partial x} \left( \frac{GM_\odot}{r} \right) = 0. \quad (2.37)$$

By substituting  $p = \rho \times (p/\rho)$  and considering the temporal average, the following is obtained:

$$-\left\langle \frac{\partial \ln \rho}{\partial x} \right\rangle = \left\langle \frac{\rho v_x}{p} \frac{\partial v_x}{\partial x} \right\rangle + \left\langle \frac{1}{p} \frac{\partial}{\partial x} \left( \frac{B_\phi^2}{8\pi} \right) \right\rangle + \left\langle \frac{B_\phi^2}{4\pi p} \frac{\partial \ln \sqrt{A}}{\partial x} \right\rangle - \left\langle \frac{\rho v_\phi^2}{p} \frac{\partial \ln \sqrt{A}}{\partial x} \right\rangle + \left\langle \frac{\rho}{p} \frac{\partial}{\partial x} \left( \frac{p}{\rho} - \frac{GM_\odot}{r} \right) \right\rangle. \quad (2.38)$$

The left-hand side represents the reciprocal of the density scale height and is expressed by the harmonic mean of several scale heights:

$$\frac{1}{H_\rho} = \frac{1}{H_{\text{dyn}}} + \frac{1}{H_{\text{Bp}}} + \frac{1}{H_{\text{Bt}}} + \frac{1}{H_{\text{cnt}}} + \frac{1}{H_{\text{hyd}}} \quad (2.39)$$

Here,  $H_{\text{dyn}}$ ,  $H_{\text{Bp}}$ ,  $H_{\text{Bt}}$ , and  $H_{\text{cnt}}$  represent the scale heights, which are related to the dynamic pressure, magnetic pressure, magnetic tension force, and centrifugal force, respectively:

$$\frac{1}{H_\rho} = -\left\langle \frac{\partial \ln \rho}{\partial x} \right\rangle, \quad \frac{1}{H_{\text{dyn}}} = \left\langle \frac{\rho}{p} v_x \frac{\partial v_x}{\partial x} \right\rangle, \quad (2.40)$$

$$\frac{1}{H_{\text{Bp}}} = \left\langle \frac{1}{p} \frac{\partial}{\partial x} \left( \frac{B_\phi^2}{8\pi} \right) \right\rangle, \quad \frac{1}{H_{\text{Bt}}} = \left\langle \frac{B_\phi^2}{4\pi p} \frac{\partial \ln \sqrt{A}}{\partial x} \right\rangle, \quad (2.41)$$

$$\frac{1}{H_{\text{cnt}}} = -\left\langle \frac{\rho v_\phi^2}{p} \frac{\partial \ln \sqrt{A}}{\partial x} \right\rangle, \quad \frac{1}{H_{\text{hyd}}} = \left\langle \frac{\rho}{p} \frac{\partial}{\partial x} \left( \frac{p}{\rho} - \frac{GM_\odot}{r} \right) \right\rangle. \quad (2.42)$$

$H_{\text{hyd}}$  is the density scale height of the atmosphere in the hydrostatic equilibrium when the temperature profile is given. For the isothermal atmosphere,  $H_{\text{hyd}}$  is expressed as follows:

$$\frac{1}{H_\rho} = \frac{1}{H_{\text{hyd}}} = \frac{\mu g_\odot}{R_g T} \frac{r_\odot^2}{r^2} \frac{dr}{dx}. \quad (2.43)$$

In the expanding flux tube,  $H_{\text{cnt}}$  and  $H_{\text{Bt}}$  are always negative and positive, respectively.  $H_{\text{Bp}}$  and  $H_{\text{dyn}}$  are also usually negative and positive, respectively. These correspond to the acceleration by the magnetic pressure gradient and centrifugal force, as well as the deceleration by the magnetic tension force and dynamical pressure gradient.

Figure 2.21 shows the dependence of the density scale height on  $\bar{B}$  and  $v_{\text{conv}}$ . In Figure 2.21(c),  $H_\rho$  is plotted to see its dependence on  $v_{\text{conv}}$  and  $\bar{B}$ . The black and red lines represent the results in the  $\bar{B}=29$  and 4 G cases, respectively. The thin and thick lines correspond to the results in the  $v_{\text{conv}}/c_{\text{sph}}=0.07$  and 0.21 cases, respectively. There are two local maxima around  $\sim 1$  Mm and 2.2 Mm in the profile of  $H_\rho$  when  $(\bar{B}, v_{\text{conv}}/c_{\text{sph}}) = (29 \text{ G}, 0.21)$  (thick black line). Neither of them are seen in the  $v_{\text{conv}}/c_{\text{sph}} = 0.07$  case (thin black line). On the other hand, when  $\bar{B} = 4$  G, the profiles of  $H_\rho$  have a single maximum, regardless of the  $v_{\text{conv}}$ . In Figure 2.21(d), focus is placed on the case of  $v_{\text{conv}}/c_{\text{sph}} = 0.21$ , and  $H_\rho$  is compared to  $H_{\text{hyd}}$ .  $H_\rho$  and  $H_{\text{hyd}}$  remarkably disagree with each other around 1 Mm in the case of  $\bar{B} = 29$  G, while they agree around 2.2 Mm. These suggest that the first local maximum of  $H_\rho$  is accounted for by the magnetic pressure gradient and the centrifugal force, while the second one results from higher chromospheric temperature. Compared to the case of  $v_{\text{conv}}/c_{\text{sph}} = 0.07$ , when  $v_{\text{conv}}/c_{\text{sph}} = 0.21$ , Alfvén waves in the lower chromosphere are naturally amplified and the temperature in the upper chromosphere is increased due to the heating by the slow shock. This leads to the two local maxima in the profile of  $H_\rho$ . The single local maximum in the  $\bar{B} = 4$  G case corresponds to the first local maximum in the case of  $(\bar{B}, v_{\text{conv}}/c_{\text{sph}}) = (29 \text{ G}, 0.21)$ . This implies that the chromospheric density scale height does not extend even with a larger  $v_{\text{conv}}$  because the chromospheric temperature is less dependent on it compared to that in the case of  $\bar{B} = 29$  G. This lesser dependence of chromospheric temperature on  $v_{\text{conv}}$  would result from the evanescence of the slow shock in the upper chromosphere with a weak magnetic field.

## Appendix 2.C Axisymmetric and Local spherically Symmetric Coordinate Systems

We note the different curvilinear coordinate systems that have been traditionally employed in 1D models. The derivation of the basic equations in each coordinate system is described here.

The most general expression of our basic equations in the curvilinear coordinate system are written as follows:

$$\frac{\partial \rho}{\partial t} + \frac{1}{h_1 h_2 h_3} \sum_{\epsilon_{ijk}=1} \frac{\partial}{\partial x_i} (h_j h_k \rho v_i) = 0 \quad (2.44)$$

$$\begin{aligned} \frac{\partial}{\partial t} \left( \frac{p}{\gamma - 1} + \frac{\rho v^2}{2} + \frac{B^2}{8\pi} \right) + \frac{1}{h_1 h_2 h_3} \sum_{\epsilon_{ijk}=1} \frac{\partial}{\partial x_i} \left[ h_j h_k \left( \frac{\gamma p}{\gamma - 1} + \frac{\rho v^2}{2} + \frac{B_j^2 + B_k^2}{4\pi} \right) v_i - h_j h_k \frac{B_j v_j + B_k v_k}{4\pi} B_i \right] \\ = \sum_i \rho v_i \frac{1}{h_i} \frac{\partial}{\partial x_i} \left( \frac{GM_\odot}{r} \right) - \frac{1}{h_1 h_2 h_3} \sum_{\epsilon_{ijk}=1} \frac{\partial}{\partial x_i} (h_j h_k F_{ci}) - Q_{\text{rad}} \end{aligned} \quad (2.45)$$

$$\begin{aligned} \frac{\partial(\rho v_i)}{\partial t} + \frac{1}{h_i} \frac{\partial \Pi_{ii}}{\partial x_i} + \frac{1}{h_i h_1 h_2 h_3} \left\{ \frac{\partial}{\partial x_j} (h_k h_i^2 \Pi_{ji}) + \frac{\partial}{\partial x_k} (h_i^2 h_j \Pi_{ki}) \right\} \\ = \frac{1}{h_i} \left\{ \frac{\Pi_{jj} - \Pi_{ii}}{h_j} \frac{\partial h_j}{\partial x_i} + \frac{\Pi_{kk} - \Pi_{ii}}{h_k} \frac{\partial h_k}{\partial x_i} + \rho \frac{\partial}{\partial x_i} \left( \frac{GM_\odot}{r} \right) \right\} \end{aligned} \quad (2.46)$$

$$\frac{\partial B_i}{\partial t} + \frac{1}{h_j h_k} \left[ \frac{\partial}{\partial x_j} \{h_k (v_j B_i - v_i B_j)\} + \frac{\partial}{\partial x_k} \{h_j (v_k B_i - v_i B_k)\} \right] = 0 \quad (2.47)$$

$$\sum_{\epsilon_{ijk}=1} \frac{\partial}{\partial x_i} (h_j h_k B_i) = 0, \quad (2.48)$$

where  $h_1, h_2, h_3$  are the scale factors of the curvilinear coordinate system.  $v^2 = v_1^2 + v_2^2 + v_3^2$ ,  $B^2 = B_1^2 + B_2^2 + B_3^2$ ,  $\Pi_{ij} = \{p + B^2/(8\pi)\} \delta_{ij} + \rho v_i v_j - B_i B_j/(4\pi)$ .  $\sum_{\epsilon_{ijk}=1}$  means the summation over a set of even permutation of  $(1, 2, 3)$ .

There are two traditional approaches in simplifying the above-mentioned equations into the 1D configuration. The first one is the axisymmetric coordinate system based on the assumption that  $\partial_2 = 0$  for  $h_2, h_3, r$ , and other physical quantities, and that  $B_3 = 0$  and  $v_3 = 0$  (Hollweg et al., 1982; Kudoh and Shibata, 1999; Matsumoto and Shibata, 2010). The poloidal axis  $x_1$  represents the outer edge of the magnetic flux tube (Figure 2.22). The second is the local spherically symmetric coordinate system based on the assumption that  $\partial_2 = 0$  and  $\partial_3 = 0$  for  $h_2, h_3, r$ , and other physical quantities (Suzuki and Inutsuka, 2005; Suzuki and Inutsuka, 2006; Shoda and Yokoyama, 2018). The poloidal axis  $x_1$  in this case agrees with the radial axis of the spherical coordinate system. The scale factors  $h_2$  and  $h_3$  are specified so that  $h_2 h_3 \propto B_1^{-1}$  is along the  $x_1$ -axis in both coordinate systems. Thereafter, they can be expressed as  $h_{2,3}^{-1} = |\partial_1(\ln \sqrt{B_1})|$ , which is close to  $h_{2,3} = r$  in the distance where  $B_1 \propto r^{-2}$ . By noting  $x_1, x_2$ , and  $x_3$  with  $x, \phi$ , and  $x_3$  for the axisymmetric coordinate system or with  $x(=r), y$ , and  $z$  for the local spherically symmetric coordinate system, the following equation systems are obtained: in the axisymmetric coordinate system,

$$\frac{\partial \rho}{\partial t} + \frac{1}{A} \frac{\partial}{\partial x} (\rho v_x A) = 0 \quad (2.49)$$

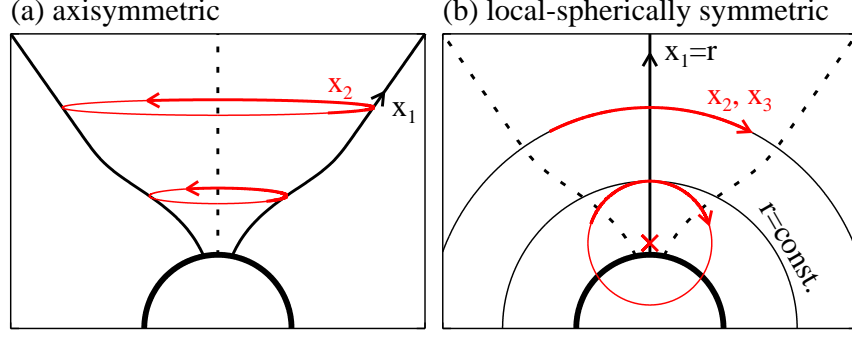


Figure 2.22: The difference between the (a) axisymmetric and (b) local spherically symmetric coordinate systems. The poloidal axis  $x_1$  is represented by solid black arrows and the toroidal or transverse axis  $x_2$  is represented by thick red arrows. The poloidal axis  $x_1$  of the local spherically symmetric coordinate system agrees with the radial axis, while that of the axisymmetric coordinate system agrees with that of the flux tube. The example of a “local sphere” in the local spherically symmetric coordinate system is shown with the thin red circle in panel (b), the center of which corresponds to the red  $\times$  symbol. The local sphere is not the same as the sphere with  $r = \text{const.}$  unless the magnetic flux tube expands radially (i.e.,  $B_1 \propto r^{-2}$ ).

$$\begin{aligned} \frac{\partial}{\partial t} \left( \frac{p}{\gamma-1} + \frac{1}{2} \rho v^2 + \frac{B^2}{8\pi} \right) + \frac{1}{A} \frac{\partial}{\partial x} \left[ A \left\{ \left( \frac{\gamma p}{\gamma-1} + \frac{\rho v^2}{2} + \frac{B_\phi^2}{4\pi} \right) v_x - \frac{B_x}{4\pi} (B_\phi v_\phi) \right\} \right] \\ = \rho v_x \frac{\partial}{\partial x} \left( \frac{GM_\odot}{r} \right) - \frac{1}{A} \frac{\partial}{\partial x} (A F_c) - Q_{\text{rad}} \end{aligned} \quad (2.50)$$

$$\frac{\partial(\rho v_x)}{\partial t} + \frac{\partial p}{\partial x} + \frac{1}{A} \frac{\partial}{\partial x} \left\{ \left( \rho v_x^2 + \frac{B_\phi^2}{8\pi} \right) A \right\} - \rho v_\phi^2 \frac{\partial \ln \sqrt{A}}{\partial x} - \rho \frac{\partial}{\partial x} \left( \frac{GM_\odot}{r} \right) = 0 \quad (2.51)$$

$$\frac{\partial(\rho v_\phi)}{\partial t} + \frac{1}{A\sqrt{A}} \frac{\partial}{\partial x} \left\{ A\sqrt{A} \left( \rho v_x v_\phi - \frac{B_x B_\phi}{4\pi} \right) \right\} = 0 \quad (2.52)$$

$$\frac{\partial B_\phi}{\partial t} + \frac{1}{\sqrt{A}} \frac{\partial}{\partial x} \left( \sqrt{A} (v_x B_\phi - v_\phi B_x) \right) = 0 \quad (2.53)$$

$$B_x A = \text{const.} \quad (2.54)$$

$$\frac{dx}{dr} = \sqrt{1 + \left( \frac{d\sqrt{A}}{dr} \right)^2}. \quad (2.55)$$

In the local spherically symmetric coordinate system,

$$\frac{\partial \rho}{\partial t} + \frac{1}{A} \frac{\partial}{\partial x} (\rho v_x A) = 0 \quad (2.56)$$

$$\begin{aligned} \frac{\partial}{\partial t} \left( \frac{p}{\gamma-1} + \frac{1}{2} \rho v^2 + \frac{B^2}{8\pi} \right) + \frac{1}{A} \frac{\partial}{\partial x} \left[ A \left\{ \left( \frac{\gamma p}{\gamma-1} + \frac{\rho v^2}{2} + \frac{B_{\perp}^2}{4\pi} \right) v_x - \frac{B_x \mathbf{B}_{\perp} \cdot \mathbf{v}_{\perp}}{4\pi} \right\} \right] \\ = -\rho v_x \frac{GM_{\odot}}{r^2} - \frac{1}{A} \frac{\partial}{\partial x} (AF_c) - Q_{\text{rad}} \end{aligned} \quad (2.57)$$

$$\frac{\partial(\rho v_x)}{\partial t} + \frac{\partial p}{\partial x} + \frac{1}{A} \frac{\partial}{\partial x} \left\{ \left( \rho v_x^2 + \frac{B_{\perp}^2}{8\pi} \right) A \right\} - \rho v_{\perp}^2 \frac{\partial \ln \sqrt{A}}{\partial x} + \rho \frac{GM_{\odot}}{r^2} = 0 \quad (2.58)$$

$$\frac{\partial(\rho \mathbf{v}_{\perp})}{\partial t} + \frac{1}{A\sqrt{A}} \frac{\partial}{\partial x} \left\{ A\sqrt{A} \left( \rho v_x \mathbf{v}_{\perp} - \frac{B_x \mathbf{B}_{\perp}}{4\pi} \right) \right\} = 0 \quad (2.59)$$

$$\frac{\partial \mathbf{B}_{\perp}}{\partial t} + \frac{1}{\sqrt{A}} \frac{\partial}{\partial x} \left( \sqrt{A} (v_x \mathbf{B}_{\perp} - \mathbf{v}_{\perp} B_x) \right) = 0 \quad (2.60)$$

$$B_x A = \text{const.} \quad (2.61)$$

where  $\mathbf{B}_{\perp} = (B_y, B_z)$  and  $\mathbf{v}_{\perp} = (v_y, v_z)$ . Because the two transverse components of the velocity and magnetic field are taken into account in the local spherically symmetric coordinate system, the circularly polarized Alfvén waves can only be discussed by using this coordinate system. However, it should be noted that the simulation result based on the local spherically symmetric coordinate system is not always representative of the dynamics of the magnetic flux tube in the 3D space, especially for the low-frequency Alfvén waves in the lower atmosphere wherein the flux tube expands superradially, and gravity cannot be ignored. This is because it is not always possible to assume both that  $\partial_x(h_y h_z B_x) = 0$  and that  $\partial_y r = \partial_z r = 0$ , as required in the local spherically symmetric coordinate system. In fact, because the local sphere with the curvature radius of  $h_y$  is not identical to the sphere radius of  $r$  unless  $B_x \propto r^{-2}$ , the gravitational acceleration is not uniform on the  $yz$  plane. Therefore, when  $B_x$  expands more strongly than  $r^{-2}$ , we can assume  $\partial_y r = \partial_z r = 0$  only along the specific direction where the  $x$ -axis agrees with the radial axis, and the gravity term, which depends on  $\partial_{y,z} r$ , affects the transverse components of the equation of motion anywhere else. This is why the assumptions that  $B_3 = 0$  and  $v_3 = 0$  are imposed in the axisymmetric coordinate system. The magnitude of the gravitational acceleration in the  $y$  component of the equation of motion around  $(y, z) = (0, 0)$  is estimated as  $\rho g_{\odot} y/R$ , where  $R = |\partial_x \ln \sqrt{B_x}|^{-1}$  is the curvature radius of the  $y$ -axis. When the flux tube expands exponentially with the pressure scale height  $H_p$  in the lower atmosphere, we find  $B_x \propto e^{-(r-r_{\odot})/(2H_p)}$  and, thus,  $R \sim 4H_p$  (see Section 2.2.2). For the propagation of the Alfvén waves with the wavelength  $\lambda_A$  and the frequency  $\nu_A$ , this gravitational acceleration is not negligible compared to the restoring force  $\sim B_x B_y / (4\pi \lambda_A)$ . In fact, by using  $y \sim v_y / \nu_A$  and  $B_y / v_y \sim \sqrt{4\pi \rho}$ , it is obtained that  $[\rho g_{\odot} v_y / \nu_A / (4H_p)] / [B_x B_y / (4\pi \lambda_A)] \sim \nu_{\text{ac}}^2 / \nu_A^2$ , where  $\nu_{\text{ac}}$  is the acoustic cutoff frequency. This means that the assumption of a local spherically symmetric coordinate system is not appropriate in describing the propagation of Alfvén waves with a frequency lower than the acoustic cutoff frequency in 3D space.

## Bibliography

Alfvén, H.

1947. Magneto hydrodynamic waves, and the heating of the solar corona. *MNRAS*, 107:211.

- An, C. H., S. T. Suess, R. L. Moore, and Z. E. Musielak  
 1990. Reflection and Trapping of Alfvén Waves in a Spherically Symmetric Stellar Atmosphere. *ApJ*, 350:309.
- Antolin, P. and K. Shibata  
 2010. The Role Of Torsional Alfvén Waves in Coronal Heating. *ApJ*, 712(1):494–510.
- Bale, S. D., M. Pulupa, C. Salem, C. H. K. Chen, and E. Quataert  
 2013. Electron Heat Conduction in the Solar Wind: Transition from Spitzer-Härm to the Collisionless Limit. *ApJL*, 769(2):L22.
- Banerjee, D., D. Pérez-Suárez, and J. G. Doyle  
 2009. Signatures of Alfvén waves in the polar coronal holes as seen by EIS/Hinode. *A&A*, 501(3):L15–L18.
- Bavassano, B., M. Dobrowolny, F. Mariani, and N. F. Ness  
 1982. Radial evolution of power spectra of interplanetary Alfvénic turbulence. *JGR*, 87(A5):3617–3622.
- Bavassano, B., E. Pietropaolo, and R. Bruno  
 2001. Radial evolution of outward and inward Alfvénic fluctuations in the solar wind: A comparison between equatorial and polar observations by Ulysses. *JGR*, 106(A6):10659–10668.
- Belcher, J. W. and J. Davis, Leverett  
 1971. Large-amplitude Alfvén waves in the interplanetary medium, 2. *JGR*, 76(16):3534.
- Belcher, J. W. and K. B. MacGregor  
 1976. Magnetic acceleration of winds from solar-type stars. *ApJ*, 210:498–507.
- Carlsson, M. and J. Leenaarts  
 2012. Approximations for radiative cooling and heating in the solar chromosphere. *A&A*, 539:A39.
- Cirtain, J. W., L. Golub, L. Lundquist, A. van Ballegoijen, A. Savcheva, M. Shimojo, E. DeLuca, S. Tsuneta, T. Sakao, K. Reeves, M. Weber, R. Kano, N. Narukage, and K. Shibasaki  
 2007. Evidence for Alfvén Waves in Solar X-ray Jets. *Science*, 318(5856):1580.
- Coleman, Paul J., J.  
 1968. Turbulence, Viscosity, and Dissipation in the Solar-Wind Plasma. *ApJ*, 153:371.
- Cranmer, S. R. and A. A. van Ballegoijen  
 2005. On the Generation, Propagation, and Reflection of Alfvén Waves from the Solar Photosphere to the Distant Heliosphere. *ApJS*, 156(2):265–293.
- Cranmer, S. R., A. A. van Ballegoijen, and R. J. Edgar  
 2007. Self-consistent Coronal Heating and Solar Wind Acceleration from Anisotropic Magnetohydrodynamic Turbulence. *ApJS*, 171(2):520–551.
- De Pontieu, B., S. W. McIntosh, M. Carlsson, V. H. Hansteen, T. D. Tarbell, C. J. Schrijver, A. M. Title, R. A. Shine, S. Tsuneta, Y. Katsukawa, K. Ichimoto, Y. Suematsu, T. Shimizu, and S. Nagata  
 2007. Chromospheric Alfvénic Waves Strong Enough to Power the Solar Wind. *Science*, 318(5856):1574.
- Derby, N. F., J.  
 1978. Modulational instability of finite-amplitude, circularly polarized Alfvén waves. *ApJ*, 224:1013–1016.

Goldstein, M. L.

1978. An instability of finite amplitude circularly polarized Alfvén waves. *ApJ*, 219:700–704.

Hahn, M. and D. W. Savin

2013. Observational Quantification of the Energy Dissipated by Alfvén Waves in a Polar Coronal Hole: Evidence that Waves Drive the Fast Solar Wind. *ApJ*, 776(2):78.

Harvey, K. L., J. Sheeley, N. R., and J. W. Harvey

1982. Magnetic measurements of coronal holes during 1975–1980. *Sol. Phys.*, 79(1):149–160.

Hasan, S. S., W. Kalkofen, A. A. van Ballegoijen, and P. Ulmschneider

2003. Kink and Longitudinal Oscillations in the Magnetic Network on the Sun: Nonlinear Effects and Mode Transformation. *ApJ*, 585(2):1138–1146.

Hasan, S. S., A. A. van Ballegoijen, W. Kalkofen, and O. Steiner

2005. Dynamics of the Solar Magnetic Network: Two-dimensional MHD Simulations. *ApJ*, 631(2):1270–1280.

Hegglund, L., V. H. Hansteen, B. De Pontieu, and M. Carlsson

2011. Wave Propagation and Jet Formation in the Chromosphere. *ApJ*, 743(2):142.

Heinemann, M. and S. Olbert

1980. Non-WKB Alfvén waves in the solar wind. *JGR*, 85(A3):1311–1327.

Heyvaerts, J. and E. R. Priest

1983. Coronal heating by phase-mixed shear Alfvén waves. *A&A*, 117:220–234.

Hollweg, J. V.

1971. Density fluctuations driven by Alfvén waves. *JGR*, 76(22):5155.

Hollweg, J. V.

1978. Alfvén waves in the solar atmosphere. *Sol. Phys.*, 56(2):305–333.

Hollweg, J. V.

1992. Alfvénically Driven Slow Shocks in the Solar Chromosphere and Corona. *ApJ*, 389:731.

Hollweg, J. V., S. Jackson, and D. Galloway

1982. Alfvén Waves in the Solar Atmospheres - Part Three - Nonlinear Waves on Open Flux Tubes. *Sol. Phys.*, 75(1-2):35–61.

Hori, K., T. Yokoyama, T. Kosugi, and K. Shibata

1997. Pseudo-Two-dimensional Hydrodynamic Modeling of Solar Flare Loops. *ApJ*, 489(1):426–441.

Iijima, H.

2016. *Numerical studies of solar chromospheric jets*. PhD thesis, Department of Earth and Planetary Science, School of Science, The University of Tokyo, Japan.

Iijima, H. and T. Yokoyama

2015. Effect of Coronal Temperature on the Scale of Solar Chromospheric Jets. *ApJL*, 812(2):L30.

Johannesson, A. and H. Zirin

1996. The Pole-Equator Variation of Solar Chromospheric Height. *ApJ*, 471:510.

- Kim, Y.-H., S.-C. Bong, Y.-D. Park, K.-S. Cho, Y.-J. Moon, and Y. Suematsu  
 2008. Estimation of Spicule Magnetic Field Using Observed MHD Waves by the Hinode SOT. *Journal of Korean Astronomical Society*, 41(6):173–180.
- Kopp, R. A. and T. E. Holzer  
 1976. Dynamics of coronal hole regions. I. Steady polytropic flows with multiple critical points. *Sol. Phys.*, 49(1):43–56.
- Kudoh, T. and K. Shibata  
 1999. Alfvén Wave Model of Spicules and Coronal Heating. *ApJ*, 514(1):493–505.
- López Ariste, A. and R. Casini  
 2005. Inference of the magnetic field in spicules from spectropolarimetry of He I D3. *A&A*, 436(1):325–331.
- Marsch, E., W. G. Pilipp, K. M. Thieme, and H. Rosenbauer  
 1989. Cooling of solar wind electrons inside 0.3 AU. *JGR*, 94(A6):6893–6898.
- Matsumoto, T. and R. Kitai  
 2010. Temporal Power Spectra of the Horizontal Velocity of the Solar Photosphere. *ApJL*, 716(1):L19–L22.
- Matsumoto, T. and K. Shibata  
 2010. Nonlinear Propagation of Alfvén Waves Driven by Observed Photospheric Motions: Application to the Coronal Heating and Spicule Formation. *ApJ*, 710(2):1857–1867.
- Matsumoto, T. and T. K. Suzuki  
 2012. Connecting the Sun and the Solar Wind: The First 2.5-dimensional Self-consistent MHD Simulation under the Alfvén Wave Scenario. *ApJ*, 749(1):8.
- Matsumoto, T. and T. K. Suzuki  
 2014. Connecting the Sun and the solar wind: the self-consistent transition of heating mechanisms. *MNRAS*, 440(2):971–986.
- Meyer, C. D., D. S. Balsara, and T. D. Aslam  
 2012. A second-order accurate Super TimeStepping formulation for anisotropic thermal conduction. *MNRAS*, 422(3):2102–2115.
- Meyer, C. D., D. S. Balsara, and T. D. Aslam  
 2014. A stabilized Runge-Kutta-Legendre method for explicit super-time-stepping of parabolic and mixed equations. *Journal of Computational Physics*, 257:594–626.
- Miyoshi, T. and K. Kusano  
 2005. A multi-state HLL approximate Riemann solver for ideal magnetohydrodynamics. *Journal of Computational Physics*, 208(1):315–344.
- Moriyasu, S., T. Kudoh, T. Yokoyama, and K. Shibata  
 2004. The Nonlinear Alfvén Wave Model for Solar Coronal Heating and Nanoflares. *ApJL*, 601(1):L107–L110.
- Nagai, F.  
 1980. A Model of Hot Loops Associated with Solar Flares - Part One - Gasdynamics in the Loops. *Sol. Phys.*, 68(2):351–379.

- Okamoto, T. J. and B. De Pontieu  
2011. Propagating Waves Along Spicules. *ApJL*, 736(2):L24.
- Orozco Suárez, D., A. Asensio Ramos, and J. Trujillo Bueno  
2015. Height Variation of the Vector Magnetic Field in Solar Spicules. *ApJL*, 803(2):L18.
- Osterbrock, D. E.  
1961. The Heating of the Solar Chromosphere, Plages, and Corona by Magnetohydrodynamic Waves. *ApJ*, 134:347.
- Parker, E. N.  
1964. Dynamical Properties of Stellar Coronas and Stellar Winds. II. Integration of the Heat-Flow Equation. *ApJ*, 139:93.
- Pereira, T. M. D., B. De Pontieu, and M. Carlsson  
2012. Quantifying Spicules. *ApJ*, 759(1):18.
- Saito, T., T. Kudoh, and K. Shibata  
2001. What Determines the Height of Spicules? I. Alfvén-Wave Model and Slow-Wave Model. *ApJ*, 554(2):1151–1158.
- Shibata, K. and Y. Suematsu  
1982. Why are spicules absent over plages and long under coronal holes? *Sol. Phys.*, 78(2):333–345.
- Shibata, K. and Y. Uchida  
1985. A magnetodynamic mechanism for the formation of astrophysical jets. I - Dynamical effects of the relaxation of nonlinear magnetic twists. *PASJ*, 37(1):31–46.
- Shoda, M., T. K. Suzuki, M. Asgari-Targhi, and T. Yokoyama  
2019. Three-dimensional Simulation of the Fast Solar Wind Driven by Compressible Magnetohydrodynamic Turbulence. *ApJL*, 880(1):L2.
- Shoda, M. and T. Yokoyama  
2018. High-frequency Spicule Oscillations Generated via Mode Conversion. *ApJ*, 854(1):9.
- Shoda, M., T. Yokoyama, and T. K. Suzuki  
2018. A Self-consistent Model of the Coronal Heating and Solar Wind Acceleration Including Compressible and Incompressible Heating Processes. *ApJ*, 853(2):190.
- Shu, C.-W. and S. Osher  
1988. Efficient Implementation of Essentially Non-oscillatory Shock-Capturing Schemes. *Journal of Computational Physics*, 77(2):439–471.
- Snow, B. and A. Hillier  
2019. Intermediate shock sub-structures within a slow-mode shock occurring in partially ionised plasma. *A&A*, 626:A46.
- Soler, R., J. Terradas, R. Oliver, and J. L. Ballester  
2019. Energy Transport and Heating by Torsional Alfvén Waves Propagating from the Photosphere to the Corona in the Quiet Sun. *ApJ*, 871(1):3.

Spitzer, L. and R. Härm

1953. Transport Phenomena in a Completely Ionized Gas. *Physical Review*, 89(5):977–981.

Suzuki, T. K.

2006. Forecasting Solar Wind Speeds. *ApJL*, 640(1):L75–L78.

Suzuki, T. K.

2007. Structured Red Giant Winds with Magnetized Hot Bubbles and the Corona/Cool Wind Dividing Line. *ApJ*, 659(2):1592–1610.

Suzuki, T. K.

2018. Stellar winds and coronae of low-mass Population II/III stars. *PASJ*, 70(3):34.

Suzuki, T. K., S. Imada, R. Kataoka, Y. Kato, T. Matsumoto, H. Miyahara, and S. Tsuneta

2013. Saturation of Stellar Winds from Young Suns. *PASJ*, 65:98.

Suzuki, T. K. and S.-i. Inutsuka

2005. Making the Corona and the Fast Solar Wind: A Self-consistent Simulation for the Low-Frequency Alfvén Waves from the Photosphere to 0.3 AU. *ApJL*, 632(1):L49–L52.

Suzuki, T. K. and S.-I. Inutsuka

2006. Solar winds driven by nonlinear low-frequency Alfvén waves from the photosphere: Parametric study for fast/slow winds and disappearance of solar winds. *Journal of Geophysical Research (Space Physics)*, 111(A6):A06101.

Terasawa, T., M. Hoshino, J. I. Sakai, and T. Hada

1986. Decay instability of finite-amplitude circularly polarized Alfvén waves: A numerical simulation of stimulated Brillouin scattering. *JGR*, 91(A4):4171–4187.

Trujillo Bueno, J., L. Merenda, R. Centeno, M. Collados, and E. Landi Degl’Innocenti

2005. The Hanle and Zeeman Effects in Solar Spicules: A Novel Diagnostic Window on Chromospheric Magnetism. *ApJL*, 619(2):L191–L194.

Tsiropoula, G., K. Tziotziou, I. Kontogiannis, M. S. Madjarska, J. G. Doyle, and Y. Suematsu

2012. Solar Fine-Scale Structures. I. Spicules and Other Small-Scale, Jet-Like Events at the Chromospheric Level: Observations and Physical Parameters. *SSRv*, 169(1-4):181–244.

Velli, M.

1993. On the propagation of ideal, linear Alfvén waves in radially stratified stellar atmospheres and winds. *A&A*, 270(1-2):304–314.

Wang, Y. and T. Yokoyama

2020. Simulation of Alfvén Wave Propagation in the Magnetic Chromosphere with Radiative Loss: Effects of Nonlinear Mode Coupling on Chromospheric Heating. *ApJ*, 891(2):110.

Wang, Y. M.

2010. On the Relative Constancy of the Solar Wind Mass Flux at 1 AU. *ApJL*, 715(2):L121–L127.

Wang, Y. M., J. Lean, and J. Sheeley, N. R.

2000. The long-term variation of the Sun’s open magnetic flux. *GeoRL*, 27(4):505–508.

Washinoue, H. and T. K. Suzuki

2019. Coroneae of Zero/Low-metal, Low-mass Stars. *ApJ*, 885(2):164.

Wiegelmann, T. and S. K. Solanki

2004. Similarities and Differences between Coronal Holes and the Quiet Sun: Are Loop Statistics the Key? *Sol. Phys.*, 225(2):227–247.

Withbroe, G. L.

1989. The Solar Wind Mass Flux. *ApJL*, 337:L49.

Yasuda, Y., T. K. Suzuki, and T. Kozasa

2019. Alfvén Wave-driven Wind from RGB and AGB Stars. *ApJ*, 879(2):77.

Zaqarashvili, T. V., E. Khutsishvili, V. Kukhianidze, and G. Ramishvili

2007. Doppler-shift oscillations in solar spicules. *A&A*, 474(2):627–632.

Zhang, Y. Z., K. Shibata, J. X. Wang, X. J. Mao, T. Matsumoto, Y. Liu, and J. T. Su

2012. Revision of Solar Spicule Classification. *ApJ*, 750(1):16.

## Chapter 3

# Nonlinear Alfvén Wave Model of Stellar Coronae and Winds from the Sun to M dwarfs

An M dwarf’s atmosphere and wind are expected to be highly magnetized. The nonlinear propagation of Alfvén waves could play a key role in both heating the stellar atmosphere and driving the stellar wind. Using this Alfvén wave scenario, we carried out a one-dimensional compressive magnetohydrodynamic (MHD) simulation to examine the nonlinear propagation of Alfvén waves from the M dwarf’s photosphere, chromosphere to the corona and interplanetary space. Based on the simulation results, we developed a semi-empirical method describing the solar and M dwarf’s coronal temperature, stellar wind velocity, and wind’s mass-loss rate. We find that M dwarfs’ coronae tend to be cooler than the solar corona, and that M dwarfs’ stellar winds can be characterized as having a faster velocity and much smaller mass-loss rate compared to those of the solar wind.

### 3.1 Introduction

M-type main-sequence stars (M dwarfs) have a highly magnetized atmosphere. Discussion of their magnetic activities has focused in particular on their impact on the planetary atmosphere ([Khodachenko et al., 2007](#); [Lammer et al., 2007](#); [Scalo et al., 2007](#); [Tarter et al., 2007](#); [Seager, 2013](#)). It is important for studies about the exoplanets or astrobiology to reveal the underlying physics for the structure of the stellar atmosphere and wind ([Vidotto et al., 2014](#); [Linsky, 2019](#); [Mesquita and Vidotto, 2020](#)).

The most promising mechanism for both heating the stellar atmosphere and driving the stellar wind is the nonlinear processes related to the Alfvén waves ([Velli, 1993](#); [Cranmer and Saar, 2011](#)). Alfvén waves are responsible for the transfer of magnetic energy in the magnetized plasma, and are involved in energy conversion to the kinetic or thermal energy of the background media through the nonlinear processes. Based on this scenario, the three-dimensional (3D) magnetohydrodynamic (MHD) global model for the solar atmosphere and wind (Alfvén Wave Solar Model (AWSoM) by [van der Holst et al. \(2014\)](#)) has been developed to investigate the stellar wind of M dwarfs and the environments around their planets ([Cohen et al., 2014](#); [Garraffo et al., 2017](#); [Dong et al., 2018](#); [Alvarado-Gómez et al., 2020](#)).

Although these studies discuss the 3D global structure of the stellar wind and magnetic field configuration,

their applicability is limited due to the following two properties intrinsic to their models. First, the inner boundary of their models is placed at the “top of the stellar chromosphere,” and the Alfvén wave amplitude on that height is given by the empirical law (Sokolov et al., 2013). Second, the interaction between the Alfvén wave and the stellar wind is considered in a much simplified way using analytical, empirical, or phenomenological terms, because the propagating Alfvén wave cannot be resolved directly in the 3D simulations owing to the low spatial resolution. The effect of the other compressible waves on the stellar wind and Alfvén wave propagation is neglected.

These difficulties in the above 3D global model have been addressed by numerical studies about the nonlinear propagation of Alfvén waves along the single magnetic flux tube in the solar atmosphere from the photosphere and chromosphere to the corona (Hollweg et al., 1982; Kudoh and Shibata, 1999; Matsumoto and Shibata, 2010) and solar wind (Suzuki and Inutsuka, 2005; Suzuki and Inutsuka, 2006; Matsumoto and Suzuki, 2012; Matsumoto and Suzuki, 2014; Shoda et al., 2018; Shoda et al., 2019; Sakaue and Shibata, 2020; Matsumoto, 2021). These approaches also have been extended to the stellar atmosphere and wind models (Suzuki et al., 2013; Suzuki, 2018; Shoda et al., 2020), and have revealed that the Alfvén wave amplitude on the top of chromosphere should be self-consistently determined as a consequence of wave dissipation and reflection in the chromosphere. In addition, owing to their high-resolution simulations, it is found that, while the atmosphere and wind are maintained by the energy and momentum transfer by Alfvén waves, its propagation is affected by the dynamics of atmosphere and wind. These studies highlight the importance of resolving the local dynamics associated with the Alfvén wave propagation, as well as reproducing the global structure of the solar and stellar atmosphere and wind.

In this Letter, therefore, we extend our recent solar atmosphere and wind model (Sakaue and Shibata, 2020) to the M dwarf’s atmosphere and wind. By carrying out one-dimensional (1D) time-dependent MHD simulations, the nonlinear propagation of Alfvén waves in the nonsteady stellar atmosphere and wind is calculated from the M dwarf’s photosphere and chromosphere to the corona and interplanetary space. The primary goal of this Letter is to summarize the differences in the reproduced stellar atmosphere and wind structures between the Sun and M dwarfs. The physical mechanisms for such a diversity of stellar atmospheres and wind are also discussed here and will be more quantitatively investigated in a subsequent paper (Sakaue & Shibata, to be submitted), in which we develop the semi-empirical method describing the stellar atmosphere and wind parameters (coronal temperature, wind velocity and mass-loss rate) based on the simulation results.

## 3.2 Numerical Setting

The nonlinear propagation of the Alfvén wave in the time-dependent stellar atmosphere and wind is simulated by using 1D MHD equations based on the axial symmetry assumption of the magnetic flux tube (see Appendix 3.A and Sakaue and Shibata (2020)). The surface of the axisymmetric flux tube is defined by the poloidal and toroidal axes, which are noted in this study with  $x$  and  $\phi$  (Figure 3.1). There are three free parameters determining the magnetic flux tube configuration used in this study, including the photospheric magnetic field strength ( $B_{\text{ph}}$ ), chromospheric magnetic field strength ( $\bar{B}$ ), and filling factor of the open flux tube on the photosphere ( $f_{\text{ph}}$ ). Among them,  $B_{\text{ph}}$  is assumed to be equipartition to the photospheric plasma pressure, and  $f_{\text{ph}}$  is fixed at 1/1600.

By employing the different stellar photospheres as the boundary conditions, we considered the stellar atmospheres and winds of the Sun and two M dwarfs, including AD Leo (M3.5) and TRAPPIST-1 (M8). The stellar mass ( $M_{\star}$ ), radius ( $r_{\star}$ ), and effective temperature ( $T_{\text{eff}}$ ) of AD Leo are  $0.47M_{\odot}$ ,  $0.46r_{\odot}$ , and 3473 K, respectively (Maldonado et al., 2015), where  $M_{\odot} = 2.0 \times 10^{33}$  g and  $r_{\odot} = 7.0 \times 10^{10}$  cm are the solar mass and radius. TRAPPIST-1’s  $M_{\star}$ ,  $r_{\star}$ , and  $T_{\text{eff}}$  are  $0.08M_{\odot}$ ,  $0.12r_{\star}$ , and 2559 K, respectively (Gillon

et al., 2016). These basic parameters imply that M dwarfs are characterized with the larger gravitational acceleration ( $g_*$ ), shorter pressure scale height of the photosphere ( $H_{\text{ph}} = RT_{\text{eff}}/(\mu_{\text{ph}}g_*)$ ), and almost the same surface escape velocity  $v_{\text{esc}\star}$ , compared to the Sun. In fact,  $\log_{10} g_* = 4.44, 4.79,$  and  $5.21$  for the Sun, AD Leo, and TRAPPIST-1, respectively.  $H_{\text{ph}} = 130, 29,$  and  $6.9$  km as well, and  $v_{\text{esc}\star} = 618, 624,$  and  $511$  km s $^{-1}$ .

The outwardly propagating Alfvén wave is excited on the photosphere by imposing the velocity and magnetic fluctuations on the bottom boundary, which represent the surface convective motion. The mass density and convective velocity on the photosphere is calculated based on the opacity table presented by Freedman et al. (2014) and surface convection theory by Ludwig et al. (2002, 1999), and Magic et al. (2015). The outer boundary is set at  $r \gtrsim 100r_*$ , and 19200 grids are placed nonuniformly. The numerical scheme is based on the HLLD Riemann solver (Miyoshi and Kusano, 2005) with the second-order MUSCL interpolation and the third-order TVD Runge-Kutta method (Shu and Osher, 1988). The heat conduction is solved by the super-time-stepping method (Meyer et al., 2012). We also performed the parameter survey about the chromospheric magnetic field strength and the velocity amplitude on the photosphere for each star.

### 3.3 Typical Simulation Results

After several tens of hours, the stellar wind in the simulation box reaches the quasi-steady state. In the particular case of the M3.5 dwarf shown in Figure 3.2, it is found that the stellar wind velocity reaches around 900 km s $^{-1}$ , and that the transition layer appears in the temperature profile around 1 Mm, dividing the lower-temperature chromosphere and 1 MK corona.

To characterize the physical quantities of quasi-steady state of stellar atmospheres and winds, we investigate the integrals of the basic equations. First is the integral of the equation of motion, which is obtained by temporally averaging and spatially integrating Equation (3.6).

$$v_x^2(r) = \Delta_p^r + \Delta_{p_B}^r + \Delta_c^r + \Delta_t^r + \Delta_g^r. \quad (3.1)$$

The right-hand side terms are defined as  $\Delta_p^r = -2 \int_{r_*}^r \left\langle \frac{1}{\rho} \frac{\partial p}{\partial x} \right\rangle dx$ , where  $\langle \cdot \rangle$  means the temporal average,  $\Delta_{p_B}^r = -2 \int_{r_*}^r \left\langle \frac{1}{\rho} \frac{\partial}{\partial x} \left( \frac{B_\phi^2}{8\pi} \right) \right\rangle dx$ ,  $\Delta_c^r = 2 \int_{r_*}^r \langle v_\phi^2 \rangle \frac{\partial \ln \sqrt{A}}{\partial x} dx$ ,  $\Delta_t^r = -2 \int_{r_*}^r \left\langle \frac{B_\phi^2}{4\pi\rho} \right\rangle \frac{\partial \ln \sqrt{A}}{\partial x} dx$ , and  $\Delta_g^r = -v_{\text{esc}\star}^2 \left( 1 - \frac{r_*}{r} \right)$ , where  $v_{\text{esc}\star} = \sqrt{2GM_*/r_*}$  is the escape velocity on the stellar surface.

Another integral of equation describes the energy flux conservation.

$$A(F_A + F(v_x) + F_g + F_c + F_{\text{rad}}) = L_{\text{total}} = \text{const}. \quad (3.2)$$

where  $F_A = -B_x \langle B_\phi v_\phi \rangle / (4\pi)$  is Poynting flux by the magnetic tension (Alfvén wave energy flux),  $F_g = -\langle \rho v_x \rangle GM_*/r$  is the gravitational energy flux, and  $F_{\text{rad}} = \frac{1}{A} \int_\infty^x A \langle Q_{\text{rad}} \rangle dx'$  is the energy flux representing the radiative energy loss.  $F(v_x)$  is the sum of enthalpy flux  $F_{\text{ent}}$ , kinetic energy flux  $F_{\text{kin}}$  and the Poynting flux advected by the stellar wind:  $F_{\text{ent}} = \gamma \langle p v_x \rangle / (\gamma - 1)$ ,  $F_{\text{kin}} = \langle \rho v^2 v_x \rangle / 2$ , and  $F(v_x) = F_{\text{ent}} + F_{\text{kin}} + \langle B_\phi^2 v_x \rangle / (4\pi)$ .

Equation (3.1) and (3.2) are confirmed in Figure 3.3(a) and (b), which show the simulation result of stellar wind for the M3.5 dwarf. In Figure 3.3(a), the black solid line corresponds to  $\Delta_p^r + \Delta_g^r + \Delta_{p_B}^r + \Delta_t^r + \Delta_c^r$ , which agrees well with  $v_x^2$  (thick gray line) as indicated by Equation (3.1). It is most remarkable in Figure 3.3(a) that the stellar wind is mainly driven by the plasma pressure gradient (red solid line). In particular, the slow shocks excited by the nonlinear process of Alfvén waves greatly contribute to this stellar wind acceleration, which will be explained in Sakaue & Shibata (to be submitted) in more detail. The magnetic pressure gradient (green line) contributes to supporting the stellar atmosphere and driving the stellar wind within  $r \lesssim 10r_*$ , but not involved in the further acceleration of stellar wind beyond the distance where the

Alfvén wave amplitude (orange line) reaches a maximum. The magnetic tension force decelerates the stellar wind against the acceleration by the centrifugal force (blue line). In Figure 3.3(b), the energy fluxes are normalized by  $F_{\text{mass}}GM_{\star}/r_{\star}$ , where  $F_{\text{mass}}$  is the mass flux and  $F_{\text{mass}}GM_{\star}/r_{\star} \approx 5 \times 10^3 r_{\star}^2 / (fr^2)$  erg cm<sup>-2</sup> s<sup>-1</sup>. It is confirmed that  $F_A$ ,  $F_g$ , and  $F_c$  determine the energy balance at the coronal height  $r - r_{\star} \sim 0.1r_{\star}$ , while in the distance ( $\gtrsim 10r_{\star}$ ), the kinetic energy flux of the stellar wind ( $F_{\text{kin}}$ ) dominates the total energy flux. By defining  $L_{A,\text{co}}$ ,  $L_{g,\text{co}}$ ,  $L_{c,\text{co}}$  as the energy luminosities  $F_A A$ ,  $F_g A$ ,  $F_c A$  at  $r = 1.1r_{\star}$  and  $L_{\text{kin,wind}}$  as  $F_{\text{kin}} A$  at  $r = 100r_{\star}$ , the energy conservation along the magnetic flux tube is approximately expressed as

$$L_{A,\text{co}} \approx L_{\text{kin,wind}} - L_{g,\text{co}} - L_{c,\text{co}}. \quad (3.3)$$

The subscript <sub>co</sub> represents the physical quantities at  $r = r_{\text{co}} = 1.1r_{\star}$ . The above relation shows that the Alfvén wave energy flux is converted to the wind’s energy loss  $L_{\text{kin,wind}} - L_{g,\text{co}}$  and the coronal heating loss  $-L_{c,\text{co}}$ . Note that  $L_{\text{kin,wind}} - L_{g,\text{co}} = \dot{M}(v_{\text{wind}}^2 + v_{\text{esc}\star}^2)/2$ , where  $v_{\text{wind}} = v_x(r = 100r_{\star})$  is the wind velocity and  $\dot{M} = \rho v_x A$  is the mass-loss rate.

### 3.4 Stellar Coronae and Winds from the Sun to M Dwarfs

Numerical parameter surveys about the Sun and M dwarfs reveal the diversity of stellar wind velocity ( $v_{\text{wind}}$ ) and coronal temperature ( $T_{\text{co}}$ ). Figure 3.4 illustrates the general trends of such characteristics of stellar atmospheres and winds. In Figure 3.4(a),  $v_{\text{wind}}$  are plotted as a function of the maximum amplitude of Alfvén wave in the stellar wind ( $v_{\phi\text{max}}$ ). The tight correlation between them is accounted for, because  $v_{\phi\text{max}}$  well represents the strength of slow shocks that drive the stellar winds. The Alfvén wave tends to be more amplified in the stellar wind when  $T_{\text{co}}$  is cooler (Figure 3.4(b)). Figure 3.4(c) shows that  $T_{\text{co}}$  increases with the transmitted Poynting flux into the corona ( $F_{A,\text{co}}$ ), but M dwarfs’  $T_{\text{co}}$  are systematically cooler than that of the Sun for a given  $F_{A,\text{co}}$ . Finally, it is confirmed that the wind’s mass-loss rates ( $\dot{M}$ ) are well correlated with the energy luminosity of the Alfvén wave ( $L_{A,\text{co}}$ ), as shown in Figure 3.4(d).

### 3.5 Semi-empirical method to predict the characteristics of stellar atmosphere and wind

In order to comprehend the physical mechanisms causing the relationships presented in Figure 3.4, we developed a semi-empirical method to calculate  $v_{\text{wind}}$ ,  $v_{\phi\text{max}}$ , and  $T_{\text{co}}$  as functions of given effective temperature ( $T_{\text{eff}}$ ) and Alfvén wave luminosity on the stellar photosphere ( $L_{A,\text{ph}}$ ). Their derivation of them is briefly summarized in Appendix 3.B and will be described in Sakaue & Shibata (to be submitted). The solid lines in Figure 3.4 are the prediction curves of our semi-empirical method. As shown in Figure 3.4, the positive or negative correlations among the physical quantities are correctly reproduced by our method, although the simulation results remain scattered around the prediction curves within a factor of  $\sim 2$ . This means that the following scenario, which is employed in our semi-empirical method, can account for the relationships shown in Figure 3.4, in both a qualitative and somewhat quantitative manner.

According to our semi-empirical method, the thinner atmosphere of the M dwarf is characterized by an increase in the temperature gradient in the corona ( $(\text{grad}T)_{\text{co}}$ ) for a given  $T_{\text{co}}$ . The larger  $(\text{grad}T)_{\text{co}}$  is, the cooler  $T_{\text{co}}$  is for a given  $L_{A,\text{ph}}$ , so that the energy balance is satisfied between Poynting flux and heat conduction flux. The cooler  $T_{\text{co}}$  of the M dwarf results in lower plasma  $\beta$  for the stellar wind, in which the amplification of the Alfvén wave is promoted. The larger amplitude of the Alfvén wave is associated with the stronger slow shocks, which contribute to the faster stellar wind of the M dwarf. The faster  $v_{\text{wind}}$  and much smaller surface area of the M dwarf lead to a much smaller  $\dot{M}$  of the M dwarf’s wind.

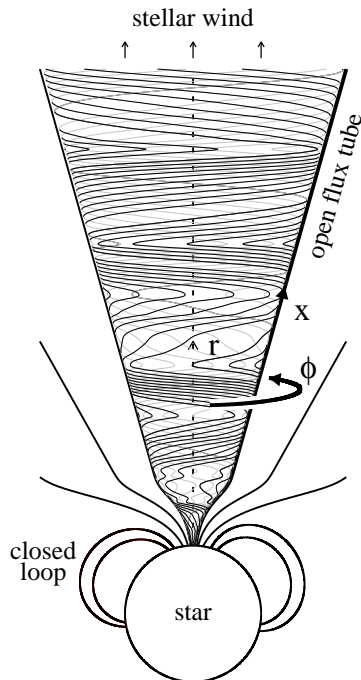


Figure 3.1: Schematic image of axisymmetric magnetic flux tube, the surface of which is defined by the poloidal  $x$  and toroidal  $\phi$  axes. The winding thin lines represent the magnetic field lines, which illustrate the nonlinear propagation of the Alfvén wave.

By using the established semi-empirical method, we can predict the general trends of  $v_{\text{wind}}$ ,  $T_{\text{co}}$ , and  $\dot{M}$ , with respect to  $T_{\text{eff}}$  and  $L_{\text{A,ph}}$ , as illustrated in Figure 3.5 (see Appendix 3.B). The open circles in this figure represent the samples of our parameter survey discussed in this Letter, about each of which several chromospheric magnetic field strengths are tested. The thick dashed line corresponds to the fiducial  $L_{\text{A,ph}}$  as a function of  $T_{\text{eff}}$ , which is calculated from the photospheric magnetic field, filling factor of open magnetic flux, and the velocity fluctuation of the convective motion. The thick dashed-dotted line corresponds to the largest  $L_{\text{A,ph}}$  obtained by assuming that the convective velocity reaches the sound speed on the photosphere. The thin dashed line represents  $L_{\text{A,ph}}$  as a function of  $T_{\text{eff}}$  which results in  $v_{\text{wind}} = v_{\text{esc}\star}$ . Along the thick dashed line, it is seen that stellar wind velocity ( $v_{\text{wind}}$ ) and coronal temperature ( $T_{\text{co}}$ ) are faster and cooler with decreasing  $T_{\text{eff}}$ , and that the mass-loss rate ( $\dot{M}$ ) of M-dwarfs' winds are much smaller than the solar wind's value.

### 3.6 Discussion

Our wind's mass-loss rates of M dwarfs are typically smaller than those reported by the previous global 3D stellar wind modelings using AWSoM. The  $\dot{M}$  of an M8 type star in this study is no more than  $6.9 \times 10^{-17} M_{\odot} \text{ yr}^{-1}$ , while Garraffo et al. (2017) and Dong et al. (2018) showed  $3 \times 10^{-14} M_{\odot} \text{ yr}^{-1}$  and  $4.1 \times 10^{-15} M_{\odot} \text{ yr}^{-1}$  for TRAPPIST-1 (M8), respectively. The  $\dot{M}$  of Proxima Centauri (M5.5) by Garraffo et al. (2016) and EV Lac (M3.5) by Cohen et al. (2014) are  $1.5 \times 10^{-14} M_{\odot} \text{ yr}^{-1}$  and  $3 \times 10^{-14} M_{\odot} \text{ yr}^{-1}$ , respectively, which are 10–100 times higher than reproduced in our simulation. These much larger mass-loss rates probably originate in their inner boundary conditions, corresponding to the top of the stellar chromosphere. In particular, our

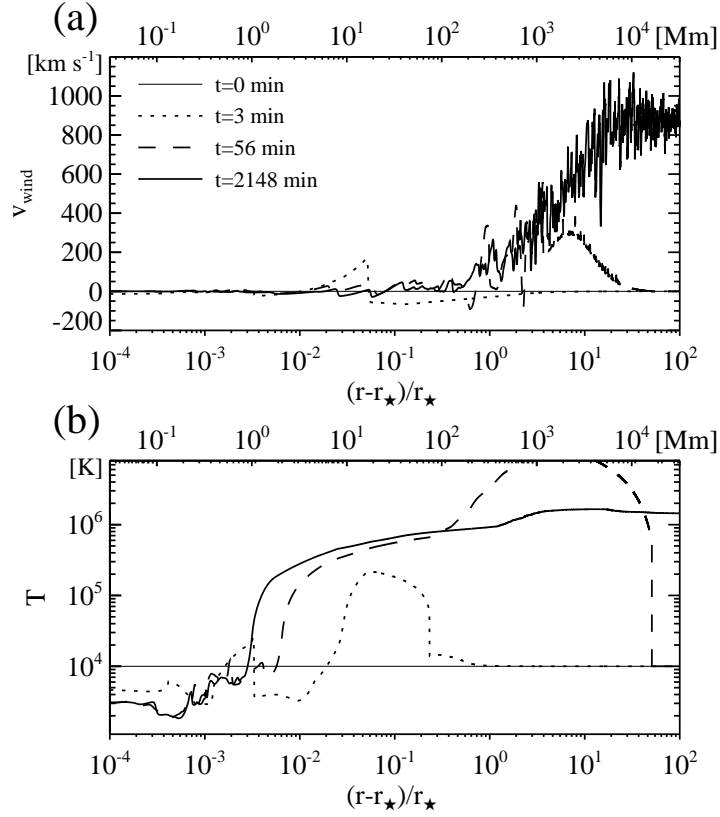


Figure 3.2: Temporal variations of the stellar wind velocity (panel (a)) and temperature (panel (b)) in the case of the M3.5 dwarf ( $r_* = 0.46r_\odot$ ). The stellar wind velocity reaches around  $900 \text{ km s}^{-1}$ . The transition layer appears in the temperature profile, dividing the lower-temperature chromosphere and 10 MK corona.

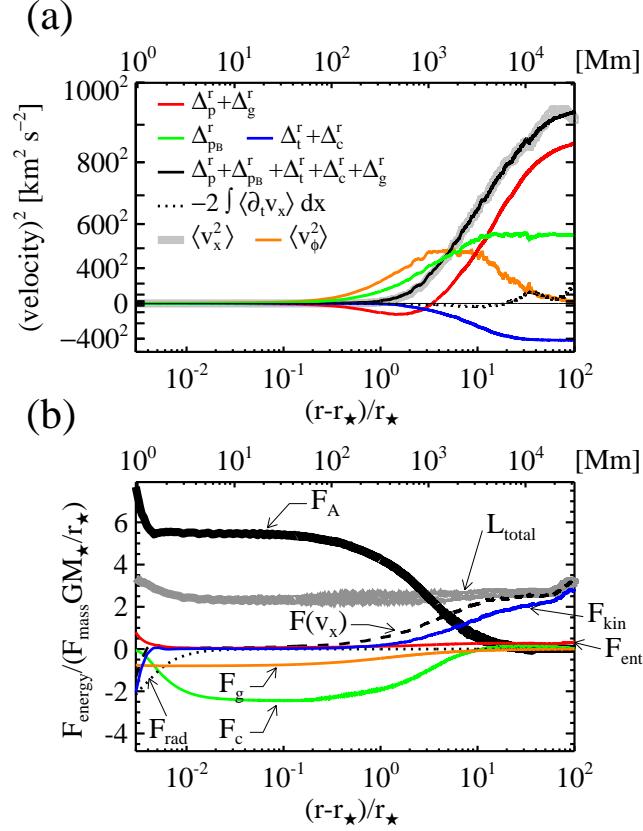


Figure 3.3: Momentum and energy conservations in the stellar wind of the M3.5 dwarf. In panel (a), the profile of  $v_x^2$  (thick gray line) is compared to the contributions by magnetic pressure acceleration  $\Delta_{pB}^r$  (green line), sum of plasma pressure  $\Delta_p^r$  and gravitational acceleration  $\Delta_g^r$  (red line), and sum of centrifugal force  $\Delta_c^r$  and magnetic tension force  $\Delta_t^r$ . The orange line shows the profile of the square amplitude of the Alfvén wave. Panel (b) shows the energy fluxes normalized by  $F_{\text{mass}}GM_*/r_*$ , where  $F_{\text{mass}}$  is the mass flux and  $F_{\text{mass}}GM_*/r_* \approx 5 \times 10^3 r_*^2 / (fr^2)$  erg cm $^{-2}$  s $^{-1}$ .  $F_A$ ,  $F_{\text{kin}}$ ,  $F_{\text{ent}}$ ,  $F_g$ ,  $F_{\text{rad}}$ ,  $F_c$ , and  $F(v_x)$  are Alfvén wave energy flux, kinetic energy flux, enthalpy flux, gravitational energy flux, heat conduction flux, and the sum of enthalpy flux, kinetic energy flux, and Poynting flux advected with the stellar wind, respectively.  $L_{\text{total}}$  is the integral constant in Equation (3.2).

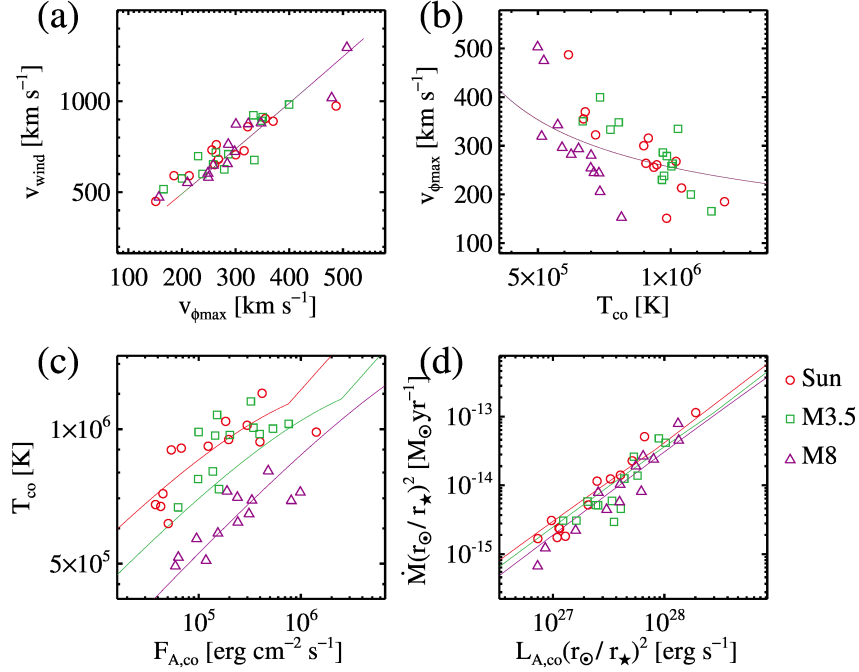


Figure 3.4: Characteristics of stellar atmospheres and winds obtained from the numerical parameter survey. The symbols represent the simulation results. The parameter survey for each star is carried out for the velocity amplitude on the photosphere (within  $(0.04 - 0.6) \times$  adiabatic sound speeds on the photosphere) and the chromospheric magnetic field strength (within  $(0.002 - 0.05) \times$  photospheric magnetic field strengths). The solid lines correspond to the prediction curves of our semi-empirical method. Panel (a): stellar wind velocity ( $v_{\text{wind}}$ ) vs. the maximum amplitude of the Alfvén wave in the stellar wind ( $v_{\phi \text{max}}$ ). Panel (b):  $v_{\phi \text{max}}$  vs. the coronal temperature ( $T_{\text{co}}$ ). Panel (c):  $T_{\text{co}}$  vs. the transmitted Poynting flux into the corona ( $F_{\text{A,co}}$ ). Panel (d): Alfvén wave luminosity in the corona ( $L_{\text{A,co}}$ ) vs. stellar wind's mass-loss rate ( $\dot{M}$ ).

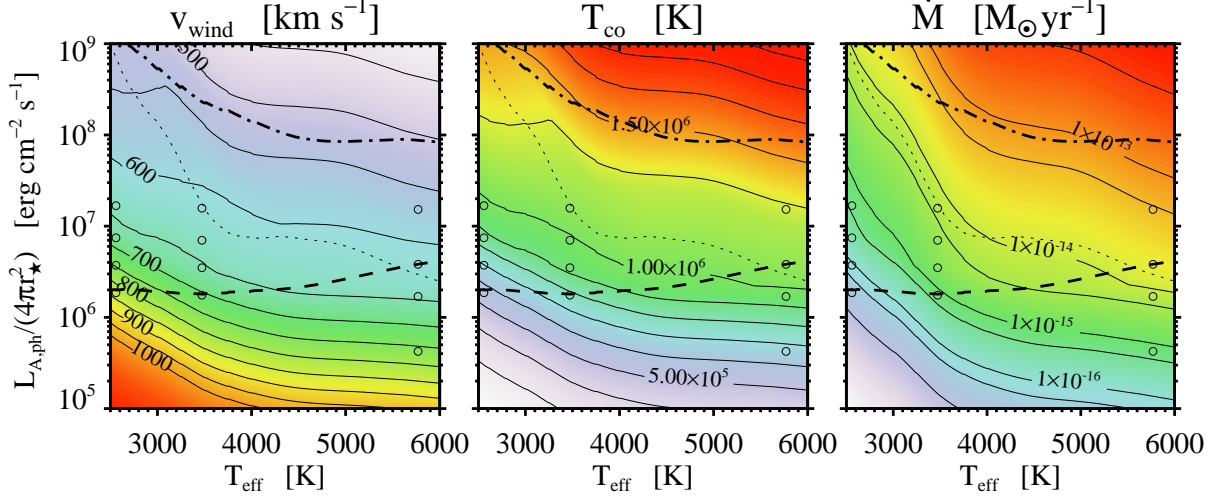


Figure 3.5: General trends of stellar wind velocity ( $v_{\text{wind}}$ ), coronal temperature ( $T_{\text{co}}$ ), and wind’s mass-loss rate ( $\dot{M}$ ), with respect to the effective temperature ( $T_{\text{eff}}$ ) and Alfvén wave luminosity on the photosphere ( $L_{\text{A,ph}}$ ), which is predicted by our semi-empirical method. The open circles in this figure represent part of the samples in our parameter survey. The thick dashed line corresponds to the fiducial  $L_{\text{A,ph}}$  as a function of  $T_{\text{eff}}$ . The thick dashed-dotted line corresponds to the largest  $L_{\text{A,ph}}$  obtained by assuming that the convective velocity reaches the sound speed on the photosphere. The thin dashed line represents  $L_{\text{A,ph}}$  as a function of  $T_{\text{eff}}$  which results in  $v_{\text{wind}} = v_{\text{esc}\star}$ .

simulation does not validate their estimation of Alfvén wave energy injection, which is sometimes based on the widely used assumption of the constant “Poynting-flux-to-field ratio” (Sokolov et al., 2013). It is impossible for the above 3D modelings to reproduce our results because they are unable to consider the Alfvén wave dissipation and reflection from the stellar photosphere to the top of the chromosphere more self-consistently with the present computational resources.

Cranmer and Saar (2011) estimated that the  $\dot{M}$  of EV Lac (M3.5) is three orders of magnitude smaller than our simulation results for an M3.5 type star. This is because they assumed much smaller Poynting flux on the photosphere compared to our simulation. The scaling law for  $\dot{M}$  proposed by Suzuki (2018) was also predicted to be 10 – 100 times smaller than our estimation. They performed numerical simulations that are similar to our study, but the low-mass stars with  $M_{\star} \geq 0.6M_{\odot}$  are considered. According to their analysis, Alfvén wave transmissivity into the corona strongly depends on the stellar effective temperature ( $\propto T_{\text{eff}}^{13/2}$ ), which possibly leads to the underestimation of  $\dot{M}$  for cool dwarfs. Finally, we point out that the assumption of  $v_{\text{wind}} = v_{\text{esc}\star}$  used in both Cranmer and Saar (2011) and Suzuki (2018) misleadingly implies that  $\dot{M}$  depends on  $v_{\text{esc}\star}$ .

Observational measurements of an M dwarf’s stellar wind are still very challenging. In order to quantify the stellar wind’s properties observationally, Wood et al. (2005) investigated the absorption signatures in stellar Ly $\alpha$  spectra, leading to the estimation of  $\dot{M} \sim 2 \times 10^{-14} M_{\odot} \text{yr}^{-1}$  for EV Lac (M3.5). They also suggested an upper limit of Proxima Centauri’s  $\dot{M} \sim 4 \times 10^{-15} M_{\odot} \text{yr}^{-1}$ . Bourrier et al. (2016) and Vidotto and Bourrier (2017) deduced  $\dot{M}$  of GJ 436 (M2.5) to be around  $(0.45 - 2.5) \times 10^{-15} M_{\odot} \text{yr}^{-1}$  by analyzing the transmission spectra of Ly $\alpha$  of GJ 436 b (a warm Neptune). While the observed  $\dot{M}$  of GJ 436 and the upper limit on  $\dot{M}$  of Proxima Centauri is not inconsistent with our results, the observed  $\dot{M}$  of EV Lac is much higher than the simulated value. Cranmer and Saar (2011) argued that the coronal mass ejection (CME)

is possibly related to the observed high mass-loss rate of EV Lac. To clarify what causes the discrepancy between the observed and simulated  $\dot{M}$ , further self-consistent modeling is needed for the stellar wind and astrosphere.

## Appendix 3.A Basic Equations

The basic equations in the axial symmetric magnetic flux tube are written as follows:

$$\frac{\partial \rho}{\partial t} + \frac{1}{A} \frac{\partial}{\partial x} (\rho v_x A) = 0, \quad (3.4)$$

$$\begin{aligned} & \frac{\partial}{\partial t} \left( \frac{p}{\gamma-1} + \frac{1}{2} \rho v^2 + \frac{B^2}{8\pi} \right) \\ & + \frac{1}{A} \frac{\partial}{\partial x} \left[ A \left\{ \left( \frac{\gamma p}{\gamma-1} + \frac{\rho v^2}{2} + \frac{B_\phi^2}{4\pi} \right) v_x - \frac{B_x}{4\pi} (B_\phi v_\phi) \right\} \right] \\ & = \rho v_x \frac{\partial}{\partial x} \left( \frac{GM_\star}{r} \right) - \frac{1}{A} \frac{\partial}{\partial x} (AF_c) - Q_{\text{rad}}, \end{aligned} \quad (3.5)$$

$$\begin{aligned} & \frac{\partial(\rho v_x)}{\partial t} + \frac{\partial p}{\partial x} + \frac{1}{A} \frac{\partial}{\partial x} \left\{ \left( \rho v_x^2 + \frac{B_\phi^2}{8\pi} \right) A \right\} \\ & - \rho v_\phi^2 \frac{\partial \ln \sqrt{A}}{\partial x} - \rho \frac{\partial}{\partial x} \left( \frac{GM_\star}{r} \right) = 0, \end{aligned} \quad (3.6)$$

$$\frac{\partial(\rho v_\phi)}{\partial t} + \frac{1}{A\sqrt{A}} \frac{\partial}{\partial x} \left\{ A\sqrt{A} \left( \rho v_x v_\phi - \frac{B_x B_\phi}{4\pi} \right) \right\} = 0, \quad (3.7)$$

$$\frac{\partial B_\phi}{\partial t} + \frac{1}{\sqrt{A}} \frac{\partial}{\partial x} \left( \sqrt{A} (v_x B_\phi - v_\phi B_x) \right) = 0, \quad (3.8)$$

$$\frac{dx}{dr} = \sqrt{1 + \left( \frac{d\sqrt{A}}{dr} \right)^2}. \quad (3.9)$$

Here,  $\gamma$  represents the specific heat ratio and is set to 5/3 in this study.  $F_c$  and  $Q_{\text{rad}}$  are the heat conduction flux and radiative cooling term, respectively.  $r$  is the distance from the center of the Sun.  $A$  is the cross section of the flux tube (i.e.,  $B_x A = \text{const.}$ ), and is related to  $r$  through the filling factor  $f$  as  $A(r) = 4\pi r^2 f(r)$ .  $f$  determines the geometry of the flux tube. The functions for  $F_c$ ,  $Q_{\text{rad}}$ , and  $f(r)$  are similar to those used in [Sakaue and Shibata \(2020\)](#).

## Appendix 3.B Semi-empirical Method for Stellar Coronae and Winds

The derivation of our semi-empirical method is briefly summarized in this Appendix. More detailed discussion will appear in our subsequent paper (Sakaue & Shibata, to be submitted).

In section 3.3, the stellar wind velocity ( $v_{\text{wind}}$ ) is determined according to the integral of equation of motion (Equation 3.1).

$$v_{\text{wind}}^2 = \Delta_p + \Delta_{p_B} + \Delta_c + \Delta_t + \Delta_g, \quad (3.10)$$

where  $v_{\text{wind}}$  is the stellar wind velocity at  $r = 100r_*$ , and  $\Delta_p = -2 \int_{r_*}^{100r_*} \frac{1}{\rho} \frac{\partial p}{\partial x} dx$ ,  $\Delta_{p_B} = -2 \int_{r_*}^{100r_*} \frac{1}{\rho} \frac{\partial}{\partial x} \left( \frac{B_\phi^2}{8\pi} \right) dx$ ,  $\Delta_c = 2 \int_{r_*}^{100r_*} v_\phi^2 \frac{\partial \ln \sqrt{A}}{\partial x} dx$ ,  $\Delta_t = -2 \int_{r_*}^{100r_*} \frac{B_\phi^2}{4\pi\rho} \frac{\partial \ln \sqrt{A}}{\partial x} dx$ , and  $\Delta_g = -v_{\text{esc}\star}^2 \left( 1 - \frac{1}{100} \right)$ . They are characterized by the maximum amplitude of Alfvén wave in the stellar wind ( $v_{\phi \text{max}}$ ) as follows:

$$\Delta_p + \Delta_g = a_{1,1} \tilde{v}_{\phi \text{max}}^{k_{1,1}}, \quad \Delta_c = a_{1,2} \tilde{v}_{\phi \text{max}}^{k_{1,2}}, \quad \Delta_t = -a_{1,3} \tilde{v}_{\phi \text{max}}^{k_{1,3}}, \quad \Delta_{p_B} = a_{1,4} |\tilde{\Delta}_c + \tilde{\Delta}_t|^{k_{1,4}}. \quad (3.11)$$

where  $\tilde{v}_{\phi \text{max}} = v_{\phi \text{max}} / (300 \text{ km s}^{-1})$ ,  $\tilde{\Delta}_c = \Delta_c / (319^2 \text{ (km s}^{-1})^2)$ ,  $\tilde{\Delta}_t = \Delta_t / (319^2 \text{ (km s}^{-1})^2)$ . The coefficients ( $a_{1,1}$ ,  $a_{1,2}$ ,  $a_{1,3}$ ,  $a_{1,4}$ ) and power-law indices ( $k_{1,1}$ ,  $k_{1,2}$ ,  $k_{1,3}$ ,  $k_{1,4}$ ) are determined based on our simulation results

$$a_{1,1} = 653^2, \quad a_{1,2} = 585^2, \quad a_{1,3} = 666^2, \quad a_{1,4} = 472^2,$$

in unit of  $(\text{km s}^{-1})^2$ .

$$k_{1,1} = 2.31, \quad k_{1,2} = 2.04, \quad k_{1,3} = 2.12, \quad k_{1,4} = 0.682.$$

$v_{\phi \text{max}}$  is negatively correlated with the plasma  $\beta$  at the position where Alfvén wave amplitude reaches the maximum ( $\beta_{\phi \text{max}}$ ).

$$v_{\phi \text{max}} = a_2 \beta_{\phi \text{max}}^{-k_2}, \quad (3.12)$$

where  $a_2 = 286 \text{ km s}^{-1}$  and  $k_2 = 0.171$ .

$\beta_{\phi \text{max}}$  is determined by the coronal temperature  $T_{\text{co}}$  and  $v_{\text{wind}}$ .

$$\beta_{\phi \text{max}} = a_3 \left( \frac{\tilde{T}_{\text{co}}}{\tilde{v}_{\text{wind}}} \right)^{k_3}, \quad (3.13)$$

where  $\tilde{T}_{\text{co}} = T_{\text{co}} / (10^6 \text{ K})$ ,  $\tilde{v}_{\text{wind}} = v_{\text{wind}} / (600 \text{ km s}^{-1})$ .  $a_3 = 2.09 \times 10^{-2}$  and  $k_3 = 1.85$ .

The coronal temperature ( $T_{\text{co}}$ ) is determined by the balance between heat conduction flux and the transmitted Poynting flux into the corona, according to the energy conservation law (Equation (3.3)). This is similar to the analytical models of quiescent and flaring coronal loops (Rosner et al., 1978; Yokoyama and Shibata, 1998). Hereafter, we discuss the following equation, which is obtained by dividing the both sides of Equation (3.3) with  $L_{A,\text{co}}$ .

$$\alpha_{c/A} = 1 - \alpha_{\text{wind}/A} (1 + v_{\text{esc}\star}^2 / v_{\text{wind}}^2), \quad (3.14)$$

where  $\alpha_{c/A}$  and  $\alpha_{\text{wind}/A}$  represent the energy conversion efficiency from  $L_{A,\text{co}}$  to  $L_{c,\text{co}}$  and  $L_{\text{kin},\text{wind}}$  (i.e.,  $L_{c,\text{co}} = -\alpha_{c/A} L_{A,\text{co}}$  and  $L_{\text{kin},\text{wind}} = \alpha_{\text{wind}/A} L_{A,\text{co}}$ ). Note that when  $v_{\text{wind}} < v_{\text{esc}\star}$ ,  $\alpha_{c/A}$  is often quenched to zero, which means that the approximation for Equations (3.3) and (3.14) become invalid. To avoid this problem, we assumed the monotonic increase in  $L_{c,\text{co}}$  with  $L_{A,\text{co}}$ . i.e.,  $\partial \ln \alpha_{c/A} / \partial \ln L_{A,\text{co}} > -1$ .

We also confirmed that the coefficient  $\alpha_{\text{wind}/A}$  is almost invariant in our parameter survey about the stars, chromospheric magnetic field strengths, and energy inputs from the photosphere, namely  $\alpha_{\text{wind}/A} = 0.442 \pm 0.166$ . Therefore,  $\alpha_{\text{wind}/A}$  is assumed to be constant in this study. It should be noted that, however,  $\alpha_{\text{wind}/A}$  possibly depends on the filling factor of open flux tube ( $f_{\text{ph}}$ ), which is beyond our present parameter survey.

By defining the spatial scale of expanding magnetic flux tube ( $l_B$ ) as below, the coronal temperature ( $T_{\text{co}}$ ) is estimated as Equation (3.16).

$$l_B = \int_1^{\bar{B}/B_{x,\text{co}}} \left| \frac{d \ln B_x}{dx} \right|^{-1} d \left( \frac{B_x}{B_{x,\text{co}}} \right) \quad (3.15)$$

$$T_{\text{co}} = a_4 \left[ \left\{ 1 - \alpha_{\text{wind/A}} \left( 1 + \frac{v_{\text{esc}\star}^2}{v_{\text{wind}}^2} \right) \right\} \tilde{F}_{A,\text{co}} \tilde{l}_B \right]^{k_4}, \quad (3.16)$$

where  $\bar{B}$  and  $B_{x,\text{co}}$  are the magnetic field strengths in the chromosphere and corona.  $\tilde{F}_{A,\text{co}} = F_{A,\text{co}}/(10^5 \text{ erg cm}^{-2} \text{ s}^{-1})$ ,  $\tilde{l}_B = l_B/r_{\odot}$ .  $a_4 = 1.62 \times 10^6 \text{ K}$ ,  $k_4 = 0.256$ . Note that  $l_B$  is determined only by the assumed geometry of magnetic flux tube.

Finally,  $L_{A,\text{co}}$  should be expressed as a product of  $L_{A,\text{ph}}$  which is the Alfvén wave luminosity on the stellar photosphere and the transmissivity of Alfvén wave from the photosphere to corona ( $\alpha_{\text{co/ph}}$ , i.e.,  $L_{A,\text{co}} = \alpha_{\text{co/ph}} L_{A,\text{ph}}$ ). The dissipation and reflection of Alfvén wave in the stellar chromosphere could reduce  $\alpha_{\text{co/ph}}$ .

$\alpha_{\text{co/ph}}$  is well described by the Alfvén travel time from the photosphere to the corona ( $\tau_{A,\text{co}}$ ), especially the normalized one by the typical wave frequency of Alfvén wave ( $\nu_A$ ). We interpreted  $\nu_A$  with the acoustic cutoff frequency of stellar photosphere ( $\nu_{\text{ac}}$ ), and found the following:

$$\alpha_{\text{co/ph}} = a_{5,1} (\tau_{A,\text{co}} \nu_{\text{ac}} / a_{5,2})^{k_5}, \quad (3.17)$$

where  $a_{5,1} = 2.41 \times 10^{-2}$  and  $a_{5,2} = 1.04$ .  $k_5 = 1.25$  when  $\tau_{A,\text{co}} \nu_{\text{ac}} < 1.04$ , and otherwise,  $k_5 = -1.10$ .  $\tau_{A,\text{co}} \nu_{\text{ac}}$  is empirically expressed as a function of  $g_{\star}$ , chromospheric magnetic field strength ( $\bar{B}$ ), and velocity amplitude on the photosphere ( $v_{\text{ph}}$ ):

$$\tau_{A,\text{co}} \nu_{\text{ac}} = a_6 \tilde{g}_{\star}^{k_{6,1}} \left( \frac{\bar{B}}{B_{\text{ph}}} \right)^{-k_{6,2}} \left( \frac{v_{\text{ph}}}{c_{s,\text{ph}}} \right)^{k_{6,3}}, \quad (3.18)$$

where  $c_{s,\text{ph}}$  and  $B_{\text{ph}}$  are the adiabatic sound speed and magnetic field strength on the photosphere.  $a_6 = 0.921$ ,  $k_{6,1} = 0.240$ ,  $k_{6,2} = 0.408$ , and  $k_{6,3} = 0.697$ .

Based on Equations (3.15)–(3.18),  $T_{\text{co}}$  is obtained as a function of  $v_{\text{wind}}$  and  $L_{A,\text{ph}}$  (or  $v_{\text{ph}}$ ) by specifying the basic parameters ( $g_{\star}$ ,  $B_{\text{ph}}$ ,  $\bar{B}$ ,  $c_{s,\text{ph}}$ ,  $v_{\text{esc}\star}$ ,  $\alpha_{\text{wind/A}}$ ,  $l_B$ ). These parameters can be related to the stellar effective temperature  $T_{\text{eff}}$  by limiting our discussion to the main-sequence stars' atmospheres and winds. On the other hand, Equations (3.10)–(3.13) show that  $v_{\text{wind}}$  should be determined implicitly when  $T_{\text{co}}$  is given. By using some iterative method, therefore,  $T_{\text{co}}$  and  $v_{\text{wind}}$  are calculated for given  $L_{A,\text{ph}}$  and  $T_{\text{eff}}$ . From the obtained  $v_{\text{wind}}$  and the definition of  $L_{\text{kin,wind}}$ , the mass-loss rate of stellar wind ( $\dot{M}$ ) is expressed as follows:

$$\dot{M} = 2\alpha_{\text{wind/A}} \alpha_{\text{co/ph}} \frac{L_{A,\text{ph}}}{v_{\text{wind}}^2} \quad (3.19)$$

Sakaue & Shibata (2021) will explain the derivation of the above coefficients ( $a_{1,1}$ ,  $a_{1,2}$ ,  $a_{1,3}$ ,  $a_{1,4}$ ,  $a_2$ ,  $a_3$ ,  $a_4$ ,  $a_{5,1}$ ,  $a_{5,2}$ ,  $a_6$ ) and power-law indices ( $k_{1,1}$ ,  $k_{1,2}$ ,  $k_{1,3}$ ,  $k_{1,4}$ ,  $k_2$ ,  $k_3$ ,  $k_4$ ,  $k_5$ ,  $k_{6,1}$ ,  $k_{6,2}$ ,  $k_{6,3}$ ) with more simulation results for some M dwarfs (M0, M5, M5.5).

## Bibliography

Alvarado-Gómez, J. D., J. J. Drake, F. Frascchetti, C. Garraffo, O. Cohen, C. Vocks, K. Poppenhäger, S. P. Moschou, R. K. Yadav, and I. Manchester, Ward B.  
2020. Tuning the Exospace Weather Radio for Stellar Coronal Mass Ejections. *ApJ*, 895(1):47.

- Bourrier, V., A. Lecavelier des Etangs, D. Ehrenreich, Y. A. Tanaka, and A. A. Vidotto  
 2016. An evaporating planet in the wind: stellar wind interactions with the radiatively braked exosphere of GJ 436 b. *A&A*, 591:A121.
- Cohen, O., J. J. Drake, A. Gloer, C. Garraffo, K. Poppenhaeager, J. M. Bell, A. J. Ridley, and T. I. Gombosi  
 2014. Magnetospheric Structure and Atmospheric Joule Heating of Habitable Planets Orbiting M-dwarf Stars. *ApJ*, 790(1):57.
- Cranmer, S. R. and S. H. Saar  
 2011. Testing a Predictive Theoretical Model for the Mass Loss Rates of Cool Stars. *ApJ*, 741(1):54.
- Dong, C., M. Jin, M. Lingam, V. S. Airapetian, Y. Ma, and B. van der Holst  
 2018. Atmospheric escape from the TRAPPIST-1 planets and implications for habitability. *Proceedings of the National Academy of Science*, 115(2):260–265.
- Freedman, R. S., J. Lustig-Yaeger, J. J. Fortney, R. E. Lupu, M. S. Marley, and K. Lodders  
 2014. Gaseous Mean Opacities for Giant Planet and Ultracool Dwarf Atmospheres over a Range of Metallicities and Temperatures. *ApJS*, 214(2):25.
- Garraffo, C., J. J. Drake, and O. Cohen  
 2016. The Space Weather of Proxima Centauri b. *ApJL*, 833(1):L4.
- Garraffo, C., J. J. Drake, O. Cohen, J. D. Alvarado-Gómez, and S. P. Moschou  
 2017. The Threatening Magnetic and Plasma Environment of the TRAPPIST-1 Planets. *ApJL*, 843(2):L33.
- Gillon, M., E. Jehin, S. M. Lederer, L. Delrez, J. de Wit, A. Burdanov, V. Van Grootel, A. J. Burgasser, A. H. M. J. Triaud, C. Opitom, B.-O. Demory, D. K. Sahu, D. Bardalez Gagliuffi, P. Magain, and D. Queloz  
 2016. Temperate Earth-sized planets transiting a nearby ultracool dwarf star. *Nature*, 533(7602):221–224.
- Hollweg, J. V., S. Jackson, and D. Galloway  
 1982. Alfvén Waves in the Solar Atmospheres - Part Three - Nonlinear Waves on Open Flux Tubes. *Sol. Phys.*, 75(1-2):35–61.
- Khodachenko, M. L., I. Ribas, H. Lammer, J.-M. Grießmeier, M. Leitner, F. Selsis, C. Eiroa, A. Hanslmeier, H. K. Biernat, C. J. Farrugia, and H. O. Rucker  
 2007. Coronal Mass Ejection (CME) Activity of Low Mass M Stars as An Important Factor for The Habitability of Terrestrial Exoplanets. I. CME Impact on Expected Magnetospheres of Earth-Like Exoplanets in Close-In Habitable Zones. *Astrobiology*, 7(1):167–184.
- Kudoh, T. and K. Shibata  
 1999. Alfvén Wave Model of Spicules and Coronal Heating. *ApJ*, 514(1):493–505.
- Lammer, H., H. I. M. Lichtenegger, Y. N. Kulikov, J.-M. Grießmeier, N. Terada, N. V. Erkaev, H. K. Biernat, M. L. Khodachenko, I. Ribas, T. Penz, and F. Selsis  
 2007. Coronal Mass Ejection (CME) Activity of Low Mass M Stars as An Important Factor for The Habitability of Terrestrial Exoplanets. II. CME-Induced Ion Pick Up of Earth-like Exoplanets in Close-In Habitable Zones. *Astrobiology*, 7(1):185–207.
- Linsky, J.  
 2019. *Host Stars and their Effects on Exoplanet Atmospheres*, volume 955. Gewerbestr: Springer Nature Switzerland AG.

Ludwig, H. G., F. Allard, and P. H. Hauschildt

2002. Numerical simulations of surface convection in a late M-dwarf. *A&A*, 395:99–115.

Ludwig, H.-G., B. Freytag, and M. Steffen

1999. A calibration of the mixing-length for solar-type stars based on hydrodynamical simulations. I. Methodical aspects and results for solar metallicity. *A&A*, 346:111–124.

Magic, Z., A. Weiss, and M. Asplund

2015. The Stagger-grid: A grid of 3D stellar atmosphere models. III. The relation to mixing length convection theory. *A&A*, 573:A89.

Maldonado, J., L. Affer, G. Micela, G. Scandariato, M. Damasso, B. Stelzer, M. Barbieri, L. R. Bedin, K. Biazzo, A. Bignamini, F. Borsa, R. U. Claudi, E. Covino, S. Desidera, M. Esposito, R. Gratton, J. I. González Hernández, A. F. Lanza, A. Maggio, E. Molinari, I. Pagano, M. Perger, I. Pillitteri, G. Piotto, E. Poretti, L. Prisinzano, R. Rebolo, I. Ribas, E. Shkolnik, J. Southworth, A. Sozzetti, and A. Suárez Mascareño

2015. Stellar parameters of early-M dwarfs from ratios of spectral features at optical wavelengths. *A&A*, 577:A132.

Matsumoto, T.

2021. Full compressible 3D MHD simulation of solar wind. *MNRAS*, 500(4):4779–4787.

Matsumoto, T. and K. Shibata

2010. Nonlinear Propagation of Alfvén Waves Driven by Observed Photospheric Motions: Application to the Coronal Heating and Spicule Formation. *ApJ*, 710(2):1857–1867.

Matsumoto, T. and T. K. Suzuki

2012. Connecting the Sun and the Solar Wind: The First 2.5-dimensional Self-consistent MHD Simulation under the Alfvén Wave Scenario. *ApJ*, 749(1):8.

Matsumoto, T. and T. K. Suzuki

2014. Connecting the Sun and the solar wind: the self-consistent transition of heating mechanisms. *MNRAS*, 440(2):971–986.

Mesquita, A. L. and A. A. Vidotto

2020. Global trends in winds of M dwarf stars. *MNRAS*, 494(1):1297–1307.

Meyer, C. D., D. S. Balsara, and T. D. Aslam

2012. A second-order accurate Super TimeStepping formulation for anisotropic thermal conduction. *MNRAS*, 422(3):2102–2115.

Miyoshi, T. and K. Kusano

2005. A multi-state HLL approximate Riemann solver for ideal magnetohydrodynamics. *Journal of Computational Physics*, 208(1):315–344.

Rosner, R., W. H. Tucker, and G. S. Vaiana

1978. Dynamics of the quiescent solar corona. *ApJ*, 220:643–645.

Sakaue, T. and K. Shibata

2020. Energy Transfer by Nonlinear Alfvén Waves in the Solar Chromosphere and Its Effect on Spicule Dynamics, Coronal Heating, and Solar Wind Acceleration. *ApJ*, 900(2):120.

- Scalo, J., L. Kaltenegger, A. G. Segura, M. Fridlund, I. Ribas, Y. N. Kulikov, J. L. Grenfell, H. Rauer, P. Odert, M. Leitzinger, F. Selsis, M. L. Khodachenko, C. Eiroa, J. Kasting, and H. Lammer  
2007. M Stars as Targets for Terrestrial Exoplanet Searches And Biosignature Detection. *Astrobiology*, 7(1):85–166.
- Seager, S.  
2013. Exoplanet Habitability. *Science*, 340(6132):577–581.
- Shoda, M., T. K. Suzuki, M. Asgari-Targhi, and T. Yokoyama  
2019. Three-dimensional Simulation of the Fast Solar Wind Driven by Compressible Magnetohydrodynamic Turbulence. *ApJL*, 880(1):L2.
- Shoda, M., T. K. Suzuki, S. P. Matt, S. R. Cranmer, A. A. Vidotto, A. Strugarek, V. See, V. Réville, A. J. Finley, and A. S. Brun  
2020. Alfvén-wave-driven Magnetic Rotator Winds from Low-mass Stars. I. Rotation Dependences of Magnetic Braking and Mass-loss Rate. *ApJ*, 896(2):123.
- Shoda, M., T. Yokoyama, and T. K. Suzuki  
2018. A Self-consistent Model of the Coronal Heating and Solar Wind Acceleration Including Compressible and Incompressible Heating Processes. *ApJ*, 853(2):190.
- Shu, C.-W. and S. Osher  
1988. Efficient Implementation of Essentially Non-oscillatory Shock-Capturing Schemes. *Journal of Computational Physics*, 77(2):439–471.
- Sokolov, I. V., B. van der Holst, R. Oran, C. Downs, I. I. Roussev, M. Jin, I. Manchester, Ward B., R. M. Evans, and T. I. Gombosi  
2013. Magnetohydrodynamic Waves and Coronal Heating: Unifying Empirical and MHD Turbulence Models. *ApJ*, 764(1):23.
- Suzuki, T. K.  
2018. Stellar winds and coronae of low-mass Population II/III stars. *PASJ*, 70(3):34.
- Suzuki, T. K., S. Imada, R. Kataoka, Y. Kato, T. Matsumoto, H. Miyahara, and S. Tsuneta  
2013. Saturation of Stellar Winds from Young Suns. *PASJ*, 65:98.
- Suzuki, T. K. and S.-i. Inutsuka  
2005. Making the Corona and the Fast Solar Wind: A Self-consistent Simulation for the Low-Frequency Alfvén Waves from the Photosphere to 0.3 AU. *ApJL*, 632(1):L49–L52.
- Suzuki, T. K. and S.-I. Inutsuka  
2006. Solar winds driven by nonlinear low-frequency Alfvén waves from the photosphere: Parametric study for fast/slow winds and disappearance of solar winds. *Journal of Geophysical Research (Space Physics)*, 111(A6):A06101.
- Tarter, J. C., P. R. Backus, R. L. Mancinelli, J. M. Aurnou, D. E. Backman, G. S. Basri, A. P. Boss, A. Clarke, D. Deming, L. R. Doyle, E. D. Feigelson, F. Freund, D. H. Grinspoon, R. M. Haberle, I. Hauck, Steven A., M. J. Heath, T. J. Henry, J. L. Hollingsworth, M. M. Joshi, S. Kilston, M. C. Liu, E. Meikle, I. N. Reid, L. J. Rothschild, J. Scalo, A. Segura, C. M. Tang, J. M. Tiedje, M. C. Turnbull, L. M. Walkowicz, A. L. Weber, and R. E. Young  
2007. A Reappraisal of The Habitability of Planets around M Dwarf Stars. *Astrobiology*, 7(1):30–65.

- van der Holst, B., I. V. Sokolov, X. Meng, M. Jin, I. Manchester, W. B., G. Tóth, and T. I. Gombosi  
2014. Alfvén Wave Solar Model (AWSoM): Coronal Heating. *ApJ*, 782(2):81.
- Velli, M.  
1993. On the propagation of ideal, linear Alfvén waves in radially stratified stellar atmospheres and winds. *A&A*, 270(1-2):304–314.
- Vidotto, A. A. and V. Bourrier  
2017. Exoplanets as probes of the winds of host stars: the case of the M dwarf GJ 436. *MNRAS*, 470(4):4026–4033.
- Vidotto, A. A., M. Jardine, J. Morin, J. F. Donati, M. Opher, and T. I. Gombosi  
2014. M-dwarf stellar winds: the effects of realistic magnetic geometry on rotational evolution and planets. *MNRAS*, 438(2):1162–1175.
- Wood, B. E., H. R. Müller, G. P. Zank, J. L. Linsky, and S. Redfield  
2005. New Mass-Loss Measurements from Astrospheric Ly $\alpha$  Absorption. *ApJL*, 628(2):L143–L146.
- Yokoyama, T. and K. Shibata  
1998. A Two-dimensional Magnetohydrodynamic Simulation of Chromospheric Evaporation in a Solar Flare Based on a Magnetic Reconnection Model. *ApJL*, 494(1):L113–L116.

## Chapter 4

# Concluding Remarks

As noted in Section 1.1.2, the study on M-dwarf's magnetic activities is motivated by the following scientific interests. The first interest is in whether physical mechanisms for the M-dwarf's and solar magnetic activities can be understood in a unified way. The second interest is in the influence of M-dwarf's magnetic activities on the interplanetary space and exoplanets.

Through the study described in Chapter 2, we found a possibility that the stellar magnetic flux tube cannot guide the Poynting flux from the surface convection layer to the stellar corona, when the Alfvén wave is too highly nonlinear in the stellar chromosphere. This is caused because the twisting magnetic flux tube with large inertia cannot be restored by the Lorentz force of propagating Alfvén wave. The strong shear flow driven by the competing of inertia force with Lorentz force results in the chromospheric intermediate shock. The importance of our finding is that, first, this phenomenon is expected to be ubiquitous around the stellar chromospheres. We derived the following scaling law as the requirement for inducing the chromospheric intermediate shock.

$$v_{\text{conv}}/c_{\text{sph}} \gtrsim 4.2\sqrt{\bar{B}/B_{\text{ph}}}, \quad (4.1)$$

where  $v_{\text{conv}}$ ,  $c_{\text{sph}}$ ,  $\bar{B}$ , and  $B_{\text{ph}}$  are the convective velocity, sound speed on the photosphere, chromospheric magnetic field strength, and the photospheric magnetic field strength, respectively. That means the limitation of the transmission of Poynting flux into the corona is expected to be ubiquitously observed in the weak chromospheric magnetic field environment. Another important feature of our finding is that the dynamics and emission of the upper chromosphere to the corona is not necessarily correlated with those of the lower to middle chromospheres. In fact, as a result of the formation of chromospheric intermediate shock, the dynamics of spicule becomes independent of the energy input from the photosphere (Figure 2.5). This result highlights the importance of considering the energy transfer and dissipation of Alfvén wave in the lower atmosphere where the wave nonlinearity rapidly grows with height, for the discussion about the dynamics of upper chromosphere, coronal heating, and stellar wind acceleration.

Through the study described in Chapter 3, we could directly address the second scientific interest. Because our estimates of mass-loss rate of M-dwarf's wind is much smaller than those previously reported by three-dimensional (3D) magnetohydrodynamics (MHD) global modelings, it would be necessary to reassess the interplanetary environment around the M-dwarf's planets. In addition, it is remarkable that, for the first time, we identified the definitive role of slow shock which is excited by nonlinear Alfvén wave in the stellar wind acceleration. Because the contribution of such compressible waves to the stellar wind acceleration has been totally neglected in the 3D MHD global modeling, our finding again highlights the importance of resolving the nonlinear propagation of Alfvén wave in the non-steady stellar wind. Finally, we summarize

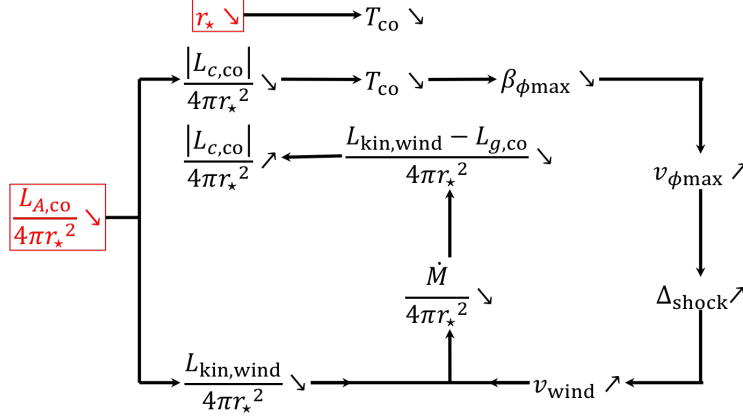


Figure 4.1: Schematic chart to explain the physical mechanisms for differences in the coronal temperature ( $T_{\text{co}}$ ), wind velocity ( $v_{\text{wind}}$ ), and mass-loss rate ( $\dot{M}$ ) between the Sun and M dwarfs.

the physical mechanisms for differences in the coronal temperature ( $T_{\text{co}}$ ), wind velocity ( $v_{\text{wind}}$ ), and mass-loss rate ( $\dot{M}$ ) between the Sun and M dwarfs. From the Sun to M dwarfs, the stellar radius ( $r_*$ ) decreases and the transmitted Alfvén wave energy into the corona ( $L_{A,\text{co}}/(4\pi r_*^2)$ ) decreases slightly. The smaller  $L_{A,\text{co}}/(4\pi r_*^2)$  is, the smaller  $|L_{c,\text{co}}|/(4\pi r_*^2)$ , which represents the conduction flux, is. Combining the smaller  $r_*$  and  $|L_{c,\text{co}}|/(4\pi r_*^2)$ ,  $T_{\text{co}}$  tends to be cooler in M dwarfs. The cooler coronal temperature is associated with lower plasma  $\beta$  of stellar wind, in which the amplification of Alfvén wave ( $v_{\phi \text{max}}$ ) is promoted. The larger  $v_{\phi \text{max}}$  could excite the stronger slow shock, leading to the significant contribution to the stellar wind acceleration ( $\Delta_{\text{shock}}$ ). On the other hand, because of smaller  $L_{A,\text{co}}/(4\pi r_*^2)$ , the kinetic energy flux of M dwarf’s stellar wind ( $L_{\text{kin,wind}}/(4\pi r_*^2)$ ) tends to be smaller. The smaller  $L_{\text{kin,wind}}/(4\pi r_*^2)$  and faster  $v_{\text{wind}}$  lead to the smaller mass flux  $\dot{M}/(4\pi r_*^2)$ , which prevent  $|L_{c,\text{co}}|/(4\pi r_*^2)$  from continuously decreasing.